UNIVERSITÀ DEGLI STUDI DI CATANIA
CORSO DI DOTTORATO IN FISICA

DOMENICO TORRESI

EXCITATION OF UNBOUND STATES IN ^{12}B VIA THE ^{8}Li-α RESONANT ELASTIC SCATTERING

COORDINATORE DEL CORSO:
PROF. F. RIGGI

RELATORI:
PROF. M. LATTUADA
DOTT.SSA M.G. PELLEGRITI

TESI PER IL CONSEGUIMENTO DEL TITOLO

XXIII CICLO 2007-2010

πῆρά τοι μαθήσιος ἀρχά

Alcmane

Contents

Introduction

The cluster structure, especially involving α-particles, is one of the essential features the characterize the nuclear structure particularly for light nuclei. This fact is sustained by the presence of groups of levels that cannot be explained inside the shell model framework.
The clustering study on $N = Z$ nuclei has been directed on two branches [1]. The first is the search for di-nuclear structures and the second is the search for complex α particle systems. These studies suggest that two body cluster structures exist in a broad variety of systems extending up to ^{28}Si+^{28}Si. An example is the di-nuclear cluster configuration ^{12}C+^{12}C of ^{24}Mg at energies close to the Coulomb barrier.

In the last decade, the study of cluster states has been directed towards the so called *exotic clustering*. Exotic cluster configurations are those configurations where at least one of the constituent clusters is unstable. In this context several theoretical studies were devoted to investigate the cluster structure of light neutron rich nuclei. In particular n-rich isotopes of Li, Be and B were studied by means of different models, for example, the Antysimmetrized Molecular Dynamics and Generator Coordinate Method. Calculations based on these methods indicate the existence of cluster structures involving very exotic configurations [2–10].

One way to study such resonant states, rather than populating them directly, is to use three-body reactions producing the nucleus under consideration in an intermediate step with a following decay into the relevant final state. One of the main advantages of this approach is that

the energy spectrum of the compound nucleus is sampled in a single experimental setting. Furthermore by measuring the angular distributions of the reaction products, a measurements of the spin and parity of the excited states is possible. For example ^{24}Mg states were investigated by using the reaction ^{12}C(^{16}O,^{24}Mg*)α. In this case the presence of a narrow resonance, a few hundred keV broad, with an high partial decay width, represents a strong indication of the cluster structure of the states [11].

It is possible to investigate the presence of such di-nuclear structure by studying the excitation function of nuclear processes where the two cluster are present in the exit channel and possibly also in entrance channel. In particular elastic and inelastic scattering have been widely used in these kind of studies. For example resonances in ^{24}Mg concerning ^{12}C+^{12}C cluster structure have been found by using ^{12}C on ^{12}C elastic scattering.

This thesis reports an experimental investigation of the cluster structure of ^{12}B excited states by using, for the first time, the ^{8}Li elastic scattering on ^{4}He. The ^{8}Li beam was provided by the LNS radioactive beam facility EXCYT at energy of 30 MeV. The method that has been used was the Thick Target Inverse Kinematics scattering method which is very suitable for low intensity beam. The main advantage of this method is the capability of measuring the elastic excitation function in a wide range of energy by using a single beam energy and a single experimental settings. Moreover the inverse kinematics represents an unique tool to measure the elastic scattering cross-section also at 180° degree in the CM system where it is mostly sensitive to the nuclear part of the interaction. This work adds information on the energy spectrum of ^{12}B for energy above the α-emission threshold reporting for the first time data on ^{8}Li elastic scattering on ^{4}He cross section. The absolute elastic cross-section was measured in the CM energy range between 3 MeV and 9.5 MeV.

This thesis is organized as follow:

- Chapter 1 gives an overview on the cluster model and shortly describes microscopic cluster models used for theoretical investigations on the cluster structure of light nuclei.

- Chapter 2 describes several experimental techniques used for the investigation of elastic and inelastic excitation function which are suitable for low intensity beams. Particular emphasis is given to the Thick Target Inverse Kinematics scattering method on which is based the experiment presented in this thesis.

- Chapter 3 discusses the production of radioactive ion beams by using the Isotope Separator On Line technique. The EXCYT facility of LNS is described highlighting the specific characteristic of the ^{8}Li beam production.

- Chapter 4 contains a description of the experimental set-up including the detectors and the used electronics. The detectors energy calibration procedure is discussed in details.

- Chapter 5 reports on the importance of accurate measurements of the target stopping power for beam and recoil particles in order to extract the excitation function by using the TTIK method. In particular the description of the experiment performed in the framework of this thesis in order to measure the ^{4}He stopping power for the ^{7}Li ions is given.

- Chapter 6 reports the analysis procedure in details. In particular the method that has been followed to extract the excitation function for ^{8}Li on ^{4}He from experimental data is described. The obtained elastic excitation function for ^{8}Li on ^{4}He is shown and the results are compared with those present in literature.

Chapter 1

Theoretical Concepts on Nuclear Clustering

In this chapter the Nuclear Cluster Model is introduced. Two microscopic cluster models are described in their main aspects: the Generator Coordinate Method (GCM) and the Antisymmetrized Molecular Dynamics (AMD). Then, specific calculations of Kanada-En'yo and Horiuchi on neutron-rich Boron isotopes by means of AMD and calculation [4] and theoretical studies of Descouvemont on ^{12}B by means of GCM [10] will be discussed.

1.1 The Nuclear Cluster Model.

Many nuclear properties, especially for the ground state, can be described by an independent particle approach, where the assumption is that the average effects of nuclear forces can be described by a single particle field and the effects not included in this single particle field are described by an effective two body correlation. This assumption is the basis of the nuclear shell model and many developments on the nuclear description of the structure were made by using a single particle field plus an effective two body-correlation.

This framework of *single particle plus two-body correlation*, although represents a basis for an unified understanding of many nuclear phenomena, does not exhaust all the nuclear properties. In other words not all the properties of nuclei can be described in this scheme and the correlations among nuclei are not limited to two-body correlations. There exist groups of levels in light nuclei that present properties that cannot be understood inside the shell model interpretations, which has its own basis on the independent particles picture.

For example in the α-nuclei [1] ^{12}C, ^{16}O, ^{20}Ne the molecule-like structures are clearly observed in excited states. Also in non-α-nuclei [2] cluster structure can be seen, for example in ^{9}Be, which is the prototype of the molecule-like structure in a non-α-nuclei, and in ^{10}B which shows a three -cluster structure. In light nuclei, structures which cannot be included in shell model appear in low-lying states close to the threshold for particle emission (in general in α-nuclei these levels are close to the α-decay threshold).

The presence of these kind of structures, especially involving α-cluster, indicates that "The molecular aspects, including the aspects dominated

[1] nuclei that can b decomposed into an α particles sub-units.

[2] non-α-nuclei are defined as nuclei composed of an α-nucleus core and one or more valence nucleons; ^{9}Be is the prototype of this kind of nuclei.

by alpha-like four-body correlations as a typical case, constitute one of the essential facetes of nuclear structure"[12].

The cluster model describes nuclei as to be composed of clusters, where cluster means a spatially localized subsystem composed of strongly correlated nucleons. When the clustering correlation becomes so strong that the relative motion between clusters becomes the fundamental mode of motion of the nucleus, different degrees of freedom appear that are not treated by other models, typically shell model, based on single particle approach.

There are three fundamental characteristics common to the cluster nuclei:

- "strong internal cluster correlations and weak inter-cluster correlation".
- The twofold role of the Pauli principle.
- The threshold rule.

The first characteristic described as: *"strong internal cluster correlations and weak inter-cluster correlation"* [13] means that the binding energy of the constituent clusters is similar to the free case (the binding energy of the free clusters) while the inter cluster interaction is weak enough to preserve the identity of the clusters. In other words: the tight binding of the constituent clusters assures the maintenance of the identity of the clusters while the weak interaction between clusters does not destroy the stability of these clusters.

This is intimately connected to the action of the Pauli principle which strongly affects the internal structure of the nucleus. In fact the Pauli principle, in the case of usual nuclei in their ground state, allows that the nucleons arrange in shell model orbits *promoting* the single particle *feature*. On the other hand when a molecular structure is considered the

Pauli principle acts as an effective repulsive core force when, for example, two α particles overlap generating the molecular structure. Ikeda called this twofold behavior of the Pauli principle as the *"dual role of the Pauli principle"* [12]. From one hand the Pauli principle permits nucleons to arrange in α particles; on the other hands, acting as an effective repulsive core force, it prevents that two α particles overlap upholding the cluster structure.

An other common characteristic of nuclei that show cluster structures is that these structures appear close or above the cluster emission threshold, the so called *"threshold rule"* [12, 13]. The threshold rule was firstly observed as an empirical rule, and then it was recognized as a necessary condition in order to disclose the cluster structure.

The break-up energy of a saturated nucleus into saturated fragments nuclei is small due to the well-known properties of the nuclear interaction. In other words, the main part of the binding energy of the ground state of light nuclei comes from the α-cluster internal energy while the small, but significant, surplus comes from the dissolution of α-cluster in shell-model structure. This means firstly that the amount of energy needed for the appearing of the cluster structure is small, secondly that the binding energy of the inter-cluster relative motion is also very small. The threshold rule is an outcome of the following rule: *"strong internal cluster correlations and weak inter-cluster correlations"*[13].

The threshold rule tells us that when the excitation energy of a nucleus increases more break-up channels are opened and more cluster configurations appear in nuclei. This is pictorially shown in the so called "Ikeda diagram" [12, 13] fig.(1.1).

In the Ikeda diagram the α particle plays the main role of cluster unit, because it is the lightest saturated nucleus with high binding energy and very high-lying first excited state. In the diagram the lowest excitation energies correspond to shell-model like structures while the n-α structure

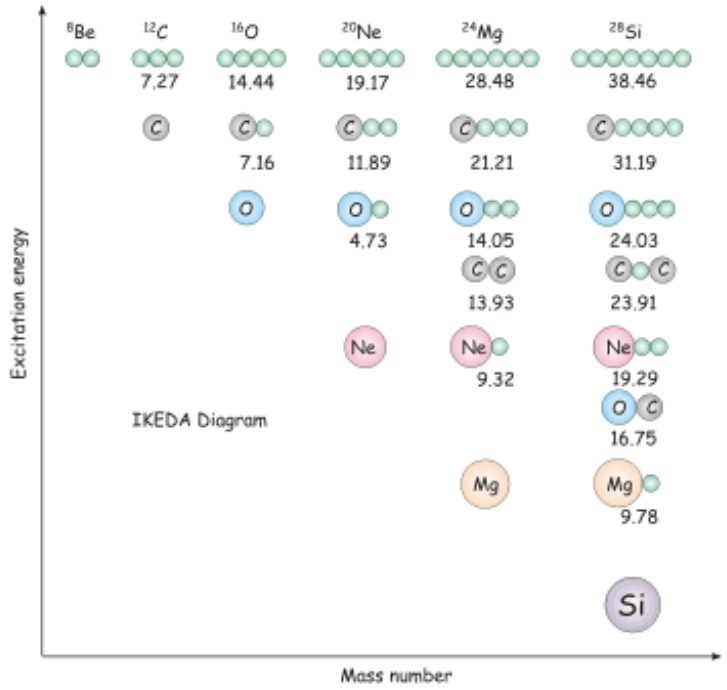

Figure 1.1: *The Ikeda diagram from [14]. The picture shows how cluster structure evolves as the excitation energy of the system increases. The cluster configurations appear when the excitation energy of the nucleus is close to the cluster decay threshold. For example, the configuration with the highest number of cluster (n-α) appears only at the highest energy.*

appears at higher excitation energies. In between these two extremes different kinds of cluster structures appear when excitation energy is close to the threshold of break-up into the constituent clusters.

Among the cluster correlation the α cluster one is the most prominent. In fact, in light nuclei there have been found many cluster states involving α cluster correlations, see [14]. ^{4}He nucleus has a closed shell and the first excited state lays very high close to 20 MeV whereas the average binding energy is less than 8 MeV per nucleon. This makes the α-particle a perfect candidate to be a cluster. This means that the α-particle can keep its own identity for a relatively long time in its motion inside the nucleus. A good cluster candidate should have high binding energy and high lying

first excited state. This ensure that the cluster keeps its individuality inside the nucleus and that the rule: "*internally strong-externally weak*" will be satisfied. As it is shown in Fig. (1.2) the α particle is the best cluster candidate. Anyway also ^{12}C, ^{14}C, ^{15}N, ^{14}O, ^{16}O (inside the box in the figure) may be good cluster.

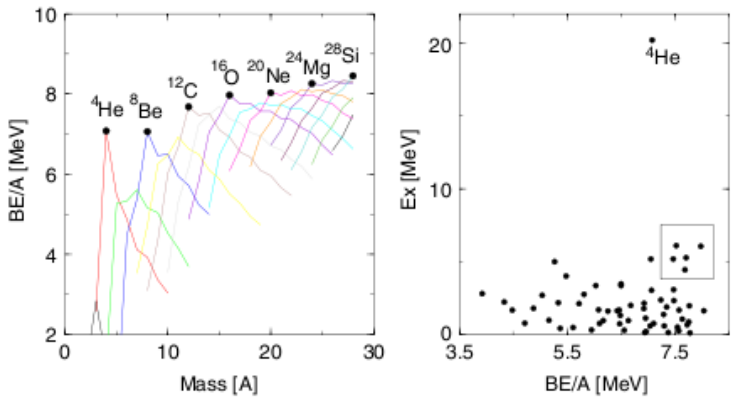

Figure 1.2: *On the left the binding energy per nucleon of light nuclei, the lines connect different isotopes of each element. On the right excitation energy of the first excited state plotted versus the binding energy per nucleon for nuclei up to A=20. the box includes nuclei which can form clusters :* ^{12}C ^{14}C ^{14}O ^{15}N ^{16}O *[14].*

In fact, as mentioned before, although the α particle is the dominant cluster there is evidence of cluster structure also for non-α-nuclei. For example ^{6,7}Li show α+d and α+t structures respectively.

The sequence of 4n+1 nuclei: ^{5}He, ^{9}Be, ^{13}C and ^{17}O show a very peculiar feature. Their structure and binding energy are deeply affected by the valence neutron. The ^{9}Be nucleus can be described by means of a α - n - α structure where the covalent exchange of a neutron between the α-cores appears [15].

The α-conjugate nucleus ^{8}Be is unstable and decays α. The only stable Be isotope is ^{9}Be. The additional neutron is exchanged between the two α cores as an electron is exchanged between atoms in a covalent atomic molecule. For this kind of states the expression "nuclear

molecules" is used. Just as in H_2 molecule the high delocalized spatial extension of the wave function (Heisenberg principle) lowers the kinetic energy increasing the binding energy with respect to the ^{8}Be case. Detailed studies on the structure of beryllium isotopes can be found in references [16–18];

The phenomenological $\alpha-\alpha$ interaction which gives rise to the cluster structure has a shape similar to the molecular one. It shows the following features.

- it is strongly repulsive for very low distance ($\sim$1.8 fm).
- in the outer region, up to the *contact* region ($\sim$3.5 fm), the interaction is attractive.

Anyway the real $\alpha - \alpha$ interaction does not have bound states but a fictitious interaction, where the Coulomb force is switched off, is slightly bounding [12, 19]. The $\alpha-\alpha$ interaction, compared with the binding force of a diatomic molecule H_2 and with the binding force of a deuteron, shows an intermediate behavior see fig.(1.3). It manifests a binding ability that is intermediate between the H_2 and the deuteron cases. Anyway it should be noted that a simple analogy with molecules does not hold for nuclei.

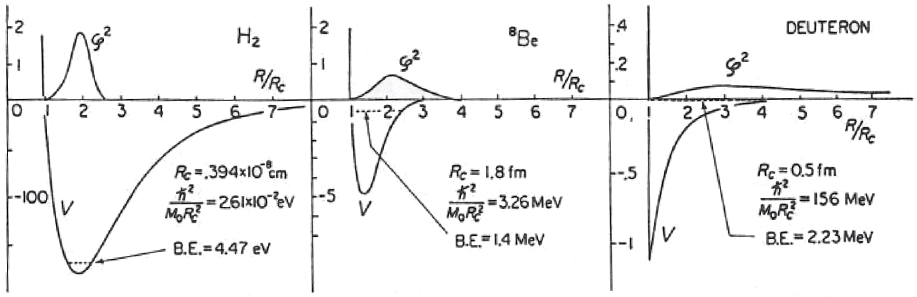

Figure 1.3: *Comparison of three binding forces: binding potencial for the ground state of the He_2 molecule; the α-α potencial (nuclear only) for the ground state of the ^{8}Be and the two nucleon potential for the deuteron from [12].*

1.2 Microscopic Cluster Models.

Microscopic cluster models are based on a description of the nucleus which takes into account the individual constituents of the nucleus with an effective nuclear interaction. There are many different microscopic models. The first proposal of a microscopic cluster model was done by Wheeler in 1937 with the Resonating Group Model (RGM) [20, 21]. Subsequently more sophisticated models were developed like AMD. In the following a basic description of some microscopic models will be shown.

1.2.1 Resonating Group Model and Generator Coordinate method

The Resonating Group Model (RGM) wave function Ψ is given by a linear superposition of the basis wave functions Ψ_{nk}

$$\Psi = \sum_{n,k} \Psi_{nk} \tag{1.1}$$

where Ψ_{nk} is expressed as

$$\Psi_{nk} = \mathscr{A}\{\chi(\vec{\xi}_1, \ldots, \vec{\xi}_{n-1})\phi(C_{k1}) \ldots \phi(C_{kn})\} \tag{1.2}$$

Here n denotes the number of cluster and k is the label that contains all the other quantum numbers that determine the quantum state of the system: angular momentum, spin, parity and so on [14, 19, 20]. $\phi(C_i)$ is the intrinsic wave function of the Cluster C_i and $\chi_k(\vec{\xi}_1, \ldots, \vec{\xi}_{n-1})$ is the wavefunction of the relative motion coordinates $\vec{\xi}_i, \qquad i = 1, 2, \ldots, n-1$ among clusters. The $\chi_k(\vec{\xi}_1, \ldots, \vec{\xi}_{n-1})$ are obtained by variational or projection method for the given microscopic hamiltonian and for the given bound or scattering boundary conditions. The RGM is very suitable to describe the dynamical properties of light nuclei.

In order to avoid difficulties in actual calculations of RGM, Brink introduced the Generator Coordinate Method (GCM) into the cluster

model. The GCM is a powerful general microscopic method which is used to describe many kinds of collective motion in nuclei and includes antisymmetrization [14]. This model permits reactions between the asymptotic clusters to be studied. In fact, within the Resonating Group Model (RGM) formalism the wave function describing A nucleons, aggregated for example into two clusters A_1 and A_2, is written as:

$$\Phi(\mathbf{r}_1, \mathbf{r}_2, \ldots, \mathbf{r}_A) = F(\mathbf{R}_{c.m.})\hat{A}\phi_1(\xi_1)\phi_2(\xi_2)g(\mathbf{R}) \tag{1.3}$$

where $F(\mathbf{R}_{c.m.})$ describes the motion of the centre of mass of the nucleus, ϕ_i is the antisymmetrized wavefunction describing the internal state of the cluster i, ξ_i are the internal coordinates, $g(\mathbf{R})$ is the function of the relative motion of the two clusters, $\hat{A}$ is the antisymmetrization operator that exchanges nucleons between the two clusters. The advantages of using this method are, firstly, that the cluster are fully antisymmetrized, secondly, that the centre of mass of the system is correctly treated so that the quantum numbers produced have a realistic meaning in term of asymptotic fragments. One of the drawback of the method is that an *a priori* assumption of the cluster structure is mandatory. The method was extensively applied by Baye and Descouvemont to various unstable nuclei, and can reproduce the characteristic of the molecular state in ^{9,10,11}Be [22].

1.2.2 Antisymmetrized Molecular Dynamics

The Antisymmetryzed Molecular Dynamics (AMD), reviewed in [5], was originally developed by Ono et collaborators for the study of nuclear reactions [23, 24]. Later on, it was extended by Horiuchi, Kanada En'yo and collaborators to nuclear structure studies [4, 6].

With respect to other microscopic cluster models, it has the main advantage that there are no assumptions about the constituent clusters, no preformed clusters are imposed, but they emerge naturally. Another

important characteristic is the flexibility of the wave functions that can represent at the same time cluster structures and shell-model like structures.

In the AMD approach the A nucleon wave-function is fully antisymmetrized by mean of a Slater determinant

$$\Phi_{AMD}((Z) = \frac{1}{\sqrt{(A!)}}\mathscr{A}(\phi_1, \phi_2, \ldots, \phi_A) \tag{1.4}$$

The individual single-particle wave-functions ϕ_i can be written as

$$\phi = \psi_{X_i}\chi_i\tau_i \tag{1.5}$$

where ψ is the spatial part of the wave function and it is described by mean of a Gaussian wave-packet

$$\psi_{X_i}((r)_j) = exp\left\{-\nu\left((r)_j - \frac{X_i}{\sqrt{(\nu)}}\right)^2\right\} \tag{1.6}$$

χ_i are the intrinsic spin function s

$$\chi_i = \left(\frac{1}{2} + \xi_i\right)\chi_\uparrow + (\frac{1}{2} - \xi_i)\chi_\downarrow \tag{1.7}$$

and τ_i are the intrinsic isospin functions. $\mathbf{Z}$ is a set of variables describing the geometry and spin of the wave-function with which the AMD function is parametrized. The energy is computed variationally by using an effective nucleon-nucleon interaction [25]

In fig. (1.4) an example of AMD calculation is shown. Density distribution for different berillium isotopes (^{6-14}Be) are plotted. All isotopes possess a clustered proton distribution. For ^8Be, in which the number of neutrons is equal to the number of protons, the distance between the cluster cores has a maximum, while for the other isotopes the neutrons reduce the core distance generating more spherical distributions [26].

This method has been widely used to describe light $N = Z$ nuclei as well as nuclei far from the $N = Z$ line, in particular for Li, Be, B [4]

and C isotopes [25] and reference therein. It permits to describe ground and excited states of stable and unstable nuclei. In general experimental binding energies, transition rates, radii and momenta, for normal nuclei are well reproduced.

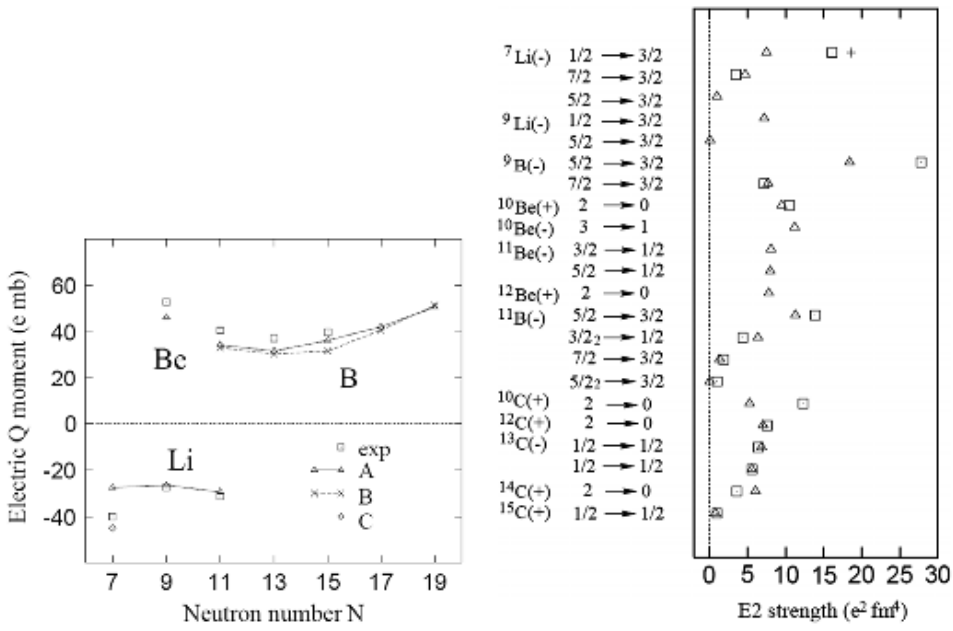

Figure 1.4: *On the left electric quadrupole momenta for Li, Be and B isotopes. The experimental data (square) are compared with AMD calculations (others symbols) with slightly different interactions and constructions. On the right experimental E2 transitions (square) for Li, Be, B and C isotopes compared with AMD calculations (other symbols); for more details see [5].*

In fig. (1.4) some examples of comparison between AMD calculations and experimental electric quadrupole momenta and electromagnetic transition rates from [5, 25] are shown.

1.3 Boron Isotopes AMD Calculations

Kanada-En'yo and Horiuchi performed systematic studies with the AMD on B isotopes up to the neutron drip-line [2, 4]. It is important to stress again that one of the main advantage of the AMD model is that

no *a priori* assumptions on existence of any cluster is required. It is well known that close to the $N = Z$ region, cluster structures appear like the $\alpha + t$ structure in ^{7}Li or $\alpha + \alpha$ in ^{8}Be. For n-rich nuclei close to the drip line there are poor informations on the cluster structure than it is difficult to assume an a priori configuration.

In their work Kanada-En'yo and Horiuchi show a drastic structure change for increasing neutron number for odd-even B isotopes with a behavior similar to Li and Be isotopes where shell-model-like structures appear for N=8 isotopes and develop toward cluster structures for higher N.

The AMD calculation reproduces well the experimental values of several quantities especially electromagnetic properties. Anyway we are more interested on discussing the intrinsic structure of the state obtained with AMD. The density distribution is one of the quantities that can strongly suggest structural change in nuclei. Fig. (1.5) shows the density distribution for the ground states of the even n-rich isotopes of B. The total density distribution ρ is shown as well the proton and neutron density distributions ρ_p and ρ_n.

^{13}B has the most spherical structure among the B isotopes under investigation. This is linked with the neutron shell closure at N=8. Indeed looking at the density distribution for neutron and proton separately, the change in the structure toward a shell configuration for ^{13}B is more evident in ρ_n with respect to ρ_p. The eight neutrons in ^{13}B constitute a closed shell that generates a spherical structure, while ^{11}B with its six neutrons, shows an oblate shape. Increasing the neutron number, deformed structures appear again with a prolate shape: ^{15}B that has 10 neutrons shows a prolate shape, supporting that the deformation increases with neutron number. For protons we observe a cluster structure in ^{11}B that becomes weaker for ^{13}B and stronger for ^{15,17,19}B

For what concerns properly cluster structures, ^{11}B exhibit a deformed

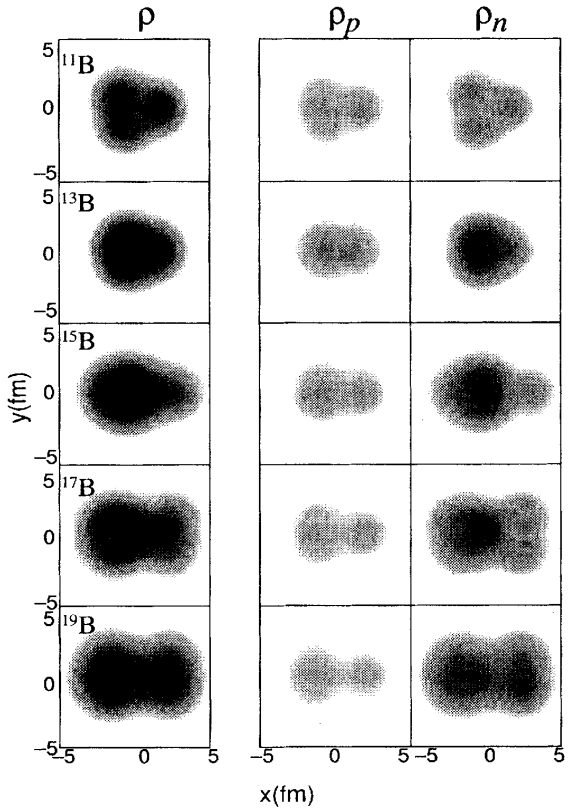

Figure 1.5: *Density distribution of AMD states of B isotopes. The density of proton ρ_p and neutrons ρ_n are shown separately. $\rho = \rho_n + \rho_p$ [4].*

state indicating a structure ^{7}Li(t+α)+α although not so well developed. The AMD calculations show also that cluster structure is prominent in B isotopes near the drip line. Fig. (1.6) shows the spatial configurations of the centre of single particle gaussian wave-packets, the square and the circles correspond to protons and neutrons respectively. Neutrons with opposite spin but with the same quantum number occupy the same position. In ^{11}B the three pairs of neutrons give place to a triangle configuration, four protons follow the neutrons configurations but the fifth is between two pairs of neutrons. The resulting structure is similar to the ^{7}Li(t+α)+α structure. In the oder B isotopes the protons are grouped in two bunches surrounded by neutrons: one with three protons

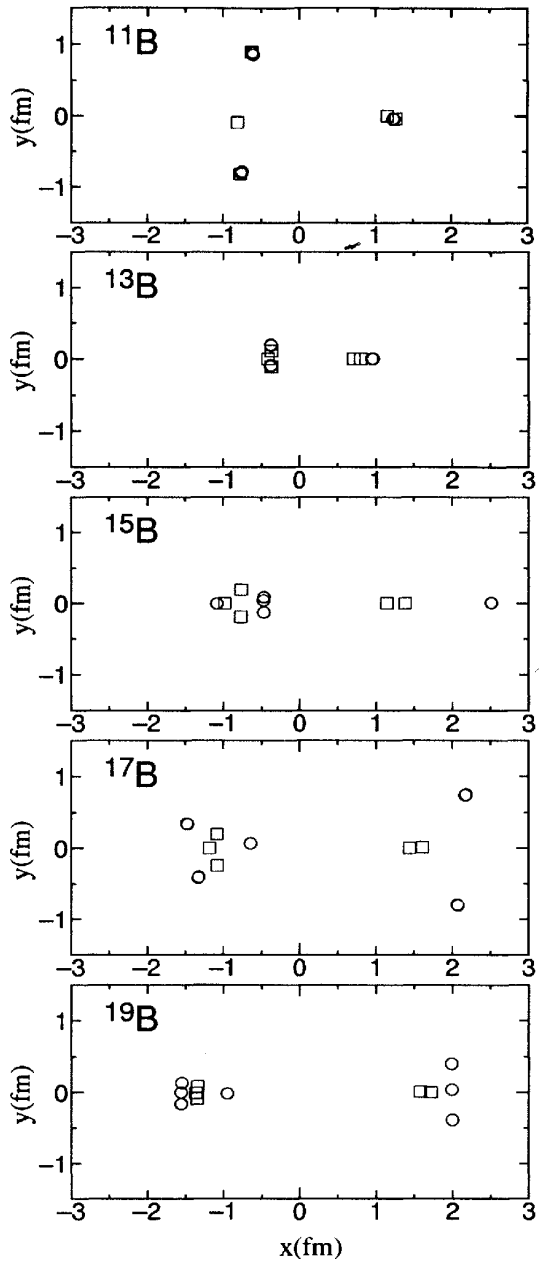

Figure 1.6: *Spatial configurations of centers of nucleon wave packets. circles and squares represent the centres of neutrons and protons [4].*

and the other one with two protons. It give rise to cluster configurations ^{9}Li+^{4}He, ^{11}Li+^{4}He, ^{11}Li+^{6}He, ^{11}Li+^{8}He for ^{13}B, ^{15}B, ^{17}B, ^{19}B respec-

J^π	$E_{c.m.}$	E_x	$\theta^2_{\alpha_0}$	$\theta^2_{n_0}$	Γ_{α_0}	Γ_{n_0}	Γ_{tot}
0^+	0.77	10.77	9.9	0.7	10	62	134
1^+	0.80	10.80	7.3	0.5	9	44	92
2^+	0.59	10.59	19.2	0.3	34	43	403
3^+	2.04	12.04	13.5	0.1	203	7	327
4^+	0.11	10.11	1.6	0.04	4.5×10^{-8}	2.8	144
2^-	-0.55	9.95	2.1	2.9	0	1400	2300
3^-	1.13	11.13	23.6	1.3	190	120	1000

Table 1.1: *Parameters for ^{12} excited statesas calculated in [10]. Energy are expressed in MeV, reduced widths (at 8.1 fm) θ^2 in %, widths in keV. E_x=$E_{c.m.}$+10.001.*

tively . The relative distance between clusters increases from ^{13}B to ^{19}B, a behavior that suggests a transition between a shell-like structure to a better developed cluster structure. A peculiar point for clustering structure in neutron-rich nuclei close to the drip-line is that the constituent clusters are not ordinary stable cluster (like ^{4}He) but unstable clusters that experience a kind of distortion and polarization where the neutrons are distributed in the outer region. Ordinary cluster are stable and difficult to be excited (like ^{4}He) while the cluster found in B n-rich isotopes are not stable and very easy to be broken.

1.4 GCM Calculations ^{12}B

A GCM study on ^{12}B was performed by Descouvemont and Baraffe [7] and Descouvemont [10]. In the following we will refer mainly to the second article that is the most recent. The spectroscopy of ^{12}B was investigated for two cluster functions involving ^{11}B-n and ^{8}Li-α structure. Excited state of ^8Li and ^{11}B were considered inside calculations. We remember that in GCM model an *a priori* choice on the cluster structure must be done.

The energy spectrum of ^{12}B is shown in fig.(1.7). The positive parity states are shown on the left side while negative parity states are shown

on the right side. Experimental energies of the states are taken from ref. [27]. The GCM calculations overestimate the binding energy of the positive parity states by few MeV, and the lower state is a 2^+ instead of the experimental 1^+ state. In the negative parity band there is a good energies agreement and also the sequence of the first three states is well reproduced. Some properties of the positive band are shown in tab. (1.1).

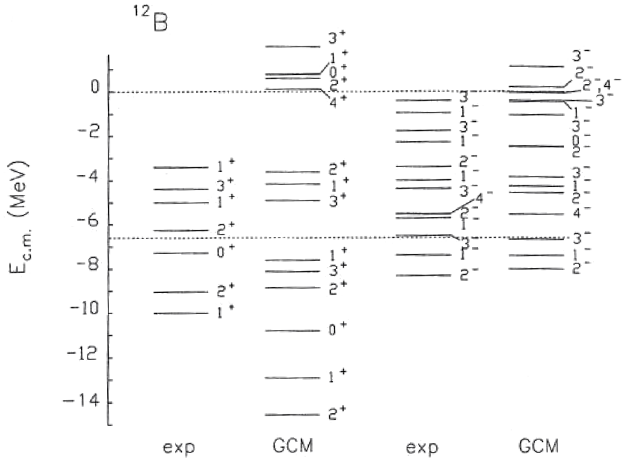

Figure 1.7: *Experimental Energy spectra respect to the α-^8Li threshold of ^{12}B form [27] and calculated spectra of ^{12}B for positive parity (left side) and negative parity (right side) from[10]. Dotted line are threshold for n-^8Li (lower line) and α-^8Li (upper line) of ^{12}B.*

The reduced widths θ^2 are calculated for a radius of 8.1 fm. In the case of the positive parity band, although the ratio $\Gamma_{\alpha_0}/\Gamma_{tot}$ is smaller than 0.1 except for the 3^+ state, the large reduced width θ_{α_0} support the $\alpha - ^8 Li$ cluster picture. On the opposite, for the negative parity band there is no indication for an $\alpha - ^8 Li$ cluster picture.

Chapter 2

The Experimental Method

In this chapter the elastic resonant scattering is introduced. A brief review of some method used to extract the excitation function for elastic scattering in inverse kinematics suitable for low intensity beam. Particular care is dedicated to the Inverse Kinematics Thick Target scattering method used for the study of the ^{4}He(^{8}Li,α)^{8}Li reaction presented in this thesis. An improvement of the method, consisting into the time of flight measurement, that allows the discrimination of elastic from inelastic scattering, is discussed. Also a short description of R-matrix formalism is given.

2.1 Resonant Elastic Scattering

In nuclear and atomic physics as well as in particle physics a **resonance** is defined as a circumstance where the scattering cross-section from a given potential shows a strong peak.
Let $V(r)$ be a potential with a finite range. The effective potential for the l^{th} wave is

$$V_{eff}(r) = V(r) + \frac{\hbar^2}{2m}\frac{l(l+1)}{r^2} \tag{2.1}$$

where the last term is the centrifugal barrier term. Since this last is repulsive the effective potential has an attractive well followed, at large distance, by a repulsive barrier as shown in fig. (2.1). It is possible that an incident particle lives inside the potential well. These states, anyway,

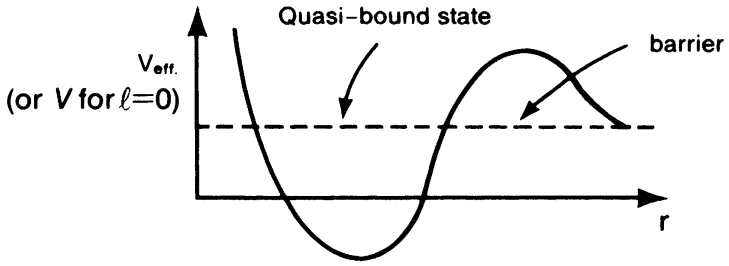

Figure 2.1: *A pictorial view of the effective potential V_{eff} the dashed line represents a quasi-bound state above the particle emission threshold [28].*

cannot be trapped forever because the trapped particle can escape for tunnel effect after a given time. These kinds of states that are not bound are called quasi-bound states (since they should be bound states when the repulsive barrier is infinitely high).

In order to find an expression for the cross-section in proximity of a resonance let us recall that the scattering amplitude can be expressed in expansion of partial-waves

$$f(k', k) = f(\theta) = \sum_{l=0}^{\infty}(2l+1)f_l(k)P_l(\cos\theta). \tag{2.2}$$

Where $P_l(cos(\theta)$ are the Legendre polynomial and $f_l(k)$ are the partial scattering amplitudes. The cross-section and the scattering amplitude are connected by the following equation:

$$\frac{d\sigma}{d\Omega} = |f(k', k)|^2. \tag{2.3}$$

Let introduce the scattering matrix:

$$S_l(k) \equiv 1 + 2ikf_l(k). \tag{2.4}$$

The only change in the wave-function at large distances due to the scattering is the changing of the phase of the out-coming wave. If we call this phase $2\delta_l$ then:

$$S_l(k) = e^{2i\delta_l(k)} \tag{2.5}$$

where $\delta_l(k)$ is real. In the following the dependence of δ_l on k will be implicit. Coming back to eq. (2.4)

$$f_l = \frac{e^{2i\delta_l} - 1}{2ik} = \frac{e^{i\delta_l} \sin\delta_l}{k} = \frac{1}{k\cot\delta_l - ik}, \tag{2.6}$$

Then for the full scattering amplitude we obtain:

$$f(\theta) = \sum_{l=0}(2l+1)\left(\frac{e^{2i\delta_l - 1}}{2ik}\right)P_l(\cos\theta) = \frac{1}{k}\sum_{l=0}(2l+1)e^{i\delta_l}\sin\delta_l P_l(\cos\theta). \tag{2.7}$$

Coming back to resonant scattering, there is a relation between the fact that σ_l are large when the state are quasi-bound then δ_l must cross $\frac{\pi}{2}$ (or $\frac{3\pi}{2}$), in other word $\cot\delta_l$ must cross 0 (fig. (2.2)). Assuming that $\cot\delta_l$ changes slowly close to a resonance, i.e. $E \simeq E_r$, it is possible to expand $\cot\delta_l$ in the following way:

$$\cot\delta_l = \underbrace{\cot\delta_l|_{E=E_r}}_{0} + O[(E - E_r)^2]. \tag{2.8}$$

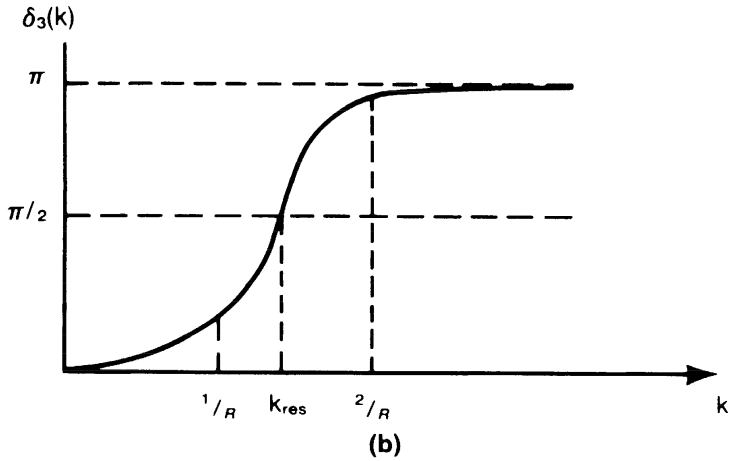

Figure 2.2: *Phase shift δ as function of $k \equiv p/\hbar$. k_{res} correspond to the energy of the resonance [28].*

then:

$$f_l = \frac{1}{k\cot\delta_l - ik} = \frac{1}{k}\frac{1}{k[-c(E-E-r)-i]} = -\frac{\Gamma/2}{k\left[(E-E_r)+\frac{i\Gamma}{2}\right]} \tag{2.9}$$

where Γ is defined by mean of the following equation:

$$\frac{d(\cot\delta_l)}{dE}|_{E=E_r} = -c \equiv -\frac{2}{\Gamma}. \tag{2.10}$$

It is important to observe that Γ is very small if $\cot\delta_l$ changes rapidly. If a single resonance dominates on the cross-section for the l^{th} partial-wave we obtain the formula for the one level resonance (Breit-Wigner formula)

$$\sigma_l = \frac{4\pi}{k^2}\frac{(2l+1)(\Gamma/2)^2}{(E-E_r)^2+\Gamma^2/4}. \tag{2.11}$$

In this case it is allowed to consider Γ as the full width at half maximum, as long as the resonance is narrow enough to neglect the effect of the term $1/k^2$. The main features of the cross-section for a single resonance are the following:

- the cross-section has its maximum $\frac{a\pi}{k^2}(2l+1)$ at $E = E_r$,
- in $E = E_r \pm \frac{\Gamma}{2}$ the cross-section drops to $\frac{1}{2}$ of is maximum value,
- the resonances are narrower for small kR, large l and if $\cot\delta_l$ changes rapidly.

2.2 Kinematical Relations for Elastic Scattering

In the following some kinematic relations for direct and inverse kinematics collisions will be recalled.
M and m denote the masses of the interacting heavy and light nuclei respectively,
E_0 and ϵ_0 denote the energy of the incident particle in the lab system for inverse and direct kinematics respectively,
E_M and E_m denote the energies of the particle M and m respectively after the reaction in the laboratory system in inverse kinematics,
ϵ_M and ϵ_m denote the energies of the particle M and m respectively after the reaction in the laboratory system in direct kinematics,
θ_M and θ_m are the laboratory scattering angles with respect to the beam direction,
Primed symbols denote centre of mass values.

The relation between the energy in the laboratory system and the energy of the centre of mass for direct kinematics is:

$$\epsilon'_M = \epsilon_0 \frac{mM}{(m+M)^2} \tag{2.12}$$

while for inverse kinematics:

$$E'_M = E_0 \frac{m^2}{(m+M)^2}. \tag{2.13}$$

The energies of the light particle for direct and inverse kinematics are the following

$$\epsilon_m = \epsilon_0 \left(\frac{m}{m+M}\right)^2 \left(cos(\theta_M) + \sqrt{\left(\frac{M}{m} - sin^2(\theta_M)\right)}\right)^2. \tag{2.14}$$

$$E_m = E_0 \frac{4mM}{(m+M)^2} cos^2(\theta_M). \tag{2.15}$$

If we consider $\theta_m = 0$, the ratio between the energy of the light particle in inverse kinematics and that one in direct kinematics is:

$$\frac{E_m}{\epsilon_m} = 4\frac{K^2}{(1+K)^2} \simeq 4. \tag{2.16}$$

The energy of the light particle is about four times larger in inverse kinematics than in direct kinematics at the same CM energy. From the experimental point of view this means that in inverse kinematics it is possible to detect lower center of mass energies by having the same energy threshold for the detectors. Moreover, neglecting the energy straggling of particles in the target, the resolution in CM energy is 4 times smaller in inverse kinematics than in direct kinematics.

The energy in the center of mass system for direct kinematics is:

$$\epsilon' = \epsilon_0 \frac{M}{m+M} \tag{2.17}$$

whilst for inverse kinematics it is

$$E' = E_0 \frac{m}{m+M} \tag{2.18}$$

Using the eq. (2.15) it possible to relate the energy of the recoiling particle with the centre of mass energy

$$E_{ex} = \frac{m+M}{4M\cos^2(\theta_m)} E_m. \tag{2.19}$$

Anyway the above relation does not hold when a thick target is used. This is due to the needing of taking into account the energy losses of the incident and recoiling particles in the target.

2.3 The Method.

Elastic Scattering. One way to study the α-structure is through elastic scattering [29, 30]. Basically a beam of α-particles impinges on a very thin target. It is usually possible to distinguish between the elastic and

the inelastic scattering due to the excitation of one of the interacting nuclei. Selecting the elastic (inelastic) channel, when the resonant state, in the intermediate system, is scanned with the appropriate ion beam energy the elastic (inelastic) cross-section shows a strong enhancement. It is possible to measure the elastic (inelastic) cross-section in a range of energies thus obtaining the excitation function, by changing the beam energy by small steps. In general the strongest deviation from Rutherford scattering will be at backward angles where the effects of the Coulomb scattering are the lowest. Moreover, if the excitation function is measured at different angles, it is possible to extract the angular distributions and therefore information on spin and parity of the state can be deduced.

Performing an R-matrix analysis of the experimental spectrum one can extracts energies and widths of the resonances (see chap. 2.4).

Thick Target Method. In the framework of the previous method, in order to obtain an excitation function with a good resolution, it is necessary to perform the measurement by changing the beam energy to very small steps. This operation is very time consuming. It is clear that it is not an efficient method for the systematic survey for many nuclides. In order to solve this problem it is possible to use the backscattering on a thick target [29, 31]. In this case a thick target that slows down the beam particles is used. The reaction takes place at different depths in the target each one corresponding to interactions at different energies. This means that it is possible to induce reaction in a wide range of energies by using a single beam energy. The limit in the energy range that it is possible to investigate at once is given by the first excited state energy of the target nuclei[1]. In fact up to this energy it is possible to distinguish between elastic and inelastic scattering. Since α- particles cross the target two times: entering and exiting (backscattering) the scattered energy

[1]The first excited states of α particles is very high 20.210 MeV

range, determined by the target thickness, must be two times smaller than the energy of the first excited state of the target nuclei in order to avoid superposition in the energy spectra of the elastic scattering. It is possible to obtain a good resolution, better or comparable to that one of α particles detectors [32] as shown in fig.(2.3).

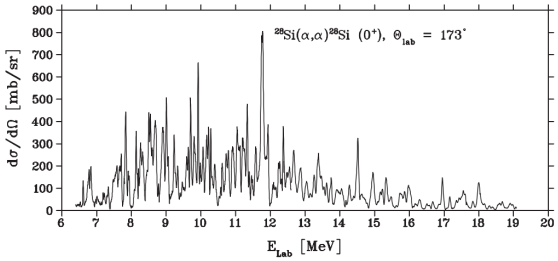

Figure 2.3: *The low-energy part of ^{32}S excitation function at 173° [32].*

Inverse Geometry. In some cases it is very difficult to obtain target of a given material like sulfur or argon or impossible in the cases of exotic nuclei with short half-life. Then, one is obliged to take advantage of the inverse kinematics elastic scattering.

An heavy beam impinges on a target of lighter particles, the light recoiling particles are detected at forward angles corresponding to backward angles in the centre of mass system. Since exotic beams are characterized by very low intensities using a thin target and changing the beam energy by very small steps is hardly possible. Then it is convenient using a thick target [33–35]. As in the previous case, thanks to fact that the beam of heavy particles, crossing the target, loses energy, the interaction can take place at different energies. By knowing the stopping power of the target material for the incident beam and for the recoiling nucleus, it is possible to determine the energy at which the reaction took place. In some case if the target is enough thin and the recoiling particles are very light, e.g. protons, the energy losses of these last in the target can be neglected and the detected energy can be related directly to the centre

of mass energy by means of eq. (2.19). In this case the energy range that can be investigated in one shoot is related to the distance between the ground state and the first excited state of the beam particles. In fact in this case there is no superimposition between elastic and inelastic scattering energies. Fig.(2.4) shows a pictorial representation of an heavy ions beam scattering on a proton target through a resonant state. The

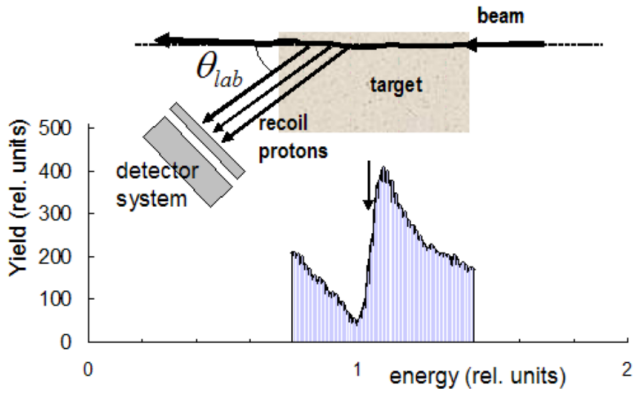

Figure 2.4: *Pictorial representation of proton spectrum elastic scattering in inverse kinematics [33].*

beam enters the target with an energy higher than the energy of the expected resonant state. It loses energy inside the target and reaches the resonant energy. If several detectors are placed at different angles, an angular distribution can be extracted and informations on energy, width and spin of the state can be obtained by means of R-matrix analysis. In order to obtain accurate measurements many effects must be taken into account like energy straggling for beam and for light recoiling particles in the target. Sometimes a catcher (mylar or aluminum) is placed in front of the detectors to stop the heavier particles scattered by the target and energy losses and straggling in the catcher must be considered.

Thick Target Inverse Kinematics Elastic Scattering Method

The method used to study the reaction $\alpha(^8\text{Li},\alpha)^8\text{Li}$ which is the subject

of this thesis is the Thick Target Inverse Kinematics scattering method (TTIK). It was firstly proposed and developed by Goldberg and collaborators [36]. The method is described in ref. [36–39]. It joins the use of the inverse kinematics with the use of a very thick target where the heavy beam particles are stopped. The main advantage of the method is the capability to measure the elastic scattering excitation function in a wide range of energies by using just a single beam energy. The method is very suitable for studies with exotic nuclei and especially for reactions involving low intensity radioactive beam where it is not possible to apply the classical method where the beam energy is changed by very small steps. In the TTIK method the target has a threefold role. It obviously acts as a target, besides this it acts as shield that prevents that the beam hits the detector. Moreover the target acts as a degrader that slows the initial beam energy down to zero. While the beam decreases its energy, scattering events occur in the energy range between the initial beam energy and zero. The recoiling particles, due to their lower stopping power, can cross the target and reach the detectors.

The heavy ion beam particles that own an higher stopping power are stopped inside the target thus the beam does not hit a detector palced at 0° allowing to measure at 180° in the centre of mass system.

A schematic sketch of experimental apparatus involving an extended gas target is shown in figure (2.5) where

R is the radius of the chamber.
z' is the distance between the point **O** in which the beam enters in the chamber and point **P** where the interaction takes place.
z'' is the distance between **P** and the detector.
θ' is the angle of the recoiling particle with respect to the beam direction in the laboratory system.
E_0 is the initial beam energy.

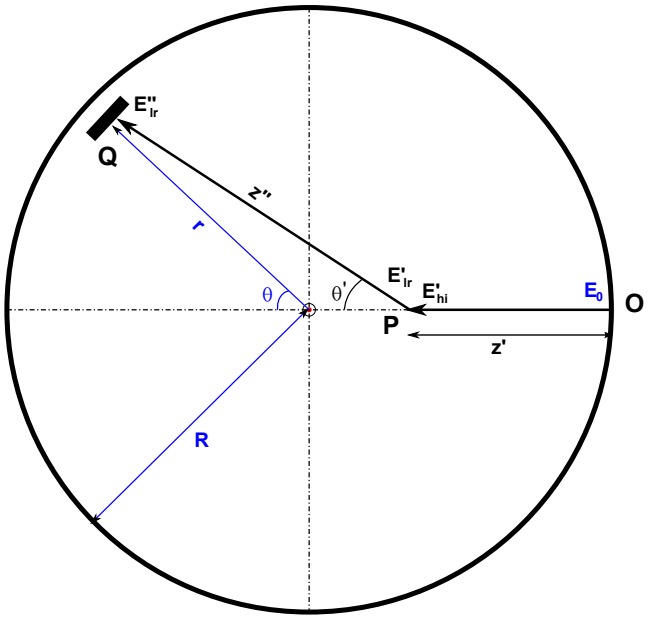

Figure 2.5: *Schematic view of the geometry in the gas target case.*

E'_{hi} is the energy of the heavy projectile at the interaction point **P**, after losing the energy

$$\Delta E_{hi} = \int_O^P \left(\frac{dE}{dz}\right)_{h.i.} dz \tag{2.20}$$

in the He gas target.

E'_{lr} is the energy of the light recoiling nucleus after the interaction which took place in **P**.

E''_{lr} is the energy at the detected point **Q** of the light recoiling nucleus after it lost the energy

$$\Delta E_{lr} = \int_P^Q \left(\frac{dE}{dz}\right)_{l.r.} dz \tag{2.21}$$

in gas the He target .

In order to determine the cross-section $\frac{d\sigma}{d\Omega}(E_{cm}, \theta_{cm})$ for the elastic scattering $m(M,m)M$ it is required to know the energy of the particle when reaction occurred and the angle with respect to the beam direction. Both these information can be obtained from the energy of the recoiling

particle and from the knowledge of the detection point **Q**. Energy and detection point are enough to reconstruct the interaction point **P** and, from this, the energy of the projectile (through the stopping power) at which the reaction was induced and the recoil scattering angle can be recovered. In order to get these information one has to know the energy losses of the heavy beam and the light recoil particles in the gas material. The energy at the detection point can be written as:

$$E''_{lr} = \frac{4Mm}{(M+m)^2}\left[E_0 - \int_0^{z'}\left(\frac{dE}{dz}\right)_{h.i.} dz\right]\cos\theta'^2_{lab} - \int_0^{z''}\left(\frac{dE}{dz}\right)_{l.r.} dz, \tag{2.22}$$

with

$$z_2 = \frac{(Z - z_1)}{\cos\theta'_{lab}} \tag{2.23}$$

where Z is the total thickness of the target corresponding to $z'+z''$ in Fig. (2.5). z' is only unknown variable in the above equation that in principle can be solved numerically. A way to obtained the interaction point, the energy of the interaction, the recoiling scattering angle and the solid angle is then to solve numerically the eq. (2.22). A fundamental part of the work performed for this thesis consists in the writing of a simulation code which allows to obtain the previous information bypassing the numerical solution of eq. (2.22). The details of the simulation will be shown in chap. 6. Once all these quantities are known the differential cross-section can be obtained. Let us first divide the detected energy spectra in bin delimited by energies $E^i_{c.m.}$, $E^{i+1}_{c.m.}$, then the cross section can be written by using the following equation:

$$\left(\frac{d\sigma}{d\Omega_{cm}}(E_{cm},\theta_{cm})\right)_i = \frac{N_i}{4\cos\theta'_{lab} I \Delta\Omega N_{ti}} \tag{2.24}$$

where N_i is the number of detected particles in the i^{th} bin of the centre of mass energy.

I is the total number of beam particles.

$\Delta\Omega$ is the solid angle of the detector in the laboratory system with respect to the interaction point P.
N_{ti} is the effective number of particles in the target slice corresponding to the i^{th} bin of energy:

$$N_{ti} = \frac{N_a \nu}{M_{mol}} t_i^j \tag{2.25}$$

where
N_a is the Avogadro number,
ν is the number of atoms in the molecule,
M_{mol} is the molecular mass of the target,
T_i^j is the target thickness N_{atoms}/cm^2 of the i^{th} slice of the target,
which correspond to the j^{th} channel in the laboratory energy spectrum.

This method requires an accurate knowledge of the stopping power, since from this depends the correct reconstruction of the variables used for the cross section calculation. The effects of a poor knowledge of the stopping power are shown in fig. (2.6). The elastic excitation function for $^9Be(\alpha,\alpha)^9Be$ measured in direct kinematics with a thin target [30, 40] is compared with the elastic excitation function for the same system extracted by using the TTIK method [41, 42]. On the left side of fig. (2.6) the elastic excitation function measured with the TTIK method by using the stopping power data from SRIM [43] is shown. On the right side of fig. (2.6) the same excitation function extracted by using the stopping power measured during the experiment. The effect of stopping power mis-knowledgement is evident. The spectrum is deformed: the position of the resonances is wrong as well as the cross section value that is understimated. In order to avoid this kind of systematic errors a measurements of $^{7,8}Li$ energy loss in ^4He was performed during the experiment, see chap. (5) for details.

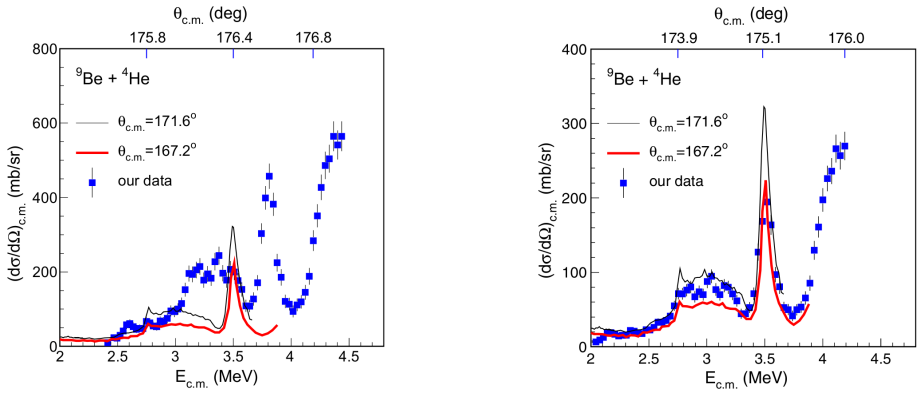

Figure 2.6: *Comparison between $^9Be+\alpha$ elastic excitation function measured in direct kinematics with thin target black [40] and red line [30] and elastic excitation function extracted by using the TTIK method from blue points [41]. The TTIK excitation function was obtained by using stopping power from SRIM-2003 data tables [43] (left) and on the right by stopping power measured during their experiment (right).*

The Time of Flight Measurements. Usually the TTIK method is used when the chosen reaction, like the resonant elastic scattering, is strongly dominant over other reaction channels whose contributions can be considered negligible. When this condition is not fulfilled, prescriptions must be used to distinguish the reaction under study, elastic scattering in this case, from the other reaction channels. One way to do this is to identify and select the recoiling particles in order to exclude other particles produced by other reactions.

Anyway identification does not provide always a good selection, for example does not permit to distinguish between elastic and inelastic scattering. In this case other methods must be used. In this thesis the telescope technique for the identification of the detected particles was used and a time of flight measurement was performed in order to discriminate elastic from inelastic scattering. This represents an important improvement of the TTIK technique because it allows a clear identification of the elastic events. As it is shown in Fig.(2.7) two α particles, produced in an elastic and in a inelastic process can be detected at the same energy.

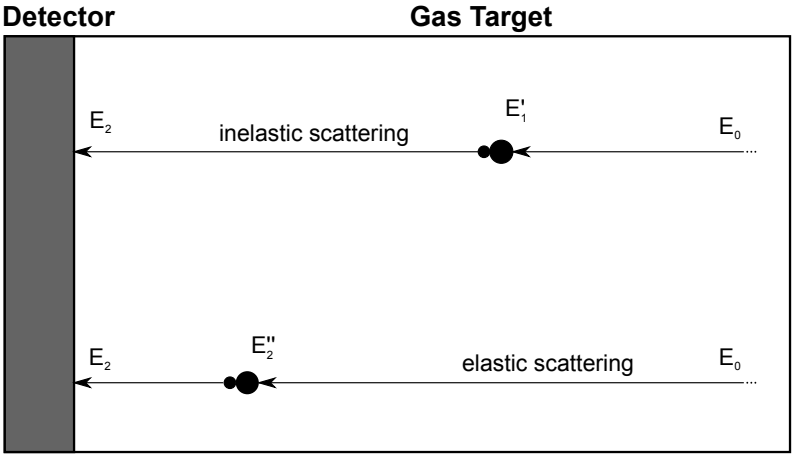

Figure 2.7: *Two beam particles at the same initial energy enter inside the gas chamber. The bottom particle is elastically scattered while the upper is inelastically scattered. Is not possible to discriminate the two processes just looking at the detected energy of the recoiling nucleus. TOF measurement allows the discrimination because its difference for the two processes.*

For example the first is produced by an elastic scattering interaction at a given place while the second is produced at a different place of the chamber by an inelastic scattering interaction. Is not possible to discriminate the two processes by using the only information coming from the silicon telescopes (that is position and energy of the recoiling particle). Anyway if the time of flight between the entrance of the projectile in the chamber and the arrival of the recoiling particle in the detectors is measured it is possible to discriminate the two processes. The use of a gas target implies the use of extended target (in our case the distance between the entrance of the chamber and the detector is about 180 cm) in this way the flight path is large enough to make time-of-flight (TOF) measurements possible. The use of a thin solid target does not allow to perform TOF measurements. On the other hands the use of an extended gas target implies that the scattering angle depends on the depth at which scattering take place inside the target which is *a priori* uknown.

2.4 R-Matrix

The R-matrix theory was introduced by Wigner and Eisenbud [44–46]. At present the R-matrix theory is used in order to describe scattering states resulting from the interaction of particles or systems of particles independently on their nature of nucleons, nuclei, atoms and molecule. Originally the theory was developed in order to describe resonances in nuclear reactions [46]. Anyway, the R-matrix is a very powerful tool also to parametrize not only the resonances but also the non-resonant part of the low-energy cross-section with a small number of parameters [47]. Two versions were developed in the past years. The calculable R-matrix theory that aims to solve the Schrodinger equation and the phenomenological R-matrix theory that aims to parametrize scattering data. In the following we will discuss the last one based on the paper of Lane and Thomas [47].

The basics concepts of the R-matrix theory are rather simple, but the full development of the theory is long and involves a remarkable amount of algebraic manipulations. For this reasons an outline of the theory will be presented. For a full development of the theory one can refer to the paper of Lane and Thomas [47] and to that one of Descouvemont and Baye [48].

R-matrix describes reactions proceedings via formation of intermediate states of the compound nucleus than it is formulated by means of some set of states that can be associated with those of the compound nucleus. In the general formulation intermediate quantities are introduced in order to make the relations between cross-section and states simpler. These quantities are: the scattering matrix $\mathbf{S}$ and the $\mathbf{L}$, Ω, $\mathbf{R}$ matrices. The cross section $\sigma_{cc'}$ is defined as the cross-section for the exit channel c' and the entrance channel c at a incident energy E. The elements $S_{c'c}(E)$ of the scattering (or collision) matrix are the amplitudes of the outgoing

wave for the exit channel c' resulting from incident unit flux relative to the entrance channel c. The cross-section $\sigma_{cc'}$ is proportional to $|S_{c'c}|^2$ (eq. (2.4). The introduction of the **S** is very convenient. Indeed two very general physical principles impose restrictions on any reaction theory for the S-matrix. These restrictions imply two properties of **S**, namely, it must be unitary and symmetric. The peculiarity of the R-matrix theory lies in the fact that **S** can be expressed in term of the matrices **L**, Ω, **R**. The first two matrices are diagonal and take into account the long-range acting between separating nuclei. The R-matrix instead is nondiagonal and takes into account the effects of all the other interactions, that is, those operating inside nuclei (both inside the colliding nuclei and inside the compound nucleus). All three matrices depend on certain parameters a_c. Once these parameters are given, the matrices **L** and Ω are fully determined, while R is unknown. All matrices depend also on a set of boundary condition B_c, one for each channel c. Even if all the parameters E, a_c and B_c are given, **R** is still unknown in general. Wigner and Eisenbud [46] have shown that the energy dependence of any element of **R** can be expressed as follows

$$R_{cc'}(E) = \sum_{\lambda} \frac{\gamma_{\lambda c}\gamma_{\lambda c'}}{E_\lambda - E} \quad , \tag{2.26}$$

where λ labels the members of a complete sets of states and $\gamma_{\lambda c}$, $\gamma_{\lambda c'}$ and E_λ are energy-independent quantities depending on a_c, B_c. The γ_λ are called "reduced width amplitudes" and their squares $|\gamma_\lambda|^2$ as "reduced widths". For each state λ, γ_λ is defined for each c. E_λ are the energy eigenvalue of the state λ.

There are four main assumptions on which the theory is built:

- Applicability of nonrelativistic quantum mechanics.
- It is possible to neglect all process in which more then two product nuclei are formed.

- It is possible to neglect creation and annihilation processes.
- The existence, for each entrance channel, of some finite radial distance of separation a_c beyond which neither nucleus suffers any polarizing potential field from the other.

It is not possible in general to extract the values of γ_λ and E_λ from the experimental cross-section even if a set of a_c is assumed. In order to be able to use the R-matrix theory some broad *a priori* knowledge of the role of the γ_λ and E_λ based on a physical picture is required. Since γ_λ and E_λ depend on a_c, this last must be definite and must have some special physical meaning. Then a_c is chosen to be equal to the sum of the radii of the colliding nuclei ("interaction radii"), which is the minimum value by the forth assumption.

Handling with the compound nucleus, it is possible to assign special properties to the γ_λ and E_λ in order to specialize the R-matrix to the compound nucleus reactions. The resonance levels are found, in nuclear reactions, at energies just above the highest bound state. This is an expression of the fact that in some way the strength of the nuclear forces lets the spectrum of nuclear states persist. In other words, in this energy region the states, although unbound, maintain some of the characteristic of the bound states; the main difference is that they have a finite width Γ due to the fact that they have a finite lifetime $\hbar/\Gamma$. Defining a_c as before, it is possible to associate the E_λ with the energy of the observed quasi-bound resonance states. In particular, if the reaction proceeds through a given resonances it is possible to neglect all the λ but one. This leads to the one-level cross-section formula: the Breit and Wigner formula (eq. (2.11)). At higher energies the resonance become broader and closer overlapping in the continuum. In this case the one-level formula does not hold anymore. But we can use the many-level formula and try to average it over many levels. For this theory one can refer to [47].

Chapter 3

The EXCYT Facility.

In this chapter the production of radioactive ions beams (RIB) by using the Isotope Separator On Line (ISOL) technique is discussed. General properties of the method, production and ionization mechanism, mass separation and post acceleration are put in evidence. The EXCYT facility of Laboratori Nazionali del Sud, INFN, Catania is described highlighting in particular the specific settings that have been used for the ^{8}Li production. ^{8}Li has been produced for the study of the ^{4}He(^{8}Li,α)^{8}Li reaction presented in this thesis.

3.1 Generalities on RIB production.

The radioactive nuclei are of fundamental importance in nuclear physics research and in science applications. The availability of techniques that allow the production of radioactive ion beam makes today possible the study and the investigation of the properties of exotic nuclei in a unprecedented way. The main problems one has to face in order to produce radioactive beams are linked to:

- the very low production cross sections,
- the formation of contaminant species during the production process,
- the very short half lives of the nuclei of interest,

In general there are two complementary ways to produce radioactive beams: in-flight separation technique and ISOL technique.

In both methods the radioactive nuclei are produced from a primary stable beam hitting a target. The exotic nuclei are transported away from the production place, separated from the background of unwanted species and then sent to the experimental set-up.
The first method uses the reaction kinematics, a combination of magnetic and electric fields, and atomic process (energy loss in material), in order to identify the nuclei and to separate them from the primary beam and from the other reaction products [49].
In the ISOL technique, the radioactive species are produced in a thick target where the be3am is stopped and thermalized are thermalized, then the isotopes are extracted and ionized in an ion source. After the extraction, the species are selected by mean of magnetic fields and then they are accelerated up to the desired energy.

The aim of the ISOL systems is to produce beams with high purity, high intensity and very good optical quality in an energy range from very

low energy (few 10 Kev/u) up to intermediate energy (few 100 MeV/u). The key points in the production process are:

- **High Production Rate.** The production cross section for a given ion species is energy dependent. The Primary accelerator has to deliver the highest beam intensity on the production target and this last has to be developed in order to resist to the power deposition of the primary beam.

- **High Efficiency.** The production cross section of exotic nuclei is very small, then every step after the production, like extraction, ionization, selection and transport must be very efficient.

- **Fast Production.** Exotic nuclei have very short half lives, thus all manipulations of the ions have to be as fast as possible to keep the time interval from the production until the delivery to experimental rooms minimum.

- **Purity.** As mentioned before, the production cross section of exotic nuclei is very small compared with that one for stable nuclei, then the last are much more abundant than exotic nuclei. Thus separation process in ISOL technique must be very efficient to separate all the contaminants, stable and radioactive, with high resolution.

3.2 ISOL: basic ingredients.

In the following the key steps required to run an ISOL facility like production, thermalization, ionization, extraction, mass separation, cooling, charge-state breeding and acceleration will be described.

- **Primary Beam and Production Target** A primary beam of light or heavy ions, neutrons or electrons hits a target to produce

the radioactive species of interest through different reaction mechanism. The beam-target combination have to be optimized in order to obtain the highest production cross-section and the lowest amount of contaminants.

- **Catcher** The exotic nuclei produced in the target must be stopped in a gaseous or solid catcher. In most cases the target acts as a catcher. After thermalization the radioactive nuclei escape from the catcher that usually is kept at high temperature ($\sim$2000°) to accelerate the effusion-diffusion process which leads the nuclei to reach the ion source. For gaseous catcher there is no need to heat the gas.

- **Ion Source** Depending on the ion species (atomic properties) several different ionization mechanisms are used. Usually ions are produced with charge state +1 or -1. Usually the target-ion source system is put on a positive or negative high voltage between 40 kV and 60 kV that is used to accelerate the particles in order to extract them from the ion source.

- **Mass Separator** After the extraction from the target-ion system the radioactive beam is purified by a system of magnetics elements. One of the parameter that better determines the quality of the system is the resolving power $R = \frac{M}{\Delta M}$. It can vary from few hundreds to many thousands.

- **Charge-State Breeder** It can be useful to produce a multiple charge state ions beam before the injection in the post accelerator. A charge state breeder performs this operation transforming a single charge ion to a multiple charged ion.

- **Post Accelerator** After mass selection the ion beam is subsequently injected into the accelerator. The beam which has been

accelerated up to the desired energy is finally sent to the experimental rooms.

3.3 EXCYT

In this section EXCYT (EXoticx with Tandem and CYclotrone) facility for radioactive ion beams operating at Laboratori Nazionali del Sud, INFN, Catania will be described [50]. In particular the case of ^{8}Li production which is of specific interest for this thesis will be considered. EXCYT is based on the two-accelerator method (ISOL technique): a

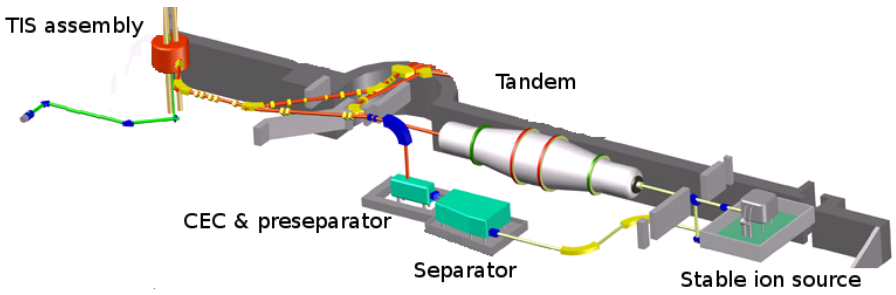

Figure 3.1: *Design of the EXCYT facility.*

primary beam accelerated by the K-800 Superconducting Cyclotron produces, in a target-ion source complex (TIS), the required nuclear species, which will be accelerated by a 15 MV Tandem [51].

The driver accelerator is a superconducting cyclotron ($K_{bending}$=800) fig. (3.2) operating at LNS since 1994 [52].

In order to produce ^{8}Li a primary beam of $^{13}C^{4+}$ accelerated at a energy of 45 MeV/amu was used. A totally new design of the first electrostatic deflector of the cyclotron was done to reach a beam power of 150 Watt. The primary beam impinges vertically on the Target-Ion System (TIS) where the radioactive ions are produced and extracted. The TIS consistes on a graphite target 8.5 mm thick on a tantalum container

Figure 3.2: *View of the cyclotron median plane [50].*

and a positive ion source (PIS) fig. (3.3) both heated up to 2100 °C. The recoils produced inside the target effuse to the ionizer where they are ionized by the PIS. The PIS a surface ionisation source, is highly selective and efficient for alkaline atoms.

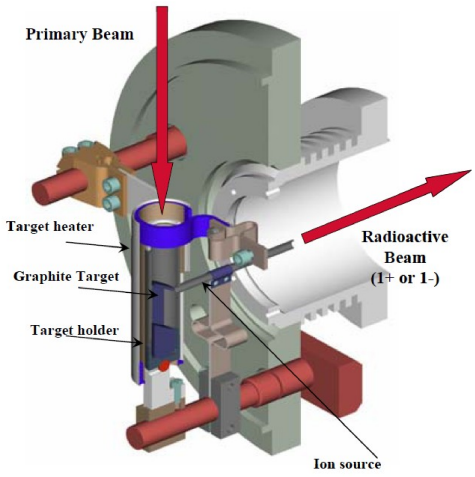

Figure 3.3: *Design of the Target Ion Source assembly [53].*

The purification of the beam is made by means of a mass separator designed as a two-stage separator operating at different potentials [54] plus a preseparator. The ^{8}Li beam was extracted at 25 KeV from the TIS and transported through the two HV platforms.

The pre-separator is placed on the first platform. It was designed with

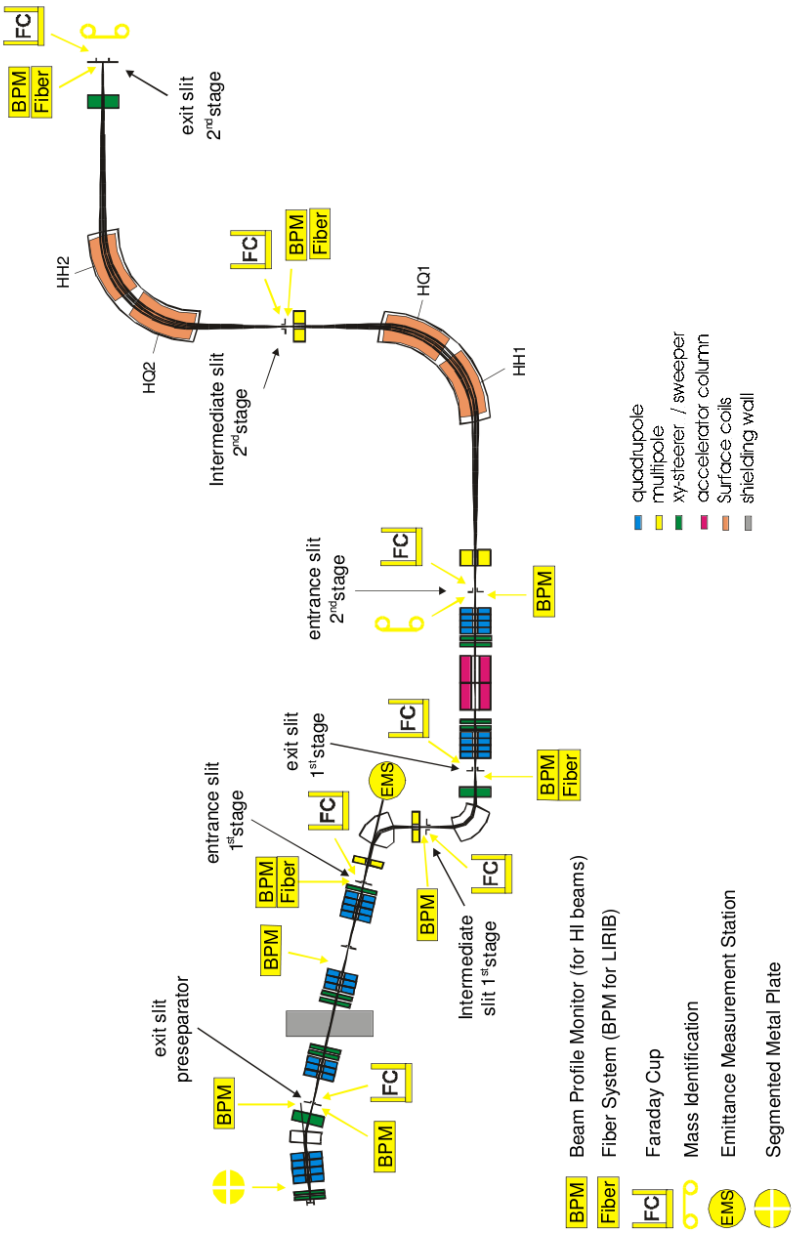

Figure 3.4: *Layout of the EXCYT mass separator [51].*

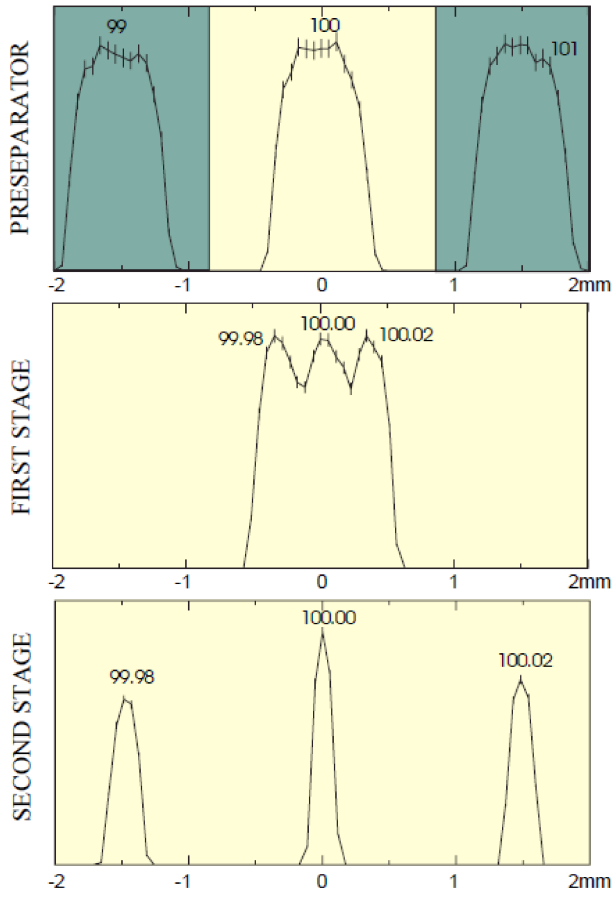

Figure 3.5: *Calculated mass resolving powers for the three separator, stages of EXCYT. After the pre-separator monoenergetic ions of mass 101 and mass 99 could be held back, while ions of mass 100 would be allowed to pass. If the ions of mass 100 would consist of elements that differ in mass by a Q_β-value of 20MeV the first-stage separator could barely separate while the second-stage separator very well separates them from each other [55].*

the aim to confine the bulk of the radioactivity in the zone near the TIS, for this reason it is shielded by a 1 m thick concrete wall. It contains two electrostatic quadrupole triplets guiding the ion beam through the wall and focusing it into a charge-exchange cell, the pre-separator resolving power is $\frac{\Delta M}{M} = 180$. The second HV platform, contains the first-stage separator, with $\frac{\Delta M}{M} \simeq 2000$,and the second-stage mass separator which

is $\frac{\Delta M}{M} \simeq 20000$ which allows to reach the overall mass separation[1]. An example of the resolving powers for the three different stages is illustrated in fig. (3.5).

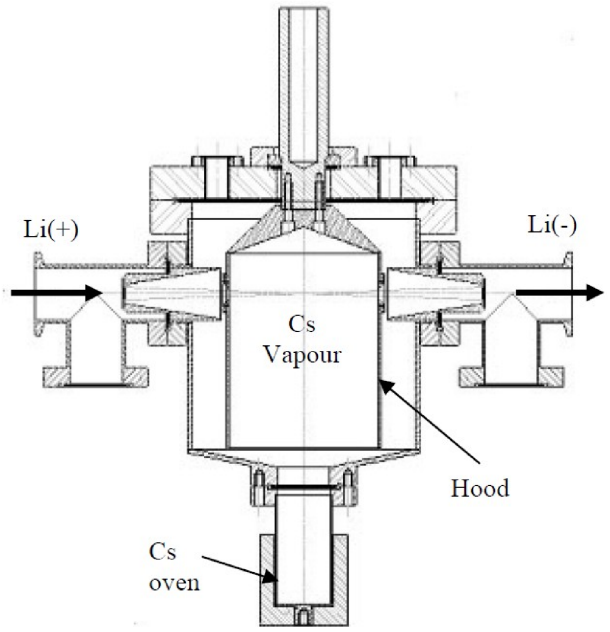

Figure 3.6: *The Charge Exchange Cell.*

Since the post-accelerator (TANDEM) needs to be injected by negative ions, a Charge Exchange Cell (CEC) is required. The CEC is a vacuum chamber containing cesium vapors, see fig. (3.6). Li^+ ions coming from the ion source, interacting with the cesium atoms, change their charge state, becoming negative ions Li^-. The charge exchange consists on a two step process described by the following formulae:

[1]The pre-separator resolving power is enough to obtain a pure ^{8}Li beam

$$Li^+ + Cs \rightarrow Li + Cs^+ \tag{3.1}$$

$$\Delta E = E_i(Cs) - E_i(Li) = 3.89eV - 5.39eV = -1.5eV \tag{3.2}$$

$$Li + Cs \rightarrow Li^- + Cs^+ \tag{3.3}$$

$$\Delta E = E_i(Cs) - E_i(Li) = 3.89eV - 0.62eV = 3.27eV \tag{3.4}$$

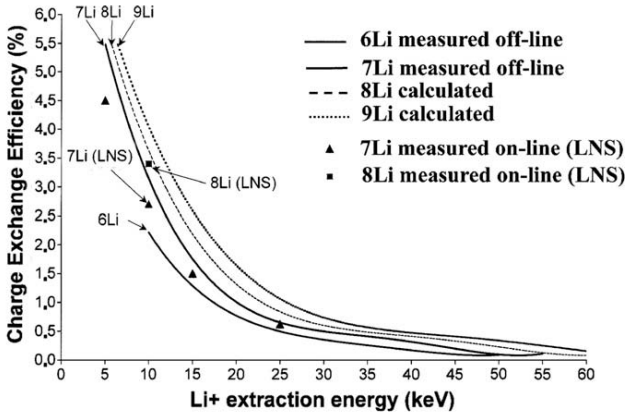

Fig. 6. CEC efficiency versus Li^+ extraction energy.

Figure 3.7: *CEC efficiency versus Li^{+1} isotopes extraction energies [50].*

Since the second step is endothermic, this leads to a rather low efficiency of the process. Cesium is chosen as electron provider because of its low ionization energy. The CEC efficiency strongly depends on the energy of the Li^{+1} extracted from the ion source: the lower is the energy, the higher is the efficiency as is shown in fig. (3.7). There is a maximum around 5 keV, but the beam optics was originally designed to operate at a minimum extraction energy above this minimum: around 15-20 keV. A good compromise between a good quality transmission and CEC efficiency was found at 10 keV for wich the Li^8 CEC efficiency is 3.4% [50, 56].

Finally the ^{8}Li beam is sent to the post-accelerator, a TANDEM-Van Der Graaf which has a maximum voltage of 15 MV, and delivered to

^{8}Li

CEC efficiency	Trough 1^{st} stage separator	Trough 1^{st} stage separator	Trough Tandem coupling line	Trough Tandem	on target
2.8%	100%	100%	100%	47%	70%
$5.4 \cdot 10^{6}$ pps	$1.5 \cdot 10^{5}$ pps	$1.5 \cdot 10^{5}$ pps	$1.5 \cdot 10^{5}$ pps	$1.5 \cdot 10^{5}$	$5.0 \cdot 10^{4}$ pps

Table 3.1: *^{8}Li charge exchange and post-acceleration efficiencies referring to ^{13}C beam at 45 AMeV [57].*

the experimental rooms. At present there are still losses in the coupling line to the tandem, the transmission efficiency depends strongly on the acceleration voltage increasing with the operating voltage. In Tab.(3.1) the efficiencies for the different stages are shown for a stable beam ^{7}Li and for a radioactive beam ^{8}Li.

Chapter 4

Experimental setup and calibrations.

In this chapter the experimental set-up used to measure the ^{4}He(^{8}Li,α)^{8}Li elastic reaction cross-section by using the TTIK method is shown. In particular the detection apparatus made by four silicon telescopes and microchannel plate detector is described.
A description of the acquisition system, with special attention to the logic used for the trigger is given. The last part of the chapter is dedicated to the detectors calibration.

4.1 Experimental Set-Up

The experimental set-up that has been used for the experiment presented in this thesis is sketched in fig. (4.1). The circular scattering chamber CT2000, present at LNS, has been filled by using ^4He with a nominal purity of 99.9999% at a pressure of approximatively 700 mbar. The pressure was continually measured by a capacitance manometer with a precision of the order of 0.3%. The chamber was isolated from the beam line by means of a 13 μm thick kapton foil window. During the experiment a tiny helium gas leakage (most probably from the kapton window) was observed. In order to compensate the pressure decrease and to avoid ^{4}He gas contamination by atmospheric air, the chamber was completely emptied and refilled once each two days.

The measurement of the temperature inside the chamber was provided by a thermocouple within ± 1 K. This last showed no significant temperature variation inside the chamber during the whole experiment. Both temperature and pressure measurements are required to determine the gas density inside the chamber which is needed to calculate the cross-section. The density is obtained by the equation of state of an ideal gas:

$$PV = nRT \tag{4.1}$$

where P is the pressure, V is the volume, n is the number of moles, R is the universal gas constant and T the temperature. The density is

$$\rho = \frac{P}{RT} MW \qquad [gm/cm^3] \tag{4.2}$$

where MW is the molecular weight.

A system of four ΔE-E silicon telescopes was placed inside the chamber and used to measure the energy and identify the recoiling α particles. Each telescope was made of a 50 μm thick silicon detector as ΔE stage and a 500-1000 μm thick silicon detector to measure the residual energy.

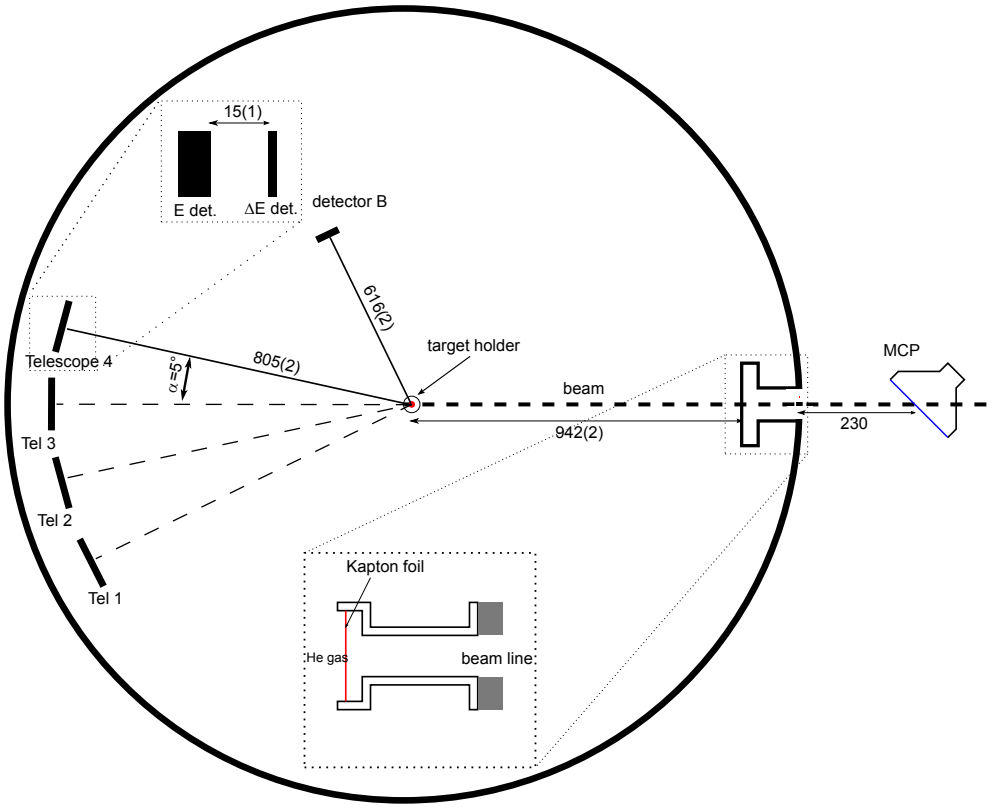

Figure 4.1: *Experimental apparatus. The detection system consists in four silicon telescopes, a silicon barrier-surface detector for the stopping power measurement and a MCP required for time of flight measurements. The chamber was isolated from the beam line by a Kapton foil 13 μm thick. Distances are expressed in mm.*

A silicon surface barrier detector 1000 μm thick was used in order to measure the ^4He stopping power for $^{7,8}Li$ measurement. See chap. (5) for further details.

In order to measure the time of flight between the entering of ^8Li in the chamber and the detection of the recoiling ^4He a reference time was provided by an MCP placed along the beam line just before the kapton window that separates the chamber from the beam line.

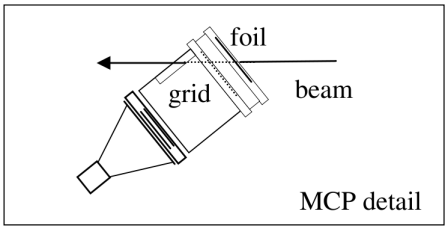

Figure 4.2: *Scheme of the MCP from [58].*

4.1.1 Detectors

In this subsection the detectors used during the experiment will be described in details.

Micro Channel Plate

As it has been underlined in chap. (2.3), the time of flight measurements is crucial for this experiment. The TOF information allows to discriminate elastic scattering from inelastic scattering and from the time-uncorrelated α-particles from ^{8}Li decay (see page (98)). For this reason it is important to have a reference time signal. It has be chosen to use the time signal coming from the beam particles impinging on the MCP detector placed in front of the chamber.
The MCP detector is made of four main parts: a metallic foil, a grid, the microchannel plate itself (chevron configuration) and the anode. The MCP sketched in Fig.(4.2) was assembled with the foil placed at 45° with respect to the beam direction as shown in ref. [59]. The foil is a 30 μg/cm^2 thick C foil coated by a 10 μg/cm^2 LiF layer. The primary electrons are emitted by the foil placed in front of the accelerating grid which improves the secondary electrons emission. The Micro Channel Plate (MCP) detector was required to give a good timing and a high efficiency [58]. The measured MCP efficiency is shown in Fig.(4.3) as a function of the applied voltage. The response of the detector as a function of the rate of the impinging particles was also investigated. Operating at a pressure of 3×10^{-6} mbar, no change in efficiency was observed up to

a rate of 10^6 pps. Operating in the same conditions "dark counts" rate ranged from nearly zero at V=2500 V up to 60 Hz at V=2900 V.

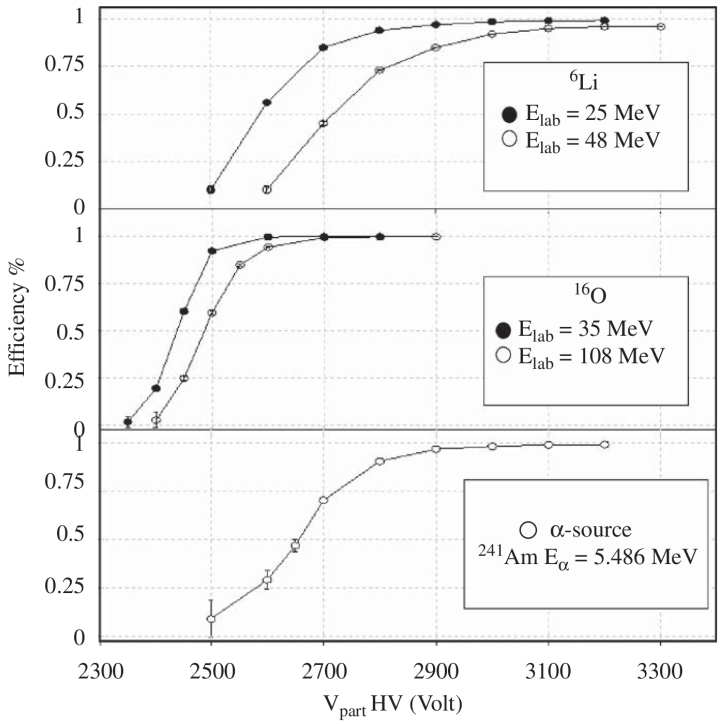

Figure 4.3: *Efficiency of the MCP as a function of the input voltage for different ions: α, ^6Li and ^{16}O error bars, where not visible, are within the dimension of the symbols [58].*

Surface Barrier Detectors

A sketch of the Surface Barrier (SB) detectors, used for the stopping power measurements, is shown in fig.(4.4). It is a 1008 μm thick detector with an active area of 100 mm^2 . The resolution[1] is 74 keV for a 5156 keV α-source of ^{239}Pu. The dead layer of the detector consists in 40 $\mu g/cm^2$ of gold.

[1]the full width at half maximum (FWHM) that includes the electronic noise of the preamplifier.

Figure 4.4: *Surface barrier detector.*

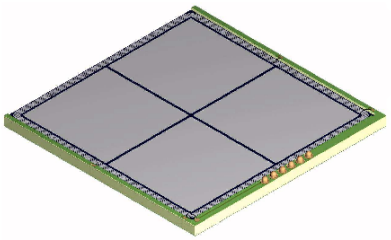

Figure 4.5: *A picture of design G Micron detector.*

Quadrant Detectors

The first stage of the telescopes consists in a Quadrant Detector (QUAD) built by MICRON semiconductor (design G). A sketch is given in fig. (4.5). They are totally depleted ion structures with multi-guard rings for over voltage operation. They have an active surface of 50x50 mm^2 and a thickness of approximately 50 μm The entrance side is divided into four quadrants of 24.975x24.975 mm^2 area. The charge is collected by a 3000 Å thick aluminium electrode. The dead layers of the detector consist in 0.7 μm of silicon for the front side and 0.3 μm of silicon in the back side.

Double Sided Silicon Strip Detectors

The Double Sided Silicon Strip Detector (DSSSD) constitutes the second stage of the telescopes. They are built by MICRON semiconductors (design W1) from n-type silicon and have an active surface of 50x50 mm^2 and a thickness of 1000 μm (telescopes 3 and 4) and 500 μm (telescopes

1 and 2) see fig. (4.1). Each side of the detector is divided into 16 strips, vertical for the front side and horizontal for the back one. A schematic view of a DSSSD is shown in fig. (4.6). On the entrance face of the detector (junction side), the 3.1 mm wide strips are obtained by using p^+ implantation. They are isolated by a 0.1 mm wide silicon dioxide layer grown during the passivation step of the process. The charge is

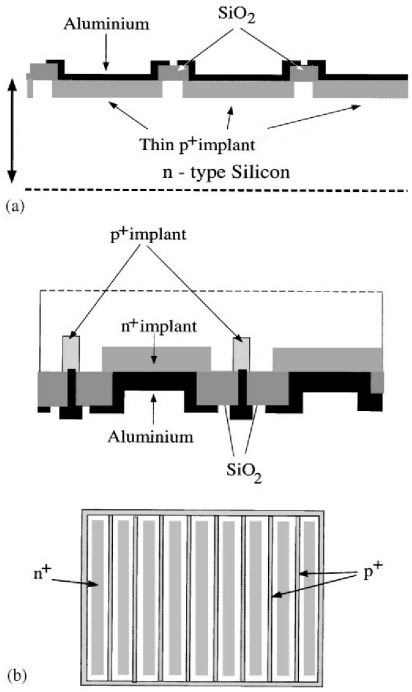

Figure 4.6: Schematic view of the entrance face (a) and exit face (b) of the strip detector. Relative dimension are not corrected [60]

collected on a 3000 Å thick aluminium electrode deposited on the strips. On the back face (ohmic side), the 3.1 m wide strips are obtained by segmentation of a 3000 Å thick aluminium layer evaporated on the anode consisting of a n^+ implantation. These backside strips are isolated by a p^+ type implantation. The edge effects on each side are reduced by the presence of a guard ring which limits the leakage current. The dead layer of the detector is made of 0.5 μm of silicon layer both for the front and

the back sides.

4.1.2 Logic

A schematic picture of the logic section of the electronic is shown in Fig. (4.7). The objective of the experiment is to detect and identify the recoiling α particles coming from ^{8}Li + ^{4}He elastic scattering. Since the ΔE detector thickness is of $\sim$50 μm, α particles which have E $\lesssim$9 MeV do not generate a signal in the second stage detector (DSSSD). So, in order to detect also the particles with E $\lesssim$ 9 MeV, the acquisition is triggered when at least one signal is coming from one of the ΔE stage. As regard as the particle identification we were able to identify them by using the telescope technique for α-particles wich have E $\gtrsim$ 9 MeV. For E $\lesssim$ 9 MeV, the α-particles which stop inside the first stage ΔE can be partially selected by using the time of flight information (see chap. 6). Each particle reaching the ΔE detector produce a signal that is sent to a preamplifier that, in turn, generate two separate signals. The first is a "slow signal" and is sent, after shaping and amplification, to the Analog to Digital Converter (ADC). The second signal is a "fast signal" that is used to generate the trigger for the acquisition system. The "fast signal" is delivered to a Constant Fraction Discriminator (CFD) that generates a logical output signal when the analogical input signal exceeda the threshold. A logic FanIn FanOut module performs an *OR* of all the sixteen ΔE outputs from the CFD giving a NIM output signal if at least one input signal is present. The output is sent to a Gate and Delay Generator (GDG), a gate is opened by the (GDG) and is sent to the ADC as trigger for the acquisition system.
The ΔE fast signal from the preamplifier is also sent to a Time Amplitude Converter (TAC) that is able to convert a time interval into an analogical signal. The ΔE fast signal is used as start. The MCP signals are sent to a preamplifier then to a delay line and to the stop of the TAC. In this

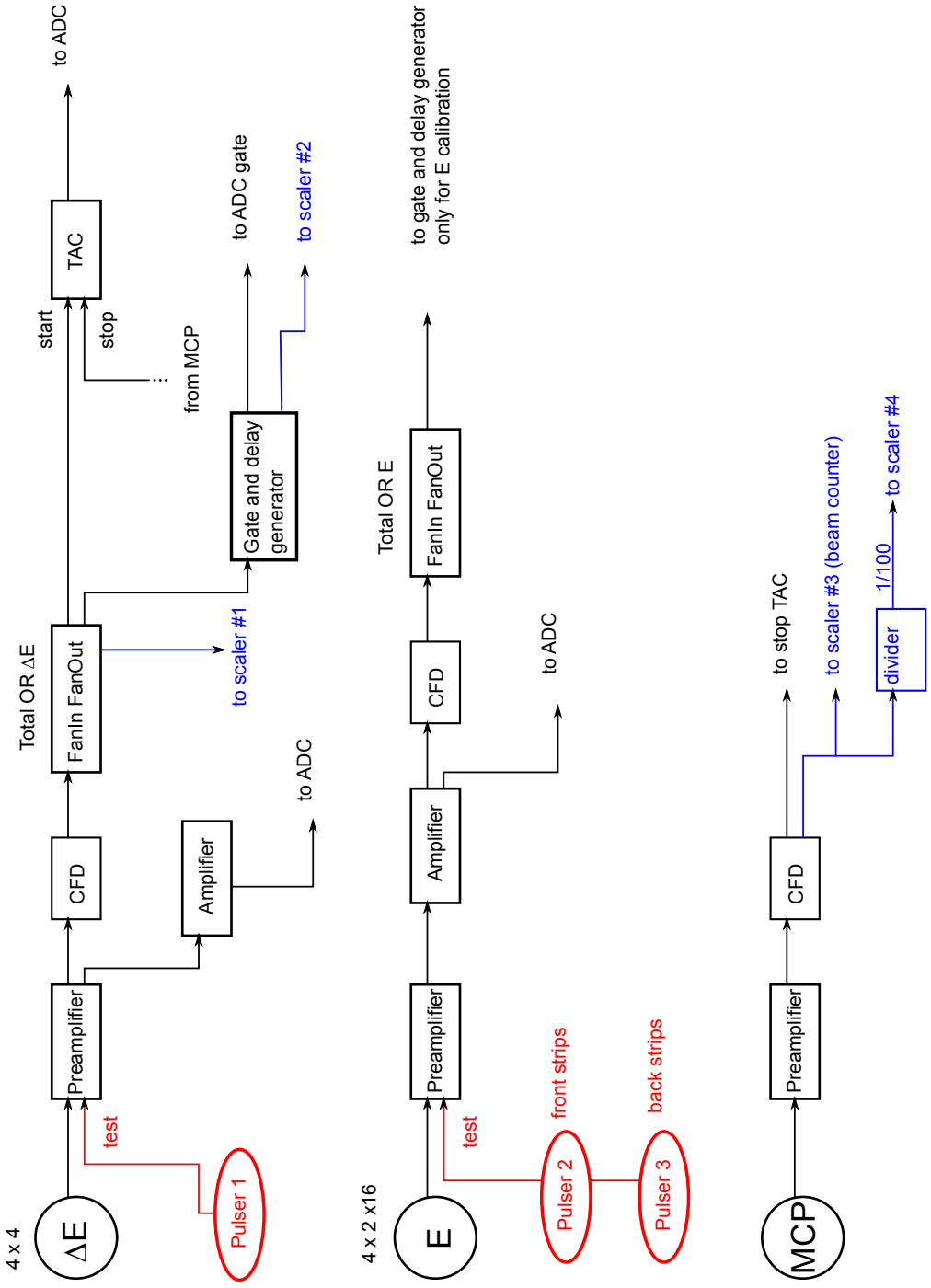

Figure 4.7: *Electronic scheme.*

way we measure the quantity

$$\tau = const - \Delta T \tag{4.3}$$

where ΔT is the time interval between the ^{8}Li crossing on the MCP foil and the arrival on the ΔE detector and *const* is an undetermined constant. The use of the "inverse logic" for measuring the TOF, allows to minimize the dead time. All the beam particles cross the MCP giving a signal (efficiency of the MCP is close to 99% [58]), while just a small fraction generates a scattering event for which recoiling ^{4}He is detected in a ΔE. The configuration where ΔE is used as a start and the delayed MCP signal is used as stop allows the TAC converting just scattering events seen by one detector.

Two signals come from the DSSSD detectors corresponding to the front and back strips hit. Both of them are proportional to the energy of the incident particle and from them it is also possible to determine the position where the particle impinges on the detector. The logic for DSSSD detectors, both front and back strips, is the same as the ΔE. But the trigger generated by the GDG are used just for the DSSSD calibration for which ΔE were removed. The MCP signal was also sent to a scaler in order to count the number of beam particles, quantity required for the calculation of the absolute cross-section.

4.1.3 Acquisition System

The role of the data acquisition system was to convert amplified analogic signals from the detectors into digital signals that can be read, written and stored into a disk. The data acquisition system is composed by two sections. A linux work station allows to read and store data, provides a user interface for setting up and controlling the system and displays on-line spectra. The VME crate houses a Control Process Unit which provides an overall coordination of the system, as the data reading

procedure from the CAMAC front-end. The ADC was working in zero suppression mode. This means that a threshold in volt can be set and for each event that triggers the acquisition only the channels in which signal exceeds the threshold are converted while to subthreshold signals is assigned the value zero (this allows to decrease the overall acquisition dead time).

4.2 Calibrations

An accurate knowledge of the energies of the detected particles is required for a correct events reconstruction. In our case the correct reconstruction of energy is needed, not only to determine the CM energy at which the scattering event occurred, but also to determine the position at which the scattering takes place and thus to calculate the scattering angle. Therefore a systematic calibration procedure was carried out in the framework of this thesis.

4.2.1 Calibrations Set-up

The set-up configuration used for the detector calibration is shown in fig.(4.8). All the angular positions given in the following refers to the centre of the chamber. Telescopes 1 2 3 and 4 were centered at 30° 25° 20° and 15° respectively. All the detectors covered an angular range of $\Delta\theta = \pm 3.6°$. The B detectors was placed at 15° on the right side. The Au target (126 μg/cm^2 thick) was placed in the centre of the chamber. In the following paragraph the analysis of the calibration data will be described in details. Calibration runs were performed at the end of the experiment by using:

1. A mixed isotopes α-source containing ^{239}Pu ^{241}Am ^{244}Cm. In fig. (4.9) a typical α-source spectra is shown.

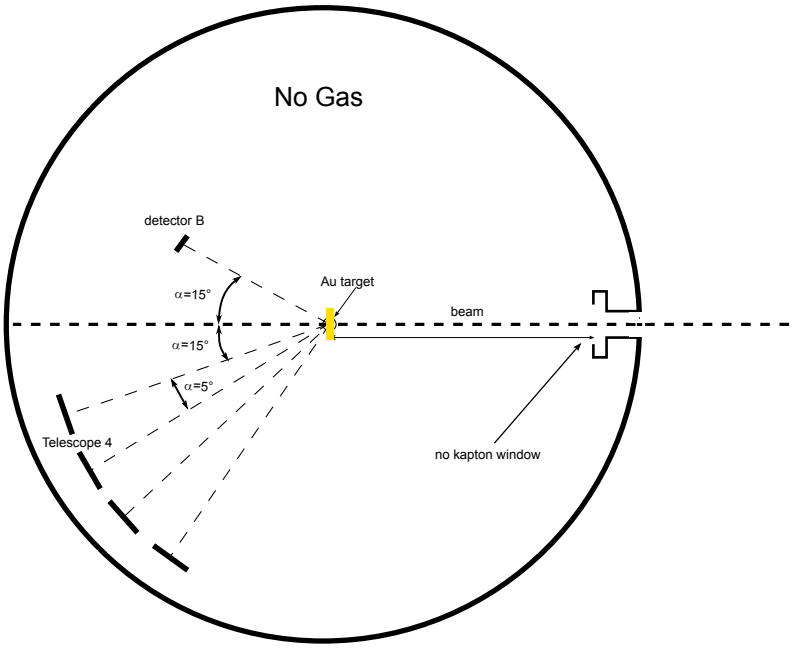

Figure 4.8: *Set-up configuration for detector calibrations. Elastic scattering of ^7Li beam on Au target was used.*

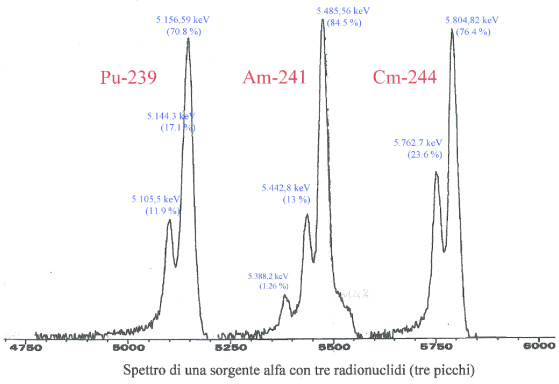

Figure 4.9: *Energy spectrum of the α-source. The yield plotted versus energy in keV..*

2. Au(^{7}Li,^{7}Li)Au elastic scattering at four different energies 10, 14, 22 and 30 MeV.

To perform the calibration there were used also

1. a pedestal run (acquisition of the electronic background),

2. a pulser walk through (PWT) (to check electronics linearity).

The ^7Li beam energy used for the calibration of the ΔE stage were 10 and 14 MeV. For both energies the scattered particles stop inside the detectors. For the E stage calibrations, the ΔE detectors were removed and the ^7Li beam energies used were 10, 14, 22, 30 MeV. It should be noted the the maximum calibration energy is larger than the maximum recoiling α-particle detected energy, in this way the entire experimental energy range was covered by the calibrations.

Pedestal As mentioned in the previous chapter, the used ADC works in "zero suppression". This means that the ADC converts only signals that exceed a given threshold and all the subthreshold signals are converted to zero. During the calibrations the ADC threshold was lowered to zero in order to acquire the pedestal. When a physical event on a given channel of the acquisition system opens a gate the signals of all channels are acquired, in this way the ADC converts the background noise of the system (the pedestal). The value corresponding to the electronic background correspond to a physical events of zero energy. Then the pedestal was used in calibrations as "zero energy point".

Pulser Walk Through (PWT) During the experiment four different pulse generator modules were connected to the input channels of the following preamplifiers.

1. 16 preamplifiers of the four ΔE detectors.

2. 4 preamplifiers (16 inputs) of the front strips of the four DSSSD detectors.

3. 4 preamplifiers (16 inputs) of the back strips of the four DSSSD detectors.

4. preamplifier of the B detector.

The pulse generators sent a signals of fixed frequency and amplitude during the entire measurement. The pulser signal has a twofold role. It represents a reference signal along the whole experiment that can be used to correct possible fluctuations of the signal amplification and it is useful to test the linearity of the electronic chain for each channel. The amplitude and the frequency of the signal can be modified with knobs. For the calibration at the end of the experiment the amplitude of the signal was changed keeping the amplitude multiple of an arbitrary unit, in the following it will be referred to this procedure as Pulser Walk Through (PWT).

4.2.2 B detector

The calibration of the silicon detector B was performed by using the following calibration points

- pedestal (corresponding to zero energy)
- energy from the α-calibration source (5.157, 5.486, 5.805 MeV)
- energies corresponding to ^{7}Li elastically scattered at $\theta = 15°$ from Au target at the four different beam energy of 10, 14, 22, 30 MeV

The energy of the α-particles coming from the α-source are corrected for the energy loss in the dead layer of the detector, see cap.(4.1.1). As regards the Au(^{7}Li,^{7}Li)Au scattering, it was supposed to take place in the middle of the target. In order to obtain the correct ^7Li energy to be used for calibration, for each beam energy it was calculated the beam energy after the first half of the Au target (128 mg/cm^2 thick) the ^7Li recoil energy at the detection angle ($\theta = 15°$) and the energy loss in the remaining part of the target taking in account the correct outcoming angle. Finally the energy loss in the dead layer of the detector

was considered. In fig. (4.10) the linear fit of the calibrations points is shown. On the bottom figure the difference between the experimental points and the linear fit function is shown. In order to exclude that this non linearity can originate from wrong energy losses calculations, this last was repeated in some sample cases by using LISE code [61], no appreciable variations (∼keV) were found. The data show a non linear

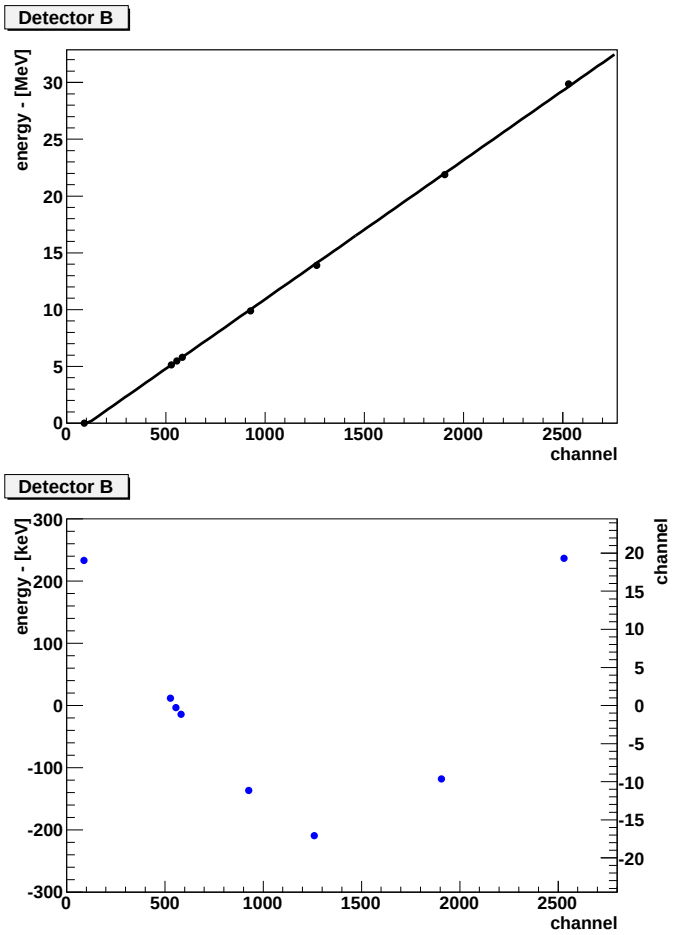

Figure 4.10: *Upper figure: Solid line represents the linear fit of the calibration points (dots) for the detector B. Bottom figure: the energy difference between the energy of the calibration points and the energy calculated by using the calibration equation at the same channel corresponding to the calibration point is shown as a function of the channel number.*

behavior. Also the PWT behavior is not linear fig. (4.11). Although the origin of this non linearity was not understood, in order to correct this

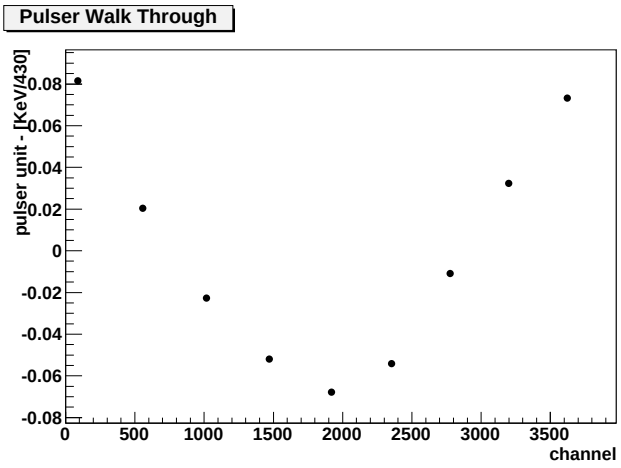

Figure 4.11: *Detector B. The difference between the pulser value of the PWT points and the pulser value calculated by using the calibration equation at the same channel corresponding to the calibration point is shown as a function of the channel number.*

Incident energy	after Au 63 μg/cm^2	kinematics	after Au 63 μg/cm^2	0.3 μ Al	0.5 μ Si
10	9.9698	9.87	9.8346	9.7367	9.5916
33	32.9832	32.55	32.5302	32.4854	32.4182

Table 4.1: *Residual energy for the ^7Li beam after the first half of the Au target, kinematics, second half of the Au target and dead layers of the DSSSD detectors. The calculations were performed by means of stopping power data extracted from the SRIM code [43, 62]. Cross-check calculations were also performed by mean of the LISE program giving results that differs for less then 10 keV [61].*

non linear behavior a quadratic fit for calibration, shown in fig. (4.12), was used. The difference between the energy of the calibration points and those calculated by using the quadratic fit function decreases down to an acceptable level, less than 25 keV (against the 300 keV for a linear function). As it will be shown in the following, this non linearity is present also in ΔE and E detector.

Two examples of energy loss calculation used to determine the energy released in the active region of the detector is illustrated in table (4.1).

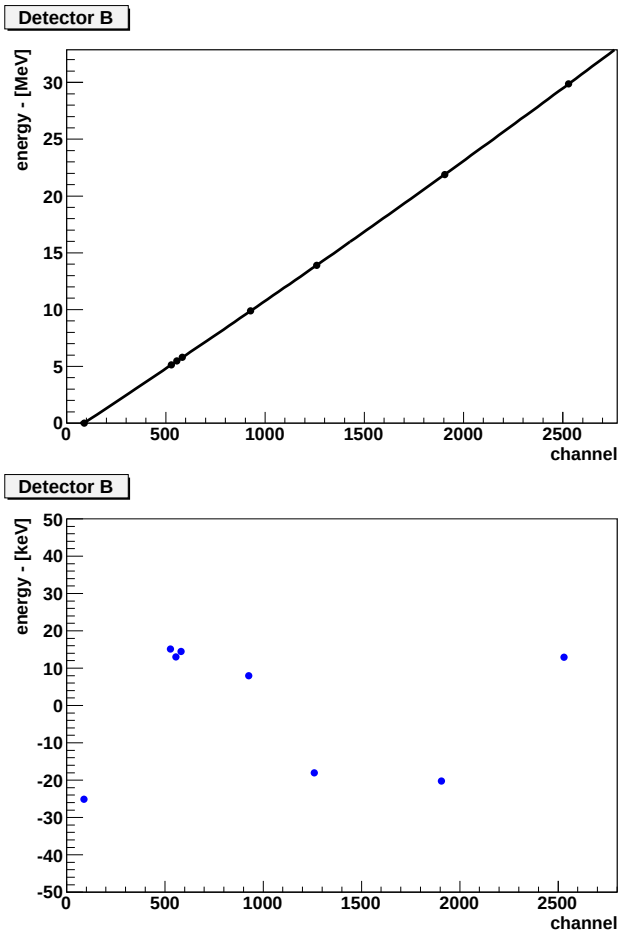

Figure 4.12: *The quadratic fit of the calibrations points for the detector B. On the bottom figure is shown the difference between the calibrations points and the value calculated by using the calibration equation at the same channel corresponding to the calibration point.*

4.2.3 Δ E detectors

For ΔE calibrations the calibration points used are: the pedestal (corresponding to zero energy), the alpha source (5.157, 5.486, 5.804 MeV) and the elastic scattering of ^7Li on Au target at energies of 10 and 14 MeV. Also for the ΔE detectors, the geometry of the α-source and detectors was carefully taken into account in order to calculate the correct energy released in the active region of the detector. The α-particles incidence angle on the detector was determined in order to calculate energy losses in the dead layer of detectors. For what concerns calibrations which involve the ^7Li beam, it was supposed again that the scattering occurs in the middle of the Au target. The energy loss in the first half of the Au target as well as the energy after the scattering at the detection angle and the energy loss in the remaining part of the target (taking into account the correct out-coming angle) was considered. The correction for the energy loss in the dead layer of the detector[2] was also included.

In these calculations it is supposed that the particles (α and ^7Li) impinge on the center of the quadrant of each detector. It was verified that the effect of taking into account the finite dimension of the quadrant (2.5 cm) is negligible[3].

Although the difference between linear and quadratic fit is not large for the sake of coherence we have used a quadratic fit (in ΔE the non linear behavior is evident). In fig. (4.14) the quadratic fit is shown.

[2]this involve the knowledge of the incident angle of the particle in the detector.

[3]i.e. if one considers a particle impinging in the border of a quadrant instead of impinging in the center of the quadrant, the variation in energy due to different scattering angle (kinematics, and difference in the effective thickness of the target and of the dead layer) is negligible, of the order of few keV.

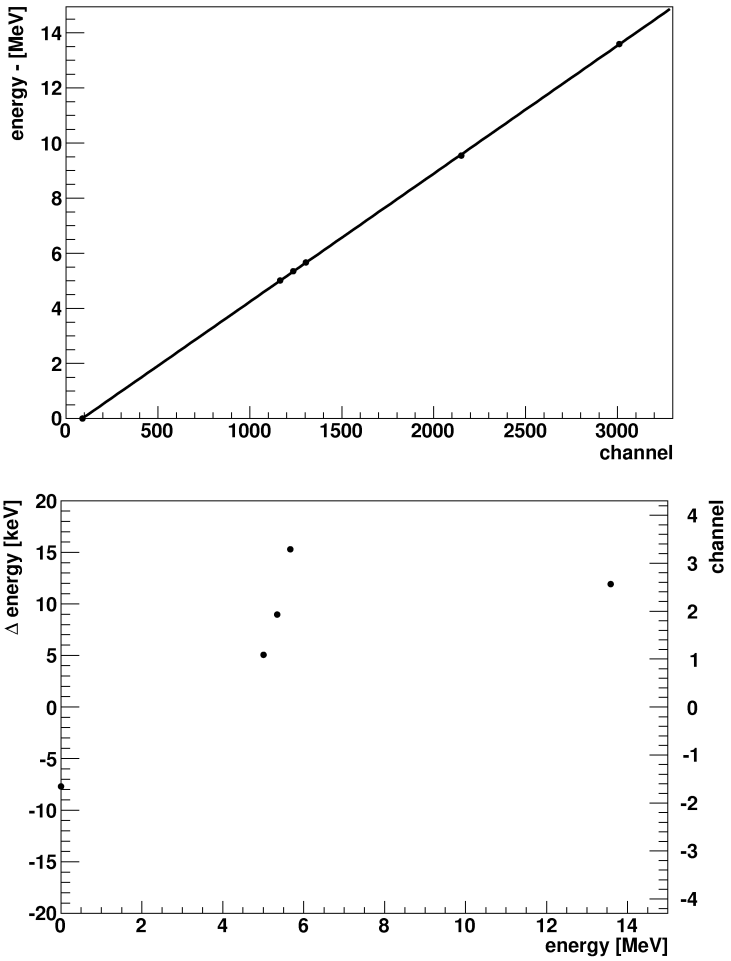

Figure 4.13: *Upper figure: Solid line represents the linear fit of the calibration points (dots) for one quadrant of a ΔE detector. Bottom figure: the energy difference between the energy of the calibration points and the energy calculated by using the calibration equation at the same channel corresponding to the calibration point is shown as a function of the channel number.*

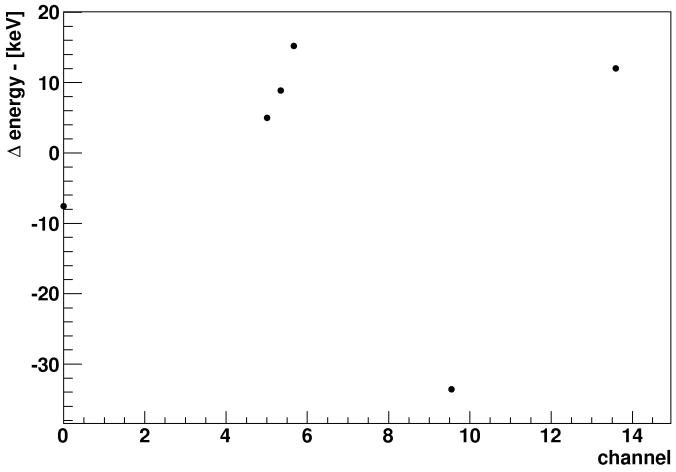

Figure 4.14: *The quadratic fit of the calibrations points for one quadrant of a detector ΔE. The difference between the calibration points and the value calculated by using the calibration equation at the same channel corresponding to the calibration point is shown.*

4.2.4 E detectors

The procedure used for the calibration of the E detectors was similar to the ΔE case. α and ^7Li particles impinging in a single pixel[4] were identified imposing a coincidence signal between one front strip and one back strip. Calculation of the expected energy deposited in the active layer of the detector was performed as in the ΔE case, taking into account the energy loss into the target (for ^7Li calibrations), the kinematics of the scattering and the dead layer (corrected for the incident angle). We

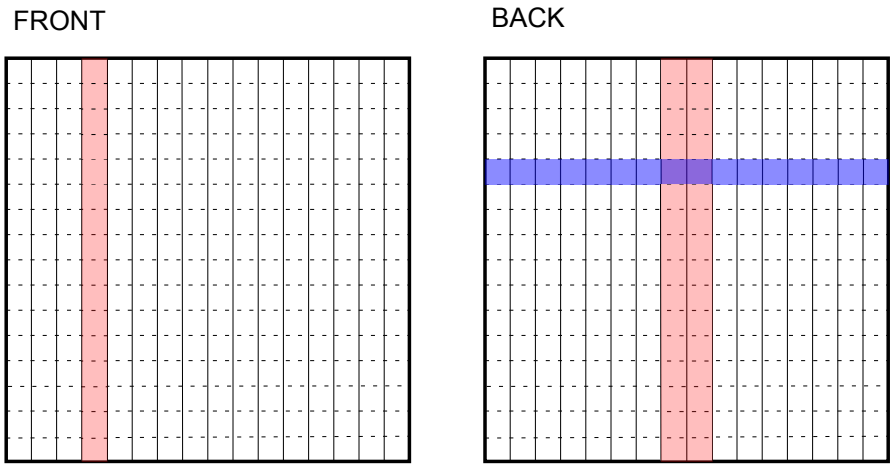

Figure 4.15: *In the front strip case the energy spectra used for the calibration is that one obtained from the entire strip. In the back strip case the energy spread of the particles impinging on a single strip is large due to kinematical effects combined to the fact that dead layer change along the strip. Thus or back strip calibrations the energy spectra coming form only two pixel was used, as shown in the right side picture. Pictorial view of a DSSSD detector. For front strips calibrations of the entire strip was used. For back strip (horizontal) the energy spread of ^7Li particles inside the entire strip is larger then for each strips, so only two pixels were used for calibration.*

observed that the expected (calculated) difference in the energy in the whole front and back strips is small (some keV) so we decide to use the spectrum obtained by using the entire strips. For ^{7}Li beam the expected difference in the particle energy are still small for front strips (vertical

[4]pixel is the overlapping area between a front strip and a back strip.

strip) while for the back strips are larger (up to 60 keV). So we take events coming from two adjacent pixel of the same back strip to calibrate back strips. We observed a non linear behavior both in front and back strips. This is true also for pulser, thus we decide to use as for the B detector a quadratic fit function. After this fit the difference between point and fit decrease to an acceptable level $\sim$10 keV

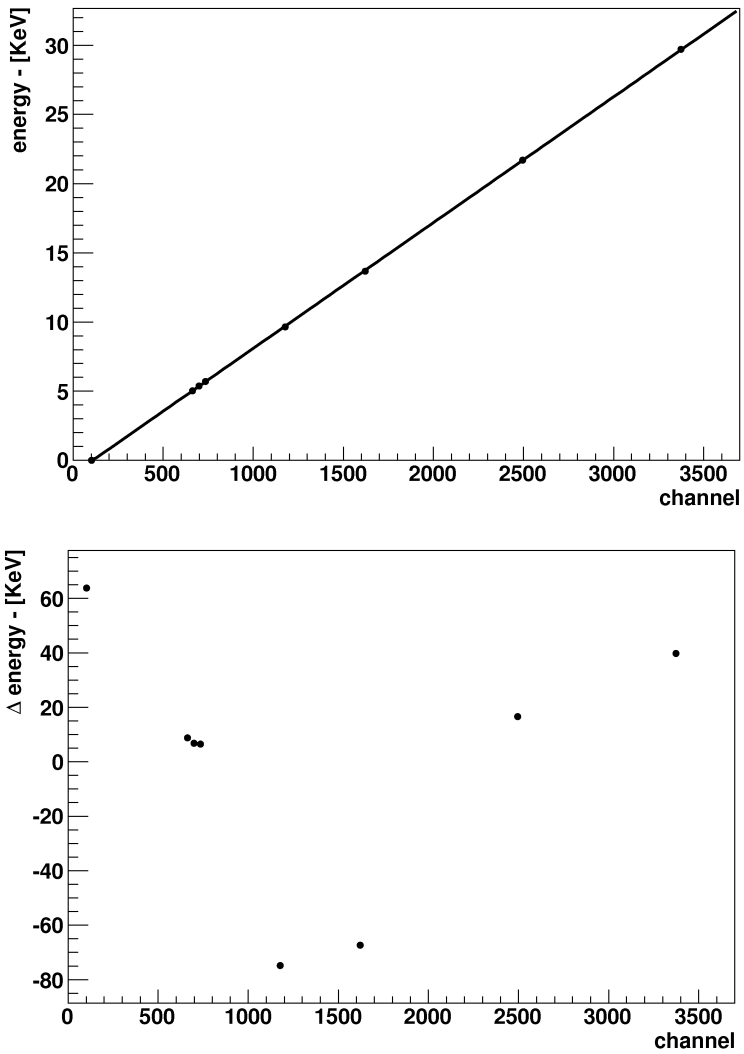

Figure 4.16: *Upper figure: Solid line represents the linear fit of the calibration points (dots) for one front strip of one DSSSD detector. Bottom figure: the energy difference between the energy of the calibration points and the energy calculated by using the calibration equation at the same channel corresponding to the calibration point is shown as a function of the channel number.*

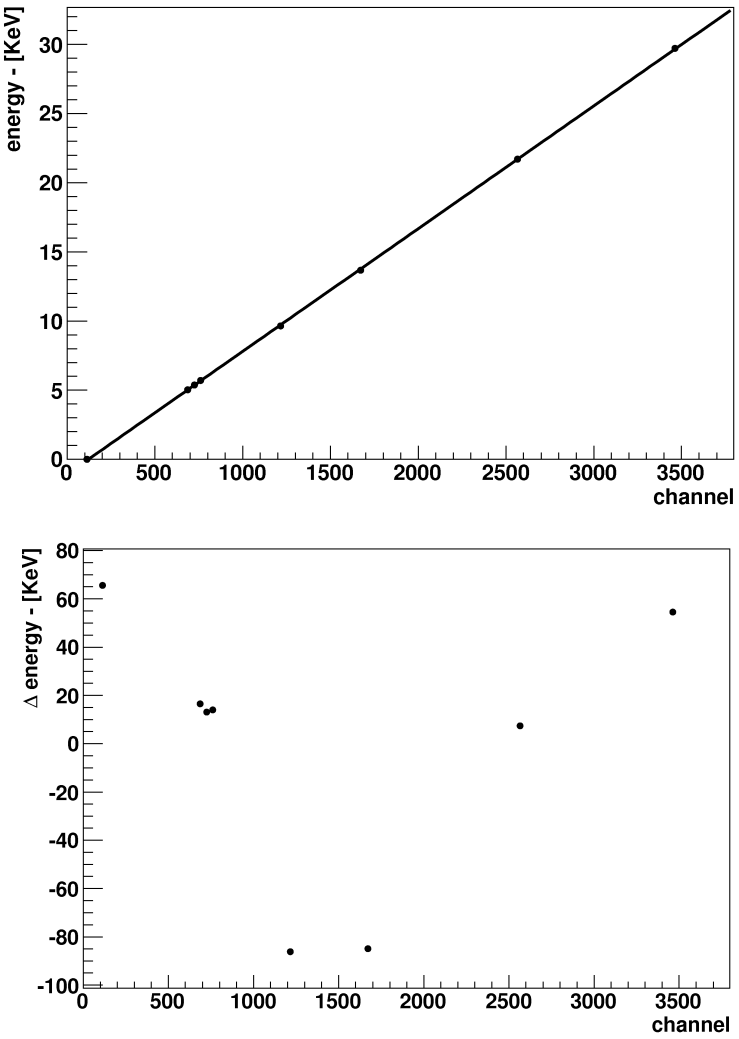

Figure 4.17: *Upper figure: Solid line represents the linear fit of the calibration points (dots) for one back strip of one DSSSD detector. Bottom figure: the energy difference between the energy of the calibration points and the energy calculated by using the calibration equation at the same channel corresponding to the calibration point is shown as a function of the channel number.*

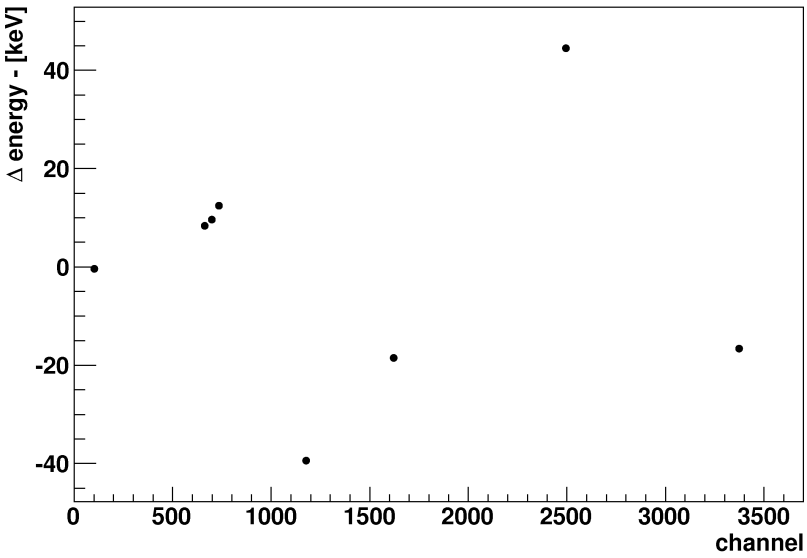

Figure 4.18: *The quadratic fit of the calibration points for one front strip. In the figure it is shown the difference between the calibrations points and the values calculated by using the calibration equation at the same channel corresponding to the calibration point.*

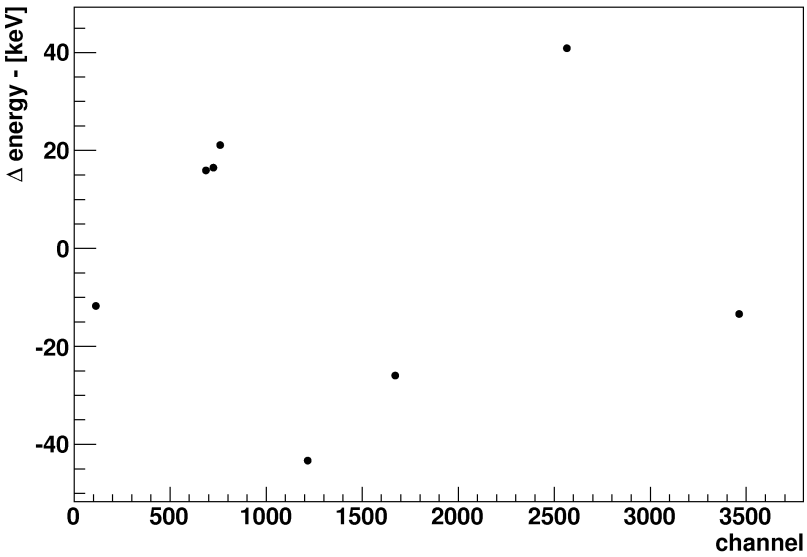

Figure 4.19: *The quadratic fit of the calibration points for one back strip. In the figure it is shown the difference between the calibrations points and the values calculated by using the calibration equation at the same channel corresponding to the calibration point.*

4.2.5 TAC

The TAC calibration was performed by using the ^8Li on the telescope 1 without gas inside the chamber but keeping the Kapton window and the MCP along the beam line. As said before the start signal of the TAC comes from the ΔE detector while the stop signal comes, after a delay line, from the MCP. Then the time measured is $\tau = tof - const$ where *const* is an undetermined constant.

In the fig. (4.20) the central peak corresponds to the time τ for ^8Li crossing the MCP (put just before the chamber entrance) and impinging the ΔE detector. The two left peaks were obtained adding a delay of 16 ns and 32 ns to the start input while the two right peaks were obtained adding a delay line of 16 ns and 32 ns to the stop input. In this way we did not obtain a absolute calibration since *const* is an undetermined constant. Anyway this does not represent a problem because we are interested in relative time (in particular to the time difference between α-particles detected with the same energy but coming out from different reaction mechanisms).

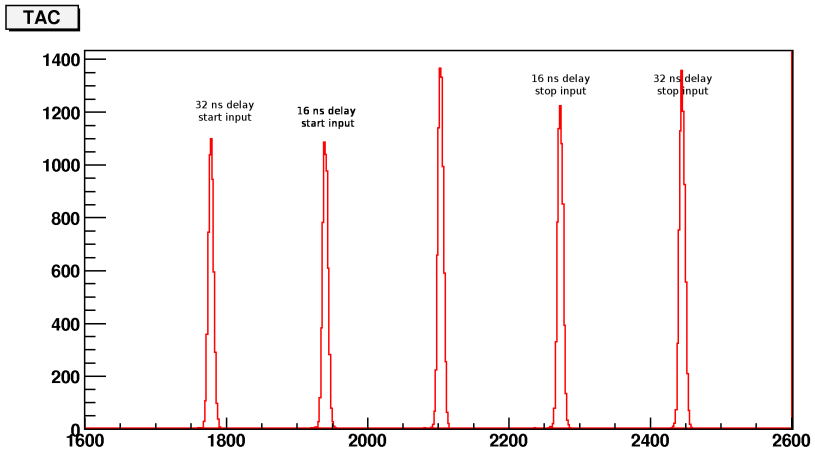

Figure 4.20: *TAC spectrum used for calibrations.*

Chapter 5

Stopping Power Measurement

The importance of an accurate knowledge of the stopping powers in the TTIK method was shown in chap. (2.3). A stopping power misknowledge can deform the extracted excitation function as shown in [41] In this chapter the description and the analysis of the experiment performed to measure the ^{7}Li energy losses in ^{4}He will be given. This measurement, that is complementary to the ^{8}Li-^{4}He experiment, has been performed in order to cross-check the results coming from stopping power calculations of ^{4}He for ^{7}Li. As it will be shown in this chapter the stopping power for high energies depends on the atomic properties of the incident ions then difference among stopping power of different isotopes depends on their mass. So we have remeasured the ^{4}He stopping power for ^{7}Li because it implies less experimental drawbacks with respect to ^{8}Li. The stopping power of ^{4}He gas for ^{7}Li ions was measured by using a direct method from 2 to 23 MeV. The residual energy of ^{7}Li with an initial energy of 30.5 MeV, crossing an increasing helium gas thickness was measured and the stopping power was determined by differentiating the thickness as a function of the residual energy. Results are compared with extrapolation of two semi-empirical codes: SRIM [43] and MSTAR [63]. The results obtained in this thesis are in agreement with SRIM data.

5.1 The method

The stopping power of a given material is defined as the average energy loss per unit path length that a given charged particle suffers by crossing the material [64].

$$S(E) = -\frac{dE}{dx}. \tag{5.1}$$

where dE is the infinitesimal energy loss of charged particles in the infinitesimal thickness dx of the considered material. Energy losses are due to the interaction between the crossing ions and the atomic electrons and the nuclei of the stopping material. It is possible to define an electronic stopping power $-\frac{dE}{dx}_{el}$ and a nuclear stopping power $-\frac{dE}{dx}_{nuc}$. This last one is important only at very low energy[1].

It is common practice to tabulate stopping power in units of MeV/(g/cm^2). The stopping power expressed in such units are called mass stopping power and is denoted as $\frac{1}{\rho}\frac{dE}{dx}$ where ρ represents the density of the medium.

The mass electronic stopping power is defined in term of the inelastic scattering cross-section $d\sigma_{in}(W,T)/dW$ of the incident particle with atomic electrons:

$$\frac{1}{\rho}S_{el}(T) = NZ\int_0^{W_m} W\frac{d\sigma_{in}}{dW}dW, \tag{5.2}$$

where T is the kinetic energy and W is the energy loss of the incident particle. In eq. (5.2) W_m is the largest possible energy loss in an inelastic collision with atomic electrons, N is the number of atoms per gram of material and Z is the number of electrons per atom.
The mass nuclear stopping power is defined in terms of elastic scattering

[1]For example, in water, the nuclear stopping power contributes more than 1% only at energies below 20 keV for protons and below 150 keV for α [64]

cross-section $d\sigma_{el}(\theta, T)/d\Omega$ of the incident particles with the atomic nuclei

$$\frac{1}{\rho}S_{nuc}(T) = 2\pi N \int_0^{W_m} W(\theta, T)\frac{d\sigma_{el}}{d\Omega}\sin\theta d\theta, \tag{5.3}$$

where θ is the deflection angle and $W(\theta, T)$ is the recoil energy received by the target atom. Although in the stopping power calculation used in the present thesis both nuclear and electronic stopping power were taken into account, the nuclear stopping power in our range of energy is negligible.

The mass electron stopping power at high energies can be calculated according to the Bethe's theory with various refinements. The formula for the mass electronic stopping power is

$$\left(\frac{1}{\rho}S_{el}\right) = -\left(\frac{1}{\rho}\right)\frac{dE}{dx}_{el} = \frac{4\pi r_e^2 mc^2}{\beta^2}\frac{1}{u}\frac{Z}{A}z^2 L(\beta), \tag{5.4}$$

where $r_e = e^2/mc^2$ is the classical electronic radius, mc^2 is the electronic rest energy, u is the atomic mass unit, β is the particle velocity in unit ov the velocity of light, Z and A are the atomic number and the atomic mass of the target atom, z is the charge number of the projectile. The quantity L is called the stopping number. It is possible to express it as the sum of three term:

$$L(\beta) = L_0(\beta) + zL_1(\beta) + z^2 L_2(\beta) \tag{5.5}$$

The first term is given by

$$L_0(\beta) = \frac{1}{2}\ln\left(\frac{2mc^2\beta^2 W_m}{1-\beta^2}\right) - \beta^2 - \ln I - \frac{C}{Z} - \frac{\delta}{2}, \tag{5.6}$$

where I is the mean excitation energy of the medium, C/Z is the shell correction, and $\delta/2$ is the density-effect correction. The term $zL_1(\beta)$, Barkas correction, and the term $z^2L_2(\beta)$, Bloch correction, take into account departures from the first order Born approximation on which the Bethe's theory is based. Shell correction becomes important in the

Bethe's formula when the velocity of the incident particle is comparable or lower then the velocity of bound atomic electrons in the target atoms.

The electronic stopping power depends on the atomic properties of the considered nuclei, while the dependence on the mass is included in the dependence on the velocity of the incident particles[2]. Then once the stopping power of a given material is known for a given isotope the extrapolation for other isotopes is quite straightforward. This is shown, for example, in ref. [65] where the stopping power in aluminium for ^{3,4}He, ^{6,7}Li and ^{10,11}B was measured at energies where stopping power is dominated by the electronic stopping power. The measured values are in good agreement with the SRIM simulations [43] indicating that no significant isotopic effects are present.
In the following we will proceed showing that data coming from the SRIM code for ^{7}Li in ^{4}He stopping power are reliable than also their extrapolation to ^{4}He for ^{8}Li stopping power are safe.

The usual way to measure the stopping power consists in using a very thin target and changing the beam energy by very small step (as described, for example, in [66, 67]). In this way for each energy one knows the infinitesimal target thickness dx and the infinitesimal energy lost by the beam dE and it is possible to extract directly the stopping power $\frac{dE}{dx}(E)$ as a function of the energy E.

This method presents two drawbacks: the change of the energy by very small steps and the production of a very thin target. The overall procedure that requires many run with slightly different beam energies is time consuming. On the other hand the production of a thin gas target is rather complex. Usually the gas targets are made by using window gas chamber that contain the gas[3].

[2]Indeed if one express the stopping power as a function of the incident energy instead as a function of the velocity of the particle, the mass dependence appears clearly by using the formula $E = v/2m$.

[3]In order to overcome this difficulty it is used a gas flow effluxing from a small aperture and removed from a differential pumping [66].

The experimental method used in this thesis is described, for example, in ref. [68]. The initial beam energy is kept fixed while the thickness of the target is changed. For each thickness, the residual beam energy is measured after it has crossed the target. Thus the energy loss E as a function of the target thickness is obtained. These points can be fitted by using a polynomial of degree n

$$x(E) = \sum_{i=0}^{n} a_i x^i. \tag{5.7}$$

Once a functional form for $x(E)$ is obtained, one can differentiate with respect to the energy

$$\frac{dx}{dE}(E) = \sum_{i=0}^{n-1} a_{i+1} x^i. \tag{5.8}$$

Since the stopping power is defined as

$$S(E) = \frac{dE}{dx}(E). \tag{5.9}$$

then

$$\frac{dx}{dE}(E) = \frac{1}{S(E)}. \tag{5.10}$$

The advantage of this method is the use of a single beam energy and moreover changing the thickness of the target is very easy, in fact one has just to vary the gas pressure. On the other hand one of the drawbacks is that, since the stopping power is obtained by means of a derivative, in order to obtain a good measurements the step in x must be as small as possible, especially in the energy region where the curvature of the function is maximum, then accurate measurements close to the Bragg peak are difficult.

5.2 Experimental Set-up

The fig. 5.1 shows the set-up used for the stopping power measurement. The MCP was removed from the beam line to reduce uncertainty

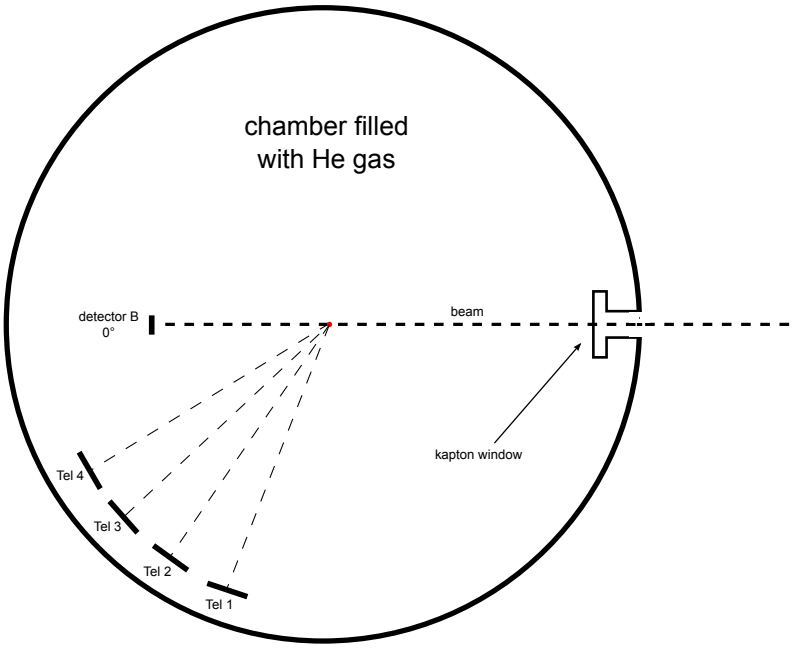

Figure 5.1: *Stopping power measurement configuration. The detector B, described in chap.(4.1.1), is placed at 0° in order to intercept the beam, while telescopes were moved away from the beam direction.*

coming from energy losses in the MCP foil. The surface detector (see chap. (4.1.1)) was placed at zero degree intercepting the beam while the other detectors are moved aside and are not used. The helium pressure initially was zero, then it was gradually increased by steps of 50 mbar for lower pressures and by 5 mbar for higher pressures (for energy losses corresponding to the Bragg peak).

5.3 Analysis

The first step, as said in chap. (5.1), is to obtain the function $x(E)$; where x is the thickness of ^{4}He gas expressed in mg/cm^2 and E is the ^{7}Li residual energy after crossing the thickness x. The fit of the experimental points is shown in fig. (5.2). It was performed by means of a polynomial of degree 5[4].

[4]The order 5 was chosen because it gave the lower reduced χ^2 value.

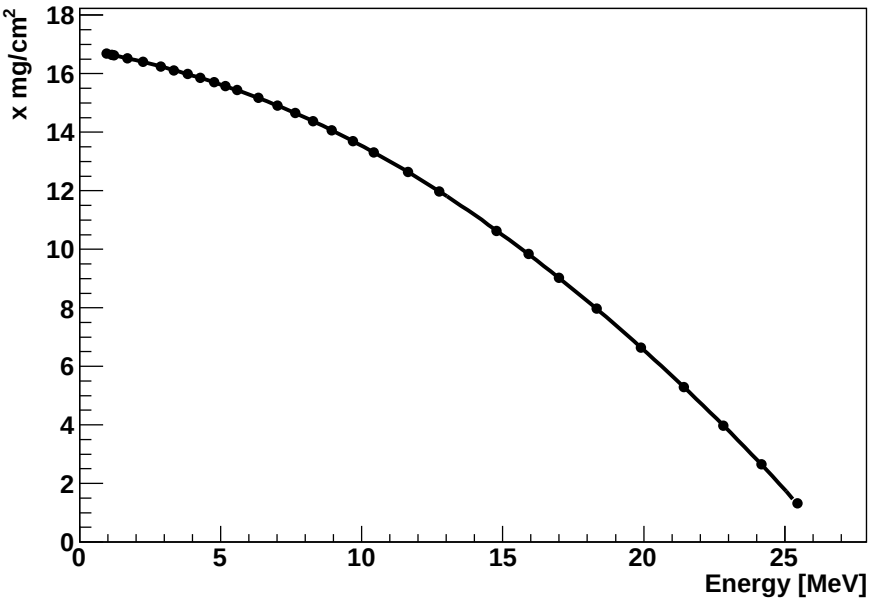

Figure 5.2: *Target thickness in [mg/cm^2] as a function of the residual energy. The line is the polynomial fit ton the data (dots).*

The obtained polynomial was derived with respect to the variable E and its inverse, the stopping power is shown in fig. (5.3). We compare the measured stopping power for ^{7}Li with semi-empirical data coming form two codes: SRIM [43] and MSTAR [63]. It is important to underline that the experimental data on which the two codes are based extend only up to very low energy $\sim$4 MeV. This means that the high energy data are based on extrapolation of low energy data. For the sake of precision during the experiment also the stopping power of ^{4}He for ^{8}Li was measured. Unfortunately during the calibrations variations in the gain of the Silicon detector amplifiers occurred and did not allow to calibrate the detector preventing to extract the stopping power. Moreover a further problem for this measurements comes from ^{8}Li particles implanted on the silicon detector that decay in the channel $^8\mathrm{Li}(\beta-)\rightarrow{}^8\mathrm{Be}^* \rightarrow 2\alpha$. The α-particles have a broad spectrum that extends up to 5 MeV. This represents a strong source of background which makes difficult to have a good quality

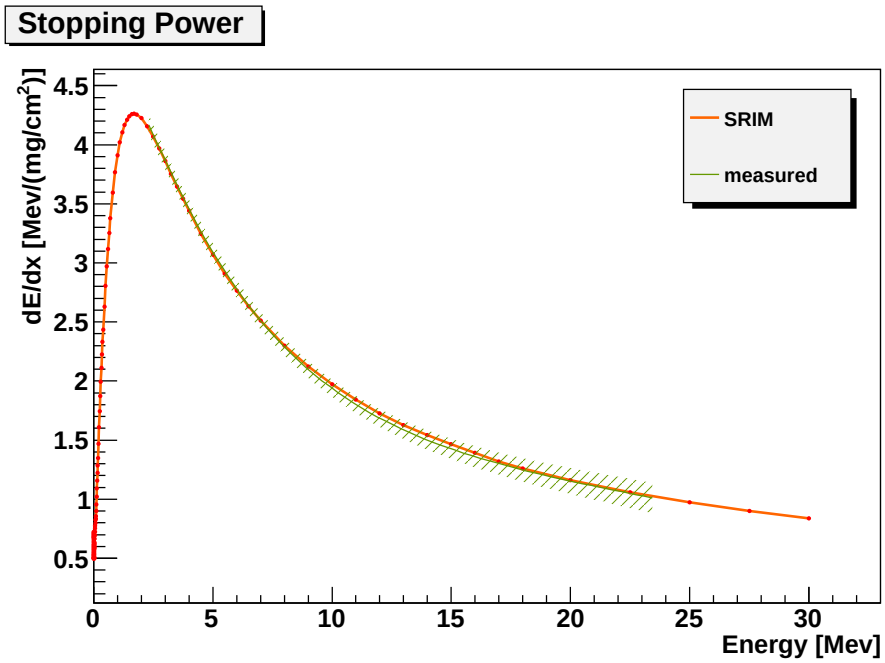

Figure 5.3: *Comparison between ^{4}He stopping power for ^{7}Li extracted from SRIM code[43] (red line), MSTAR[63] code (blue line) and present experiment (green line). The dots represents experimental data on which the two code base their calculation, for references of this last see ref. [43].*

measurements of ^{8}Li low residual energies. For a future measurements a possible way to solve this problem could be the use of the MCP. Taking the events in coincidence with MCP signals, it is possible to select ^{8}Li events from the time-uncorrelated background of the α-decay.

For the analysis of an experiment knowledge of ^{4}He stopping power is important for ^{8}Li as well as for α-particles. Anyway we could not measure it because it is not possible to accelerate ^{4}He beam at LNS by using the TANDEM, since no source is available for the production of ^{4}He negative ions. For this reason the energy losses calculation of α-particles in ^{4}He gas was performed by using the results of SRIM calculations [43]. The semi-phenomenological calculations of SRIM are based on more experimental data with respect to the ^{7}Li data which extend to higher energies ($\sim$ 8 MeV), see fig. (5.5). This makes as confident on the reliability of

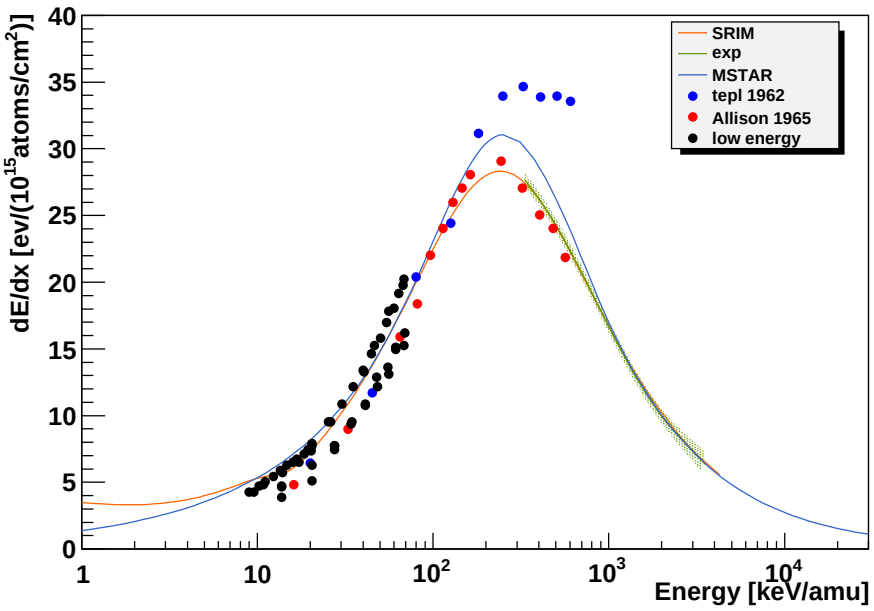

Figure 5.4: *Comparison among ^{4}He stopping power for ^{7}Li extracted from SRIM code (red dots) and present experiment (green line). The band represent the statistical errors coming from fit procedure.*

these stopping powers. Moreover an indirect clue about the validity of the stopping power value come from ref. [41]. In his work Zadro et al. performed a measurement of the elastic scattering excitation function for the system ^{9}Be-α by using the TTIK scattering method. The calculation for energy losses of recoiling α-particles in ^{4}He gas was obtained by means of SRIM data. With these data they were able to reproduce with a good agreement the elastic scattering excitation function measured in ref. [30, 40]. This excitation function had been measured by using the direct kinematics with a thin target which are weakly dependent on energy losses calculation.

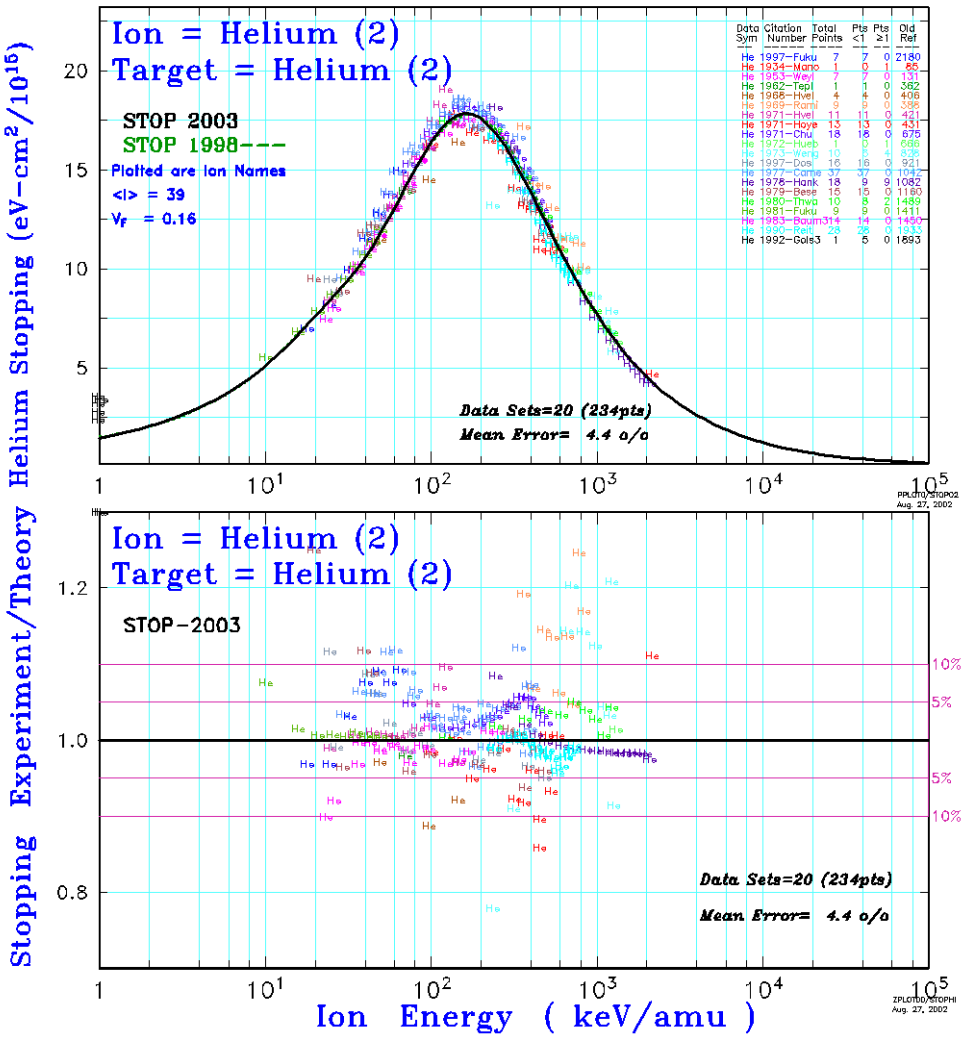

Figure 5.5: *Stopping power for ^{4}He in ^{4}He data from ref. [43].*

Chapter 6

Data Analysis

In this chapter the analysis procedure will be described in details. We distinguished two class of events: those generated by particles stopped inside the ΔE stage of the telescope and those generated by particles crossing the ΔE stage and stopping in the E stage. For both classes the selection procedure used to identify α-particles and the further procedure used to discriminate elastic scattering from other reaction mechanism will be described. Finally the method used to recover the CM energy from the α-recoil detected energies will be explained.

6.1 DSSSD Event Selection

In DSSSD [chap. 4.1.1] the presence of the interstrip gap can affect the charge collection of the detected particles [60, 69–71] decreasing the efficiency for the full energy reconstruction.

In order to investigate this behavior and to individuate a proper event selection procedure, a Au(^7Li,^7Li)Au run (the same used for calibrations) was analized. The plot in fig. (6.1) shows, for each event, on the x-axis the energy of the jth front strip and on y-axis the energy of the ith back strip with $i, j = 1, 2, \ldots, 16$

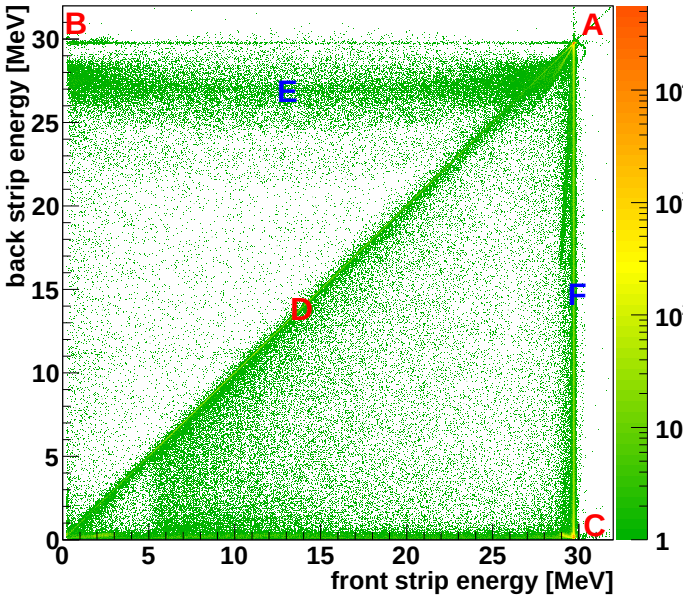

Figure 6.1: *For each event the plot shows all the permutations among the energy of front strips (x axis) and back strips (y axis).*

In this plot it is possible to recognize different loci. Events with energy correctly measured are placed in **A**: both front and back strips give signals of full energy. Locus **C** corresponds to spourious coincidences between the ith front strip hit by a particle and the not hit jth back strip; locus **B** is the opposite. The locus **D** instead is concerns events correctly

reconstructed but with a lower energy with respect to the beam energy[1]. The locus **F** corresponds to coincidences where the front strip gives the correct signals ($\sim$ 30 MeV) while the back strip gives a lower signals, that is back interstrip events. The locus **E** instead corresponds to front interstrip events, but in this case the back interstrip does not give a full energy events (i.e. front interstrip affects also the back strip signals). This is more clearly shown in fig. (6.2) where the coincidence events between two adjacent front and back strips are shown. In the back case we observe the loci $\mathbf{A}_i$ and the $\mathbf{A}_{i+1}$ corresponding to full energy reconstruction. The locus **C** corresponds to particles that give a signal at the same time in two adjacent strips, that is an interstrip events. By summing the corresponding energies coming from the two signals one obtains the correct value for the energy. This means that the back interstrip effects results in a splitting of the signals between two adjacent strips. In the front strip case we can still individuate the loci $\mathbf{A}_i$, $\mathbf{A}_{i+1}$ and **C** but in this case there is a pulse defect and summing the energies coming from two adjacent strips it does not give an event with a correct energy reconstruction.

In order to select data with full energy reconstruction we select events for which front and back energies differ[2] less than $\sim$ 100 keV. This value takes into account the energy resolution of the detectors and the effect of systematic errors from calibration see fig. (6.3),(6.4). If we compare the energy spectra for back and front strips before and after selection it is possible to observe a good agreement between the front and back strips.

In DSSSD detectors it is possible to obtain energy information both from front and back strips. In the following analysis the energy was taken from the back side because the energy resolution was slightly better as

[1]The ^7Li beam was not collimated thus lower energy particles come from gold target frame scattering

[2]The value depend on the single detector

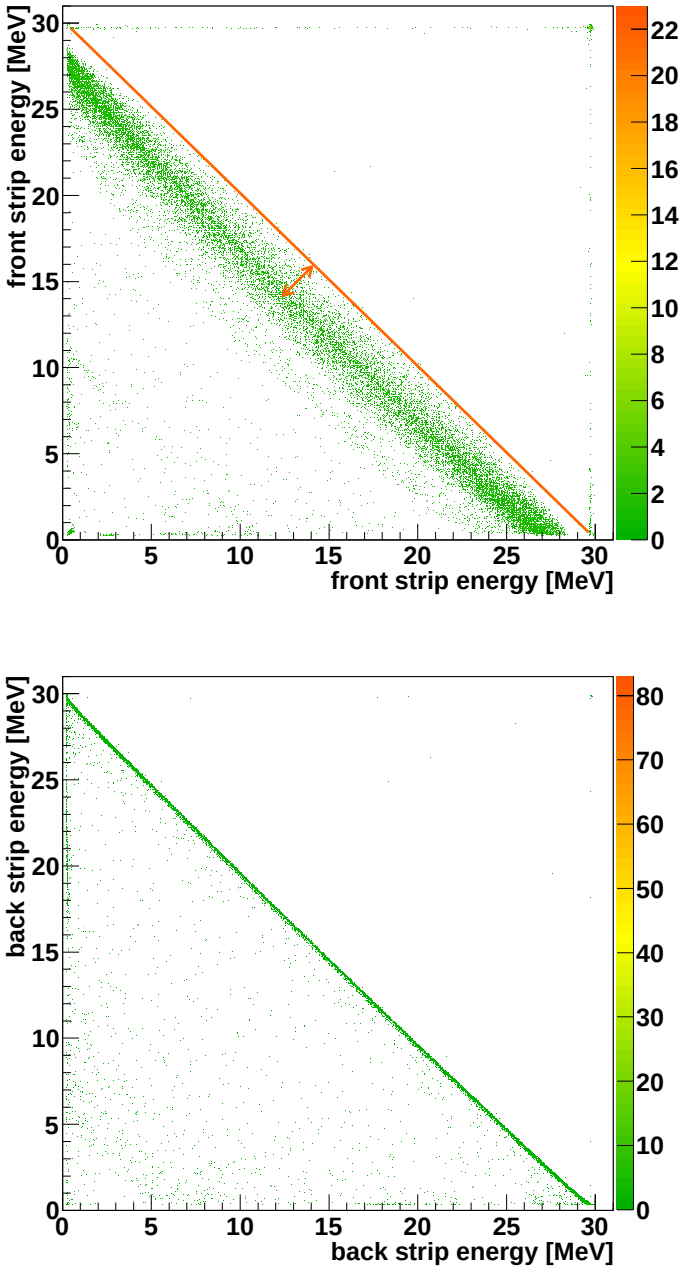

Figure 6.2: *2D-plots, energy for adjacent strips the* $(i+1)^{th}$ *strip versus* i^{th} *for i=1,15. Back strips on the top and front strips in the bottom figure.*

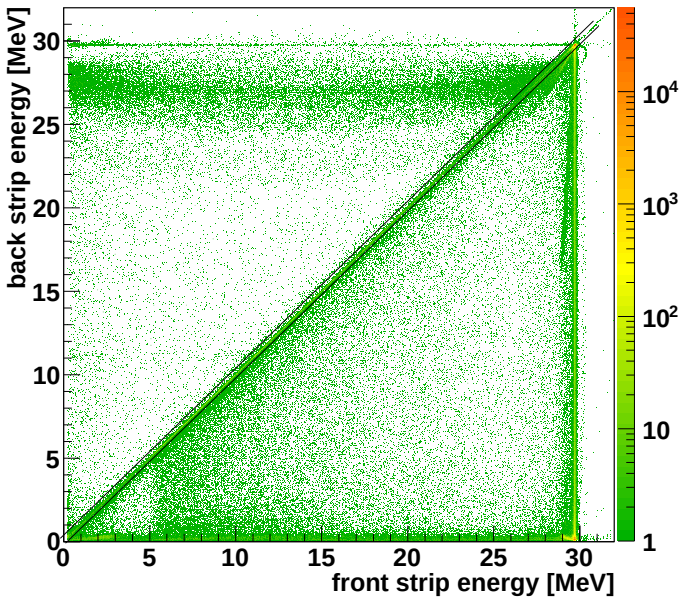

Figure 6.3: *For each event the plot shows all the permutations among the energy of front strips (x axis) and back strips (y axis). The two lines define the locus of selected data for which the difference between front energy and back energy is lower than* $\sim$ *100 keV.*

shown, for example, in fig. (6.5). Resolution was estimated to be 50 keV for back strips and 70 keV for front strips.

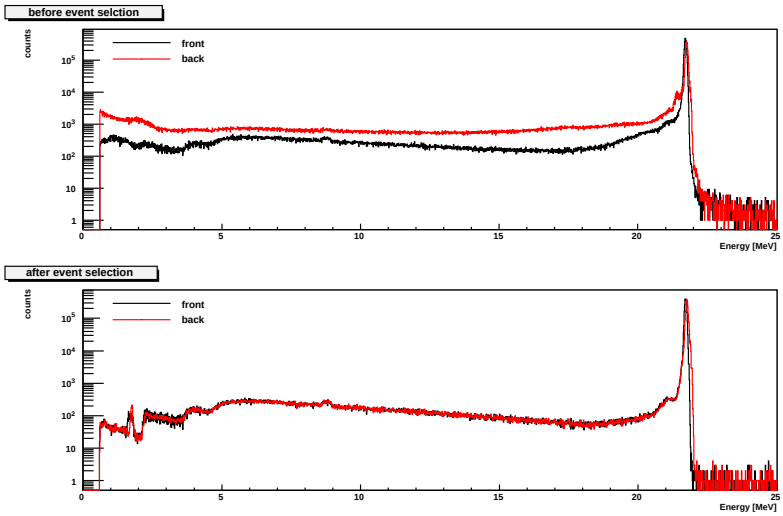

Figure 6.4: *Energy spectra of back (red line) and front (black line) strips obtained for the ^7Li beam energy of 22 MeV. In the upper figure spectra are shown without any event selection. In the bottom figure the events are shown after selection, see fig. (6.3).*

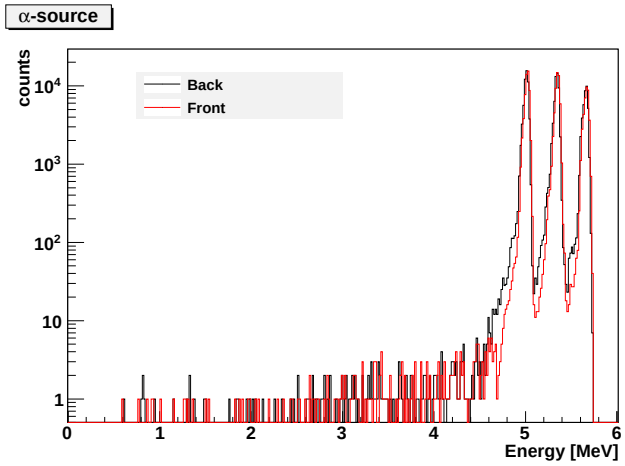

Figure 6.5: *The spectrum of the three α peaks source for DSSSD 3 after the event selection. Red line corresponds to front strips, black corresponds to back strips. Resolution for back strips (∼ 50 keV) is slightly better than for front strip (∼ 70 keV).*

6.1.1 DSSSD efficiency

In DSSSD the strip segmentation is obtained by means of an insulating layer between adjacent strips ($100\mu m$ wide layer of SiO_2). It deeply affects the charge collection on each strip for particles reaching the interstrip region, thus decreasing the efficiency for full energy reconstruction.

As shown in ref [60, 70] the pulse of a particle that hits a back interstrip is split between the two adjacent strips. The charge sharing of particles hitting the front interstrips is very different. Particles entering the detector through the front interstrip can generate pulses in both or just in one of the adjacent strips, but the sum of the pulses is smaller than the pulse produced by a particle having same energy but entering the detector through the central region of a strip [69]. Moreover, as shown in ref. [60, 69] inverted polarity pulses can be generated as well.

A possible model to explain these effects is described in [69]. The flowing charge coming from the leakage current and ionization builds up on the insulating layer of SiO_2 modifying the field between the strips. The modified field and the induction process influence the charge collection on adjacent strips and can generate inverted polarity pulses, making the effective interstrip region larger than the pure geometrical interstrip. Pulse height defect and modified polarity pulse are basically due to the charge produced by the ionizing particles in the region of the modified field. The higher is the charge produced in the modified field region then the higher is the pulse height defect and the higher is the probability to get an inverted polarity pulse. Consequently the efficiency for full energy reconstruction depends upon energy, mass and charge of the incident particle.

Due to the above mentioned effects, the efficiency of DSSSD's was determined by using the calibration run, the elastic scattering of a ^{7}Li beam on Au target at energy of 10, 14, 22 and 30 MeV. We observed that the efficiency ranges between 75% to 85% depending on the particles en-

ergy. This shows that the effective interstrip width is larger than the geometrical one, as already observed in ref. [71]. Moreover the efficiency seems to be different for each detector.
Anyway, because the beam used for calibration was not collimated, it is rather difficult to obtain definitive and safe results. Then for the following analysis we decided to use the geometrical efficiency (94%)[3]. Since the efficiency is supposed to change smoothly with the energy, the effects are just in the cross-section absolute value and do not alter the position or the width of the peaks.

In order to better understand these aspects, a test with the aim to perform a systematic measurement of the efficiency for the reconstructed energy of the DSSSD has been submitted by the candidate to the LNS PAC that approved it. The test consists in scanning different implantation depth by using ^{6}Li and ^{16}O ions at different energies and to investigate the possibility of recovering the energy of the particles impinging on the front interstrip region by measuring at the same time negative and positive pulses. The efficiency extracted will be used for the extraction of the final absolute values of the cross-section.

6.2 Event Selection

In the following, we will distinguish between particles that stop inside the ΔE stage of the telescope and those that stop inside the E stage of the telescopes. The two class of events will be handled in different ways.

6.2.1 α-particles Stopped in ΔE Detectors

In order to extract the elastic cross-section, the development of a procedure that discriminates elastic from inelastic scattering is required.

[3]the strip width is 3 mm while the interstrip width is 0.1 mm both for front and back strips.

In fig. (6.6) the time of flight[4] τ vs detected ΔE energy is shown. The points **A** and **B** represents the punch-through, respectively, of α and lighter particles.

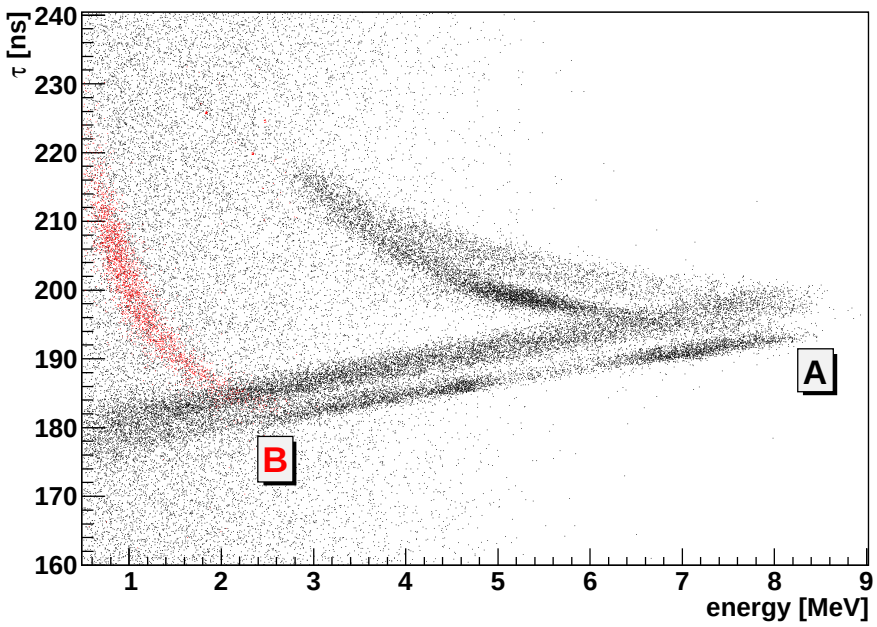

Figure 6.6: *Time versus detected ΔE energy. Events in red correspond to tritons selected by mean of a graphical cut on ΔE vs E plot in fig. (6.7).*

These last were identified as tritons by means of the telescope technique. In ΔE vs E plot, fig. (6.7), a calculations of the energy released in ΔE and E detectors is superimposed on experimental data (black dots). In these calculations the energy loss in the active layer of ΔE and E detector was extracted by using SRIM data [43]. Dead layers in the entrance and exit face of ΔE detector, gas layer between the two stages of the telescope and dead layer of the entrance face of E detector were taken into account. Blue, red and green points correspond to protons, deutons and tritons respectively. The plot shows that triton calculation

[4]See chapter (4.1.2) for τ definition

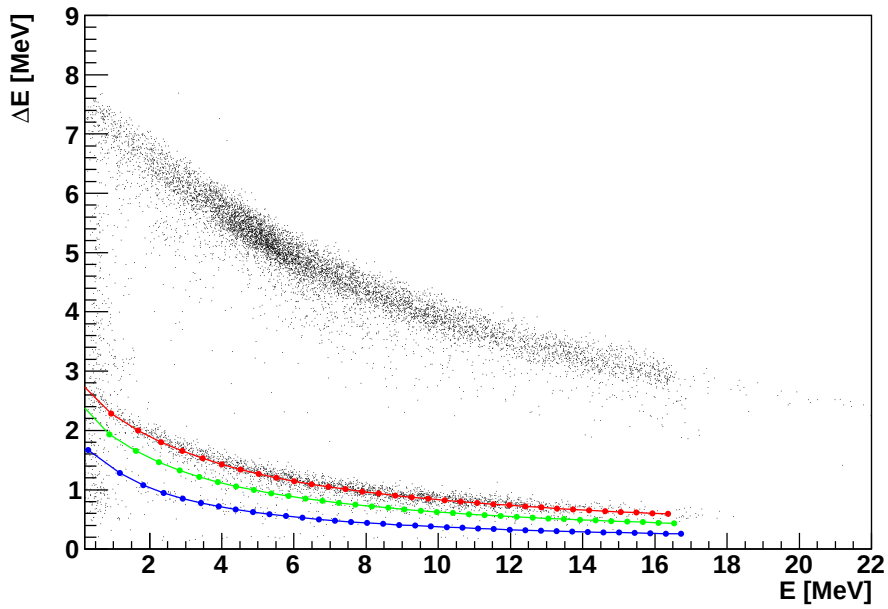

Figure 6.7: *ΔE-E plot. Upper band evevts are α-particles while lighter particles (lower band) are tritons as results from energy losses calculations. Red, green and blue lines correspond respectively to tritons, deutons and protons. Calculations take into account dead layers of detectors as well as gas layer wich lies between ΔE and E stage of the telescope (telescopes are plunged in the ^4He gas).*

fits very well the experimental data. For tritons the origin:
the reaction $^8Li +^4 He \rightarrow^9 Be + t$ which has a threshold of 2.925 MeV [72], triton emission for $^8Li^* \rightarrow^4 He + t + n$ decay with a threshold of 4.499 MeV [72], see ^8Li level scheme fig. (A.1).

In fig. (6.8) calculations for the elastic scattering $^4He(^8Li,^4He)^8Li$ and for the inelastic scattering $^4He(^8Li,^4He)^8Li^*$ are superimposed on experimental data. In the calculation the scattering event was supposed to take place at position **P** (see scheme in fig. (2.5)). The energy loss and time of flight of ^8Li was calculated, see cap. (5) by using the SRIM [43] data, the energy of the recoiling ^4He was calculated for elastic scattering and for inelastic scattering (three first excited states of ^8Li). Energy losses and time of flight of recoiling ^4He were calculated for trajecto-

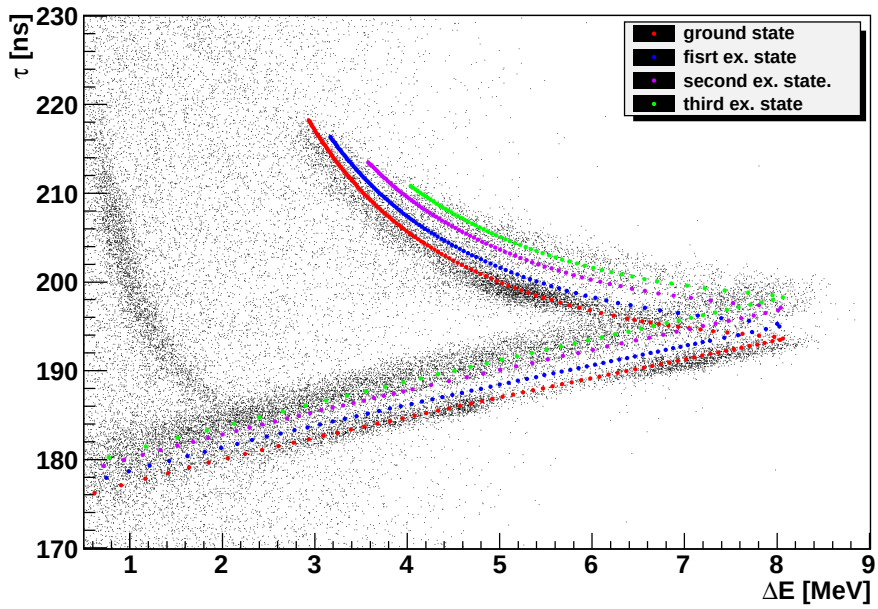

Figure 6.8: *Time versus detected ΔE energy. Calculations are superimposed on experimental data (6.7).*

ries joining the point **P** to point **Q** for each detector quadrant by using again SRIM data. Red points correspond to elastic scattering events, while blue, violet and green points corresponds to inelastic scattering for the first(0.9808 MeV), second (2.255 MeV) and third excited state (3.21 MeV) of ^8Li respectively (see the level scheme in fig. A.1).

The fact that inelastic scattering from the first excited 1^+ state is very low populated is in agreement with the results of Brown et al. [73] and Smith at al.[74] .

As regards other α background events, possible sources are reactions at energies above the ^{8}Li α-threshold emission or reactions on the kapton window. Kinematics calculations combined with energy loss calculations shows that α-particles coming from these sources do not contaminate the elastic α spectrum.

Once the elastic scattering events are identified, we can proceed to

select them by means of a graphical cut directly on the τ-ΔE plot (fig. (6.9)). This procedure is limited to α-particles stopped in the ΔE. The α-selection procedure used for particles which punch through the ΔE detector will be discussed in cap. (6.2.3).
After selection, the events were projected along the energy axis. A further energy cut at low energy (3.1 MeV which represents the punching through energy for tritons for the telescope placed at zero degree) was done in order to exclude tritons contamination. The spectrum was also cut at higher energy (7.7 MeV for the telescope placed at zero degree) to exclude particles that stop inside the dead layers between the two stages of the telescopes. Dead layer are constituted by: a metalization layer (Al) and the proper silicon dead layer for the back side of the ΔE detector and the front side of DSSSD and finally ^4He gas which is between the two stages. One of the consequences of the dead layers is that particles which stop inside the dead layer lose a lower amount of energy and cannot be distinguished by lower energy particles that stop inside the ΔE stage.

In fig. (6.6) one can also observe an time-uncorrelated background at energy below $\sim$5 MeV coming from $^8Li(\beta^-) \rightarrow^8 Be^* \rightarrow \alpha+\alpha$ decay. The reason why these α-particles have a wide energy spectrum is twofold. a) ^8Li decades into the first excited states of ^8Be which is a 2^+-state with an observed width of $\Gamma = 1.23 \pm 0.02 MeV$. [75]. b) Half-life of ^8Li is quite long (840.3 ms) and the ^8Li has the time to thermalize and diffuse inside the chamber, then α-particles can be produced at different distances from the detector, and lose different amount of energy crossing the gas.

The background was sampled as shown in fig. (6.9) in the region of τ where no "contamination" from scattering or reactions is present. The background shown in fig. (6.10) was evaluated as the average of the projection along the x-axis of the red graphical cuts of fig. (6.9).

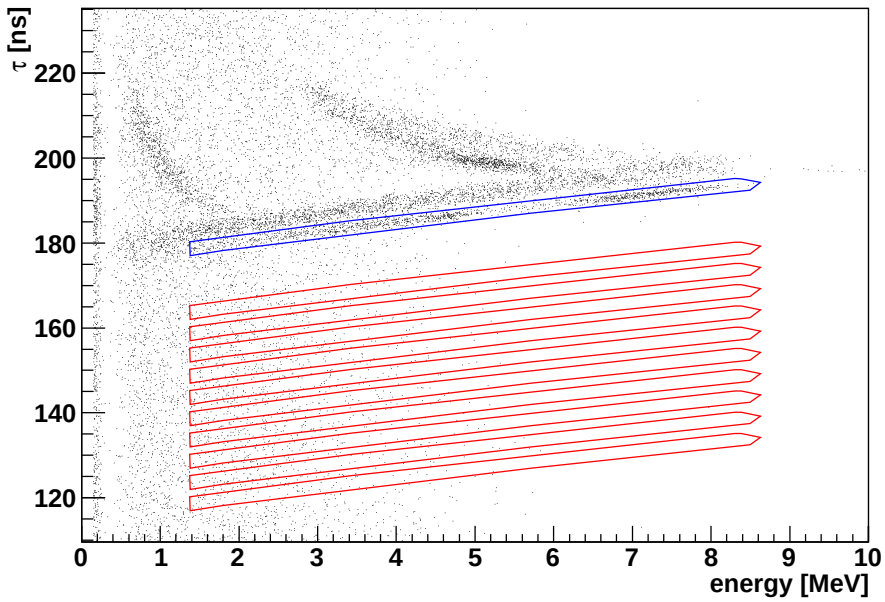

Figure 6.9: *Time versus detected ΔE energy. In blue the graphical cut used to select data. The red cuts, obtained translating the blue line, were used to sample the time-uncorrelated α background. This plot refers to the first quadrant of telescope 3.*

6.2.2 E_{cm} and θ_{cm} Reconstruction for α's Stopped in ΔE Detectors

In order to determine the cross-section we need to associate at each α-particle coming from an elastic scattering event the energy at which the scattering took place and the scattering angle. Instead to solve the integral equation (2.22) the procedure used by the candidate consists on an approximated method based on energy loss calculations for projectile and recoil in the ^4He gas target. In the following, as a first approximation, the assumption of a point like beam cross-section was made and no energy and angular straggling were taken into account. In the calculation the beam enters the chamber with an initial energy of 30.591 MeV (see the scheme of fig. (2.5)), it loses energy crossing the gas up to the point **P**, where the elastic scattering is supposed to take place.

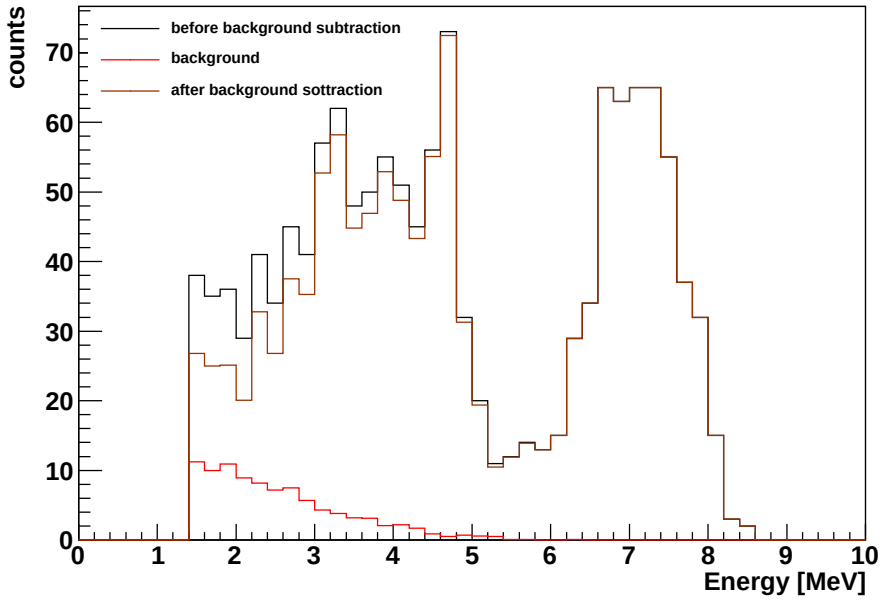

Figure 6.10: *1D-spectrum of detected energy in the telescope 3 quadrant 1 before background selection (black line) and after selection (brown line). The background estimation is red line.*

The trajectory joining the point **P** and the center of each ΔE quadrant **Q** was calculated as well as the energy of the recoiling α-particle. Then the energy loss of the α-particle crossing the distance **P-Q** in the gas was calculated. Energy losses in the detector dead layers were taken into account. An example of this calculation is shown in tab.(6.1). The position of the point **P** was changed by very small steps (from 10 mm to 1 mm depending on the amount of gas crossed) along the beam trajectory. This allows, for each quadrant, to define a set of tables in which the detected energy and the corresponding CM energy are reported. Examples of these calculations for the first quadrant of the detector 1 and 3, are given in tab. (6.2, 6.3)

In this way a relation is created among different quantities:

E_d, detected energy,

E_{CM}, centre of mass energy at which the reaction took place,

	detector 1	detector 3
initial ^8Li energy	30.591 MeV	0.591 MeV
^8Li energy after kapton window	28.65 MeV	28.65 MeV
^8Li energy at point P	13.901 MeV	13.901 MeV
^4He energy after elastic scattering	11.933 MeV	12.336 MeV
^4He energy at point Q	7.089 MeV	7.719 MeV
^4He after Al dead layer	7.045 MeV	7.681 MeV
^4He after Si dead layer	7.968 MeV	7.604 MeV

Table 6.1: *Calculated energy value at different steps of the calculation. From the detected energy (eg 7.968) it is possible traceback the energy at which the reaction took place (eg 13.901).*

θ_{CM}, θ_{lab}, scattering angle in the CM and in the laboratory system,
$\Delta\Omega$, solid angle covered by the detector,
z, position at which the reaction took place from the entrance of the chamber.
Once the quadrant of the ΔE is fixed, in order to obtain the CM energy from a given detected energy an interpolation (4^{th} order) procedure was performed on the tables (6.3).

Let us consider the α-spectrum of fig (6.10), to each energy bin ($E_d^i < E < E_d^{i+1}$) one need to associate a centre-of-mass energy E_{CM}^i to each energy bin ($E_d^i < E < E_d^{i+1}$). The E_{CM}^i is obtained from tables, like tab. (6.3), by interpolating the function E_{CM} versus E_d with a 4^{th} order polynomial in the points $\frac{E_d^i+E_d^{i+1}}{2}$ (centre of the bin). In a similar way, also the parameters θ_{CM}, $\Delta\Omega$, necessary for the cross section extraction, are obtained. In order to determine the N_{ti} of eq. (2.24) the distance z_i is calculated by means of the interpolation for energies corresponding to the beginning (E_d^i) and the end (E_d^{i+1}) of the bin. $\delta z_i = z_i - z_{i+1}$ is the target thickness corresponding to the given energy bin of the spectrum [5] (6.10). Knowing temperature and pressure it is possible to determine

[5] i.e. particles that reach the detector with energy between E_d^i and E_d^{i+1} are scattered in a position z between z_{i+1} and z_i.

		detector 1	detector 3
E_d	detected energy	6.968 MeV	7.604 MeV
E_{CM}	energy in the CM system	4.627 MeV	4.627 MeV
E_{lab}	^8Li energy in the lab system	13.901 MeV	13.901 MeV
θ_{CM}	^8Li scattering angle in CM system	158.9°	176.5°
θ_{lab}	^4He scattering angle in lab system	10.56°	1.753°
$\Delta\Omega$	solid angle	5.00×10^{-5} sr	5.07×10^{-5} sr
z	distance from the entrance of the chamber	1040 mm	1040 mm
τ	time from the entrance of ^8Li in the chamber to the detection of recoiling α in the detector	78.9 ns	77.8 ns

Table 6.2: *Calculated quantities for first quadrant of detector 1 and 3 for ^8Li particles that are supposed to induce scattering event at a distance $z = 1040$ mm from the entrance of the chamber.*

Detector 3 Quadrant 1							
z [mm]	E_d	E_{CM}	E_{lab}	θ_{CM}	θ_{lab}	$\Delta\Omega$ [sr]	τ [ns]
⋮	⋮	⋮	⋮	⋮	⋮	⋮	⋮
1040	7.604	4.627	13.901	176.49°	1.75°	5.07×10^{-5}	77.8
1041	7.587	4.620	13.881	176.48°	1.75°	5.08×10^{-5}	77.9
⋮	⋮	⋮	⋮	⋮	⋮	⋮	⋮
1050	7.430	4.561	13.703	176.44°	1.77°	5.21×10^{-5}	78.2
⋮	⋮	⋮	⋮	⋮	⋮	⋮	⋮

Table 6.3: *Example of tables created to find relations between the detected α-particles energy and different quantities required for cross-section calculation. Energies are expressed in MeV and TOF in nsec. Calculation was performed for z ranging from 0 to 1800 mm.*

density and then transform thickness units from mm to mg/cm^2 (see cap. (4.1)).

For the α-particles scattered close to the detectors, effects due to the size of detectors can be not negligible, and for this reason in the calculations the detectors were divided in fictitious pixels and, for each fictitious pixel, tables like tab.(6.3) were calculated. Anyway still we cannot calculate the cross-section[6] σ for each of these fictitious pixels because we do not know the N_j of eq.(2.24). How to get over this difficulty is described in the following.

If σ_j is the cross-section for the jth pixel of the quadrant and N_j is the unknown number of particles hitting the jth pixel

$$\sigma_j = f_j N_j \tag{6.1}$$

where coefficients f_j are

$$f_j = \frac{1}{4\cos\theta_{lab,j} I \Delta\Omega_j N_{t,j}} \equiv \frac{1}{c_j} \tag{6.2}$$

Then if N is the total number of particles hitting the whole quadrant

$$N = \sum_j N_j = \sum_j c_j \sigma_j \tag{6.3}$$

if we assume that σ_j slightly depends on angle $\sigma_j \simeq \overline{\sigma}$, the following approximation holds

$$N = \sum_j N_j = \sum_j c_j \sigma_j \simeq \bar{\sigma} \sum_j c_j \tag{6.4}$$

then

$$\bar{\sigma} = \frac{N}{\sum_j c_j} \tag{6.5}$$

For each of the fictitious pixels the quantity c_j is calculated eq.(6.2) and the $\bar{\sigma}$ is determined.

Finally the cross-section as a function of the centre of mass energy is obtained, in fig. (6.11) the cross section for the detector 3 placed at zero degree. The error including only the statistical error.

[6] In this context for the sake of brevity σ denote the differential cross-section $\frac{d\sigma}{d\Omega}$

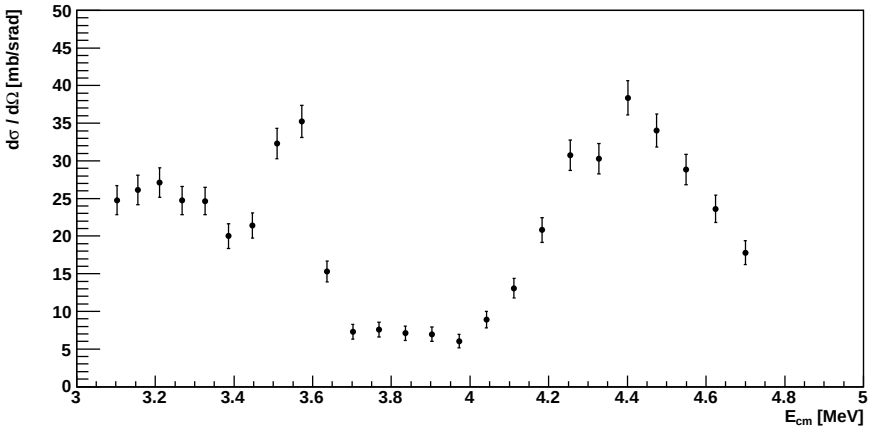

Figure 6.11: *Cross-section as function of the CM energy for the telescope 3.*

6.2.3 α-particles stopped in E detectors

This section is focused on particles which cross the ΔE stage. Even if DSSSD detector have a high granularity, each detector has been divided in four quadrants, in order to accumulate enough statistics it was decided to join all the pixels corresponding to the same quadrant. In such a way also the DSSSD detectors are divided in quadrants. This is possible because the angular range spanned by the DSSSD detector is small. Indeed particles crossing ΔE detector and reaching the E detector are the most energetic, this means that they are produced in elastic scattering events that take place far from the detector. The angular opening covered by a quadrant of DSSSD varies from 0.8° for E_{det}=16 MeV up to 1.9° for E_{det}=0.5 MeV

In this case it is possible to use an identification procedure by means of the telescope technique. A graphical cut of the α-particle was performed on ΔE versus E plot (fig. (6.7)) and for these particles a scatter plot of τ (see chapter (4.1.2)) versus the residual energy was produced fig. (6.12) Calculation of the τ versus the residual energy was performed as in the previous case. Red points correspond to elastic scattering; violet green

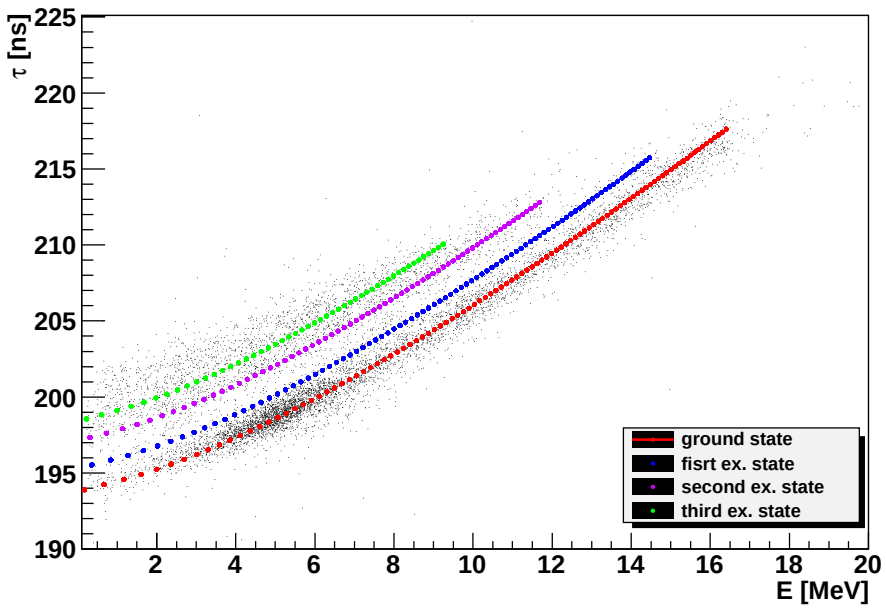

Figure 6.12: *τ vs residual energy E. Colored points represent calculations are superimposed on experimental data (black dots)). Red points correspond to elastically scattered α violet, green and pink points correspond to inelastic scattering respectively for the first, second and third excited state of ^8Li.*

and pink points correspond to inelastic scattering where ^8Li is excited to first (0.9808 MeV) second (2.255 MeV) and third (3.21 MeV) excited state respectively. A graphical cut of the lower band of α allows to select only elastically scattered alpha. The monodimensional spectrum is shown in fig. (6.13).

6.2.4 E_{cm} and θ_{cm} Reconstruction for α Stopped in E Detectors

Once the mono dimensional spectrum for elastically scattered particles was obtained, the same procedure of the previous case was used to determine the cross-section.

In this case the energy losses in ΔE detectors were included in the calculations. In tab.(6.4) an example of the energies of the particles after

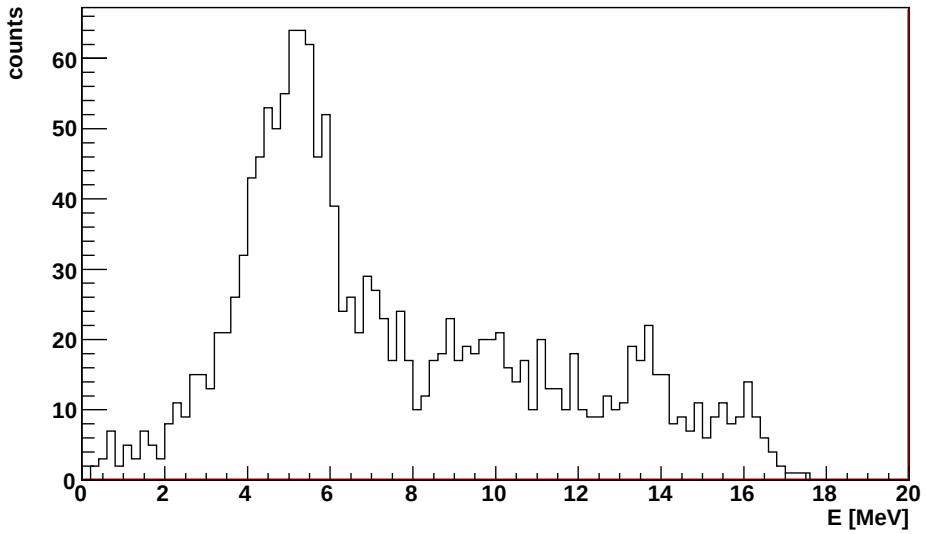

Figure 6.13: *Residual energy spectrum of elastically scattered α.).*

different steps of the calculation is shown .

Then the cross-section as a function of the centre of mass energy for the detector 3 at zero degree is shown in fig. (6.14). The error in the figure represent once more the statistical error only.

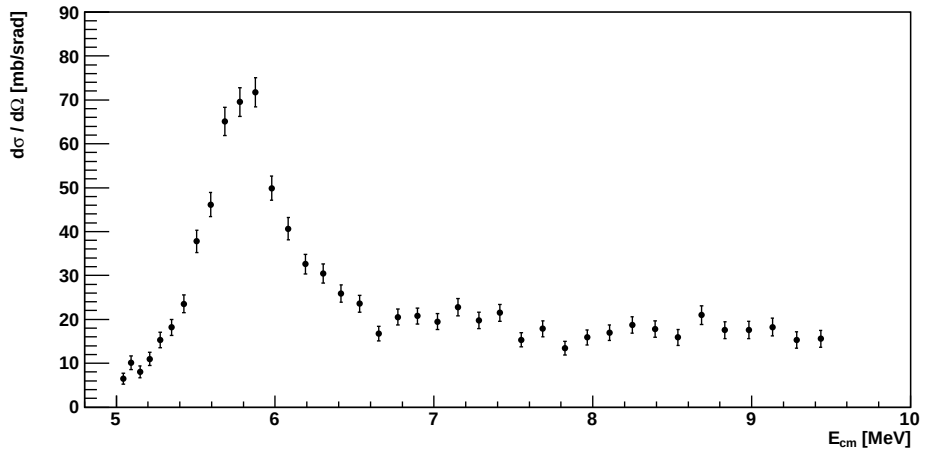

Figure 6.14: *Cross-section as function of CM energy for the the telescope 3.*

	detector 1	detector 3
^8Li initial energy	30.591 MeV	30.591 MeV
^8Li after kapton window	28.65 MeV	28.65 MeV
^8Li at point P	23.866 MeV	23.866 MeV
^4He after elastic scattering	20.9923 MeV	21.1969 MeV
^4He energy at point Q	15.5533 MeV	15.8079 MeV
^4He after Al QUAD entrance face metalization	15.5303 MeV	15.7849 MeV
^4He after Si QUAD entrance face dead layer	15.4833 MeV	15.7389 MeV
^4He after Si active layer	11.2863 MeV	12.4129 MeV
^4He after Si QUAD exit face dead layer	11.2273 MeV	12.3579 MeV
^4He after Al QUAD exit face metalization	11.1983 MeV	12.3309 MeV
^4He after ^4He gas layer between detectors	11.1133 MeV	12.2519 MeV
^4He after Al DSSSD metalization	11.0843 MeV	12.2249 MeV
^4He after Si DSSSD entrance face dead layer	11.0413 MeV	12.1849 MeV

Table 6.4: *Calculated energy in different steps of the overall calculations. From the detected energy (i.e. 11.0413 for detector1) it is possible to trace the energy at which the reaction took place (eg 23.866). The point* **P** *is 40 mm distant from the entrance of the chamber.*

6.3 Excitation functions

In this section the method used to extract the cross-section will be shown and discussed.

In fig. (6.15) a pictorial view of the detector array seen from the beam entrance side is shown . The ΔE detectors are divided into quadrants, so a color code is used to indicate those quadrants which are symmetric with respect to the beam axis.

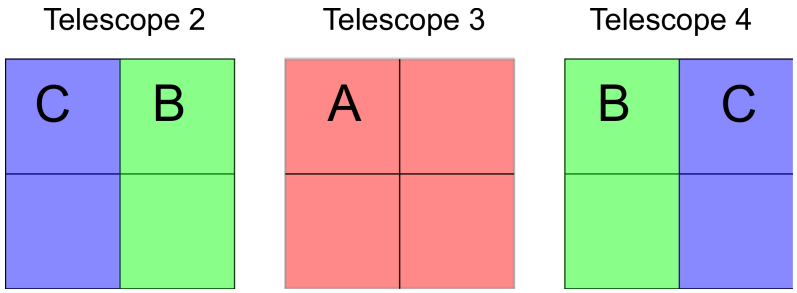

Figure 6.15: *Pictorial view of the telescope array as seen from the entrance of the chamber.*

The excitation function was extracted separately for each quadrant, (see fig. (6.16)), by following the procedure explained in the previous sections. The statistic relative to the telescope 1 placed at 10° was too low in order to extract the excitation function. The four excitation functions, obtained for example from the four quadrants of telescope 3 (red in fig. (6.15) give results coherent with each other since they correspond to the same angular range. Then, for each group of four quadrants A,B, C (see fig. (6.15)), which again corresponds to the same angular range, a weighted average of the cross-section for each energy bin was performed, see fig. (6.17, 6.18, 6.19). By comparing the different results obtained in the different angular ranges (see fig. (6.22)) one can observe that the resonances peaks are placed at the same positions. This evidence gives consistence and support to the validity of the overall detector calibration procedure (see cap. (4.2)). Let us fix the attention on one of the three

obtained excitation functions, for example the one deduced from data of telescope 3 (sector A). In the bottom part of fig. (6.17), one can see the one by one correspondence between the CM angle and each energy bin. One has to stress the fact that in the excitation function the angle is not

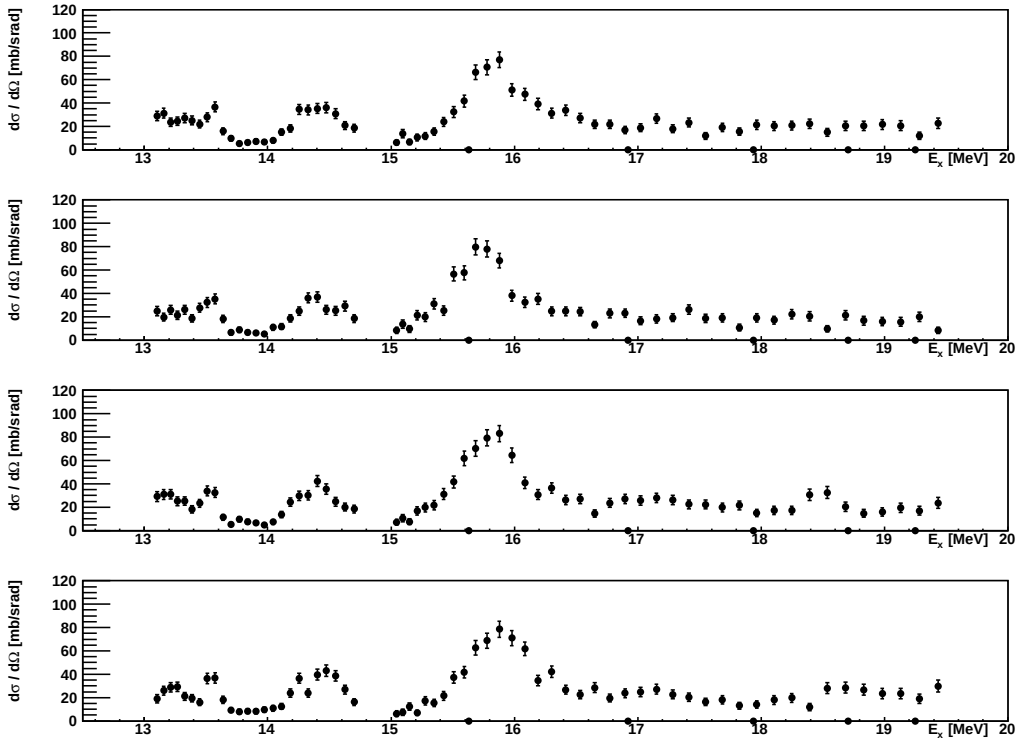

Figure 6.16: *Cross section as a function of centre of mass energy for the four quadrants of the telescope 3.*

constant but it is function of the centre of mass energy. Indeed since the quadrants are not placed at zero degree at each CM energy corresponds a given distance z at which the scattering took place and then a different scattering angle (see fig. (2.5)). In fig. (6.16 6.17, 6.18, 6.19) the absence of data in the energy spectra around 15 MeV is due to particles which stop in between the ΔE and E stages of the telescopes. The different displacement of these "hole" in the spectra of fig. (6.18) and (6.19) with respect to the spectra of fig. (6.17) is due to the combined effect of the different ΔE detector thickness and the different scattering angle

($175.5^\circ < \theta_{cm} < 178.5^\circ$ for the spectrum of fig.(6.17), $166^\circ < \theta_{cm} < 176.3^\circ$ and $162^\circ < \theta_{cm} < 174^\circ$ for the spectra of fig. (6.18 6.19) respectively.

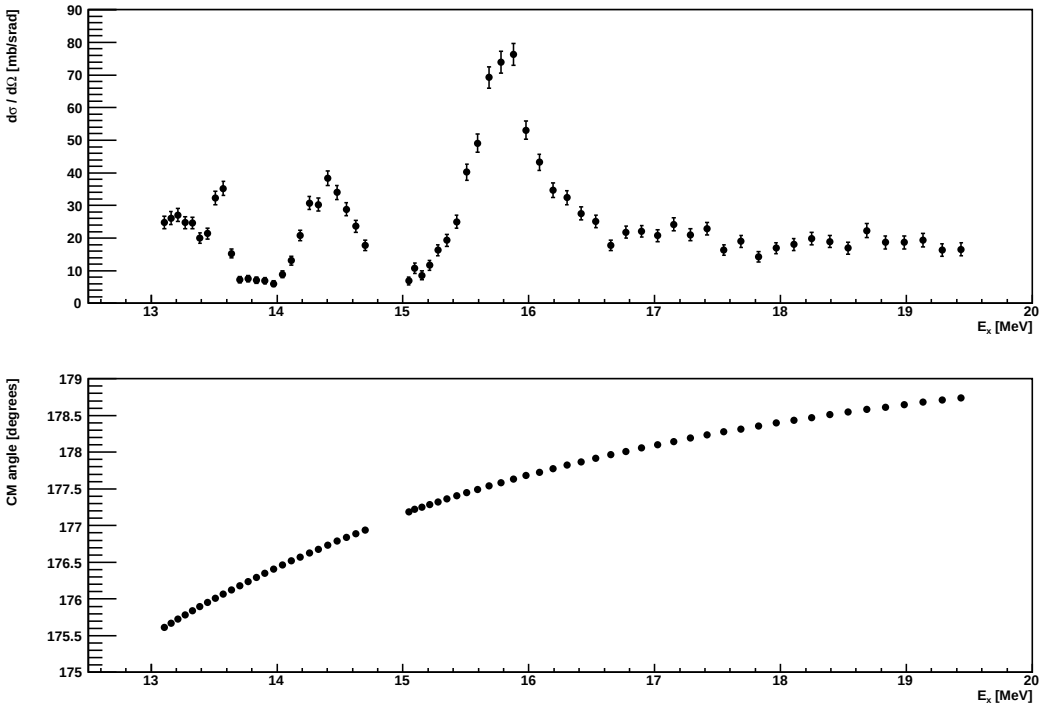

Figure 6.17: *On the top the cross is reported section as a function of the centre of mass energy for the telescope 3. The hole around 15 MeV is due to the dead layer between the two stages of the telescope. On the bottom the centre of mass scattering angle of ^8Li is shown as a function of the centre of mass energy. .*

Once the excitation function has been extracted, one has to pass to the extrapolation of the resonance parameters by fitting the experimental cross-section spectra by R-matrix (see cap. (2.4)). Although this theoretical analysis prescinds from this thesis work, a preliminary Rutherford scattering cross-section calculation has been performed for the sake of comparison.

In particular the excitation function for the telescope 3 (placed at zero degree) is compared with the Rutherford scattering cross-section see fig. (6.20). This last was calculated by means of the LISE code [61] by taking

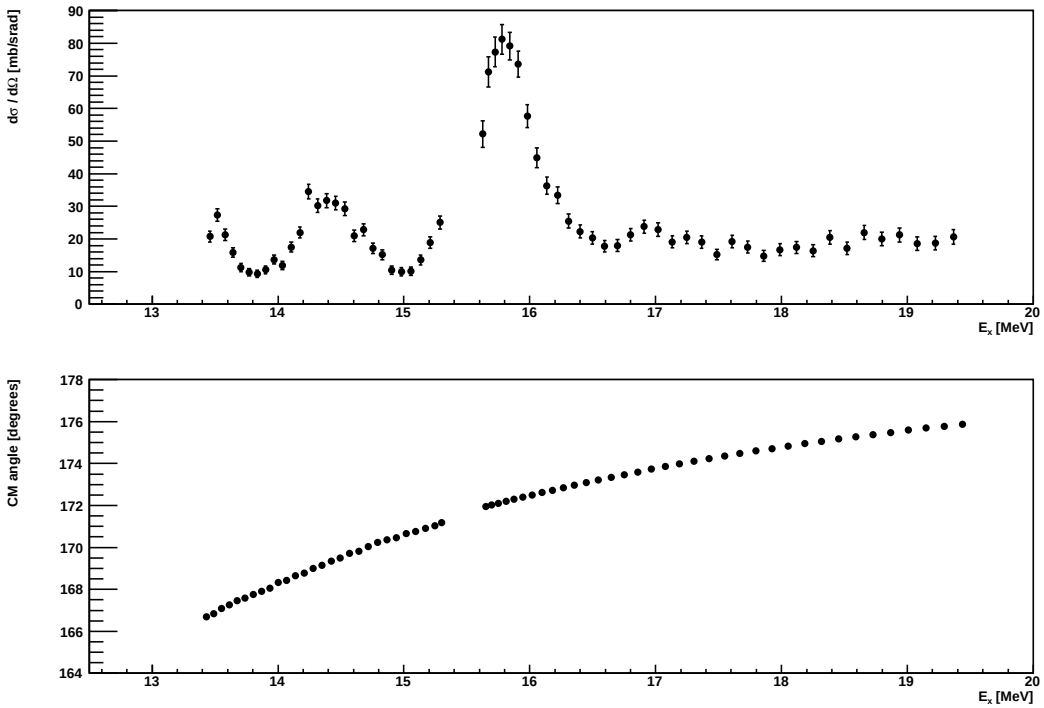

Figure 6.18: *On the top the cross section as a function of the centre of mass energy for the telescope 2. The hole around 15 MeV is due to the dead layer between the two stage of the telescope. On the bottom the centre of mass scattering angle of ^8Li as a function of the centre of mass energy. .*

into account the correct scattering angle in the centre of mass system for each excitation energy value (E_x and θ_{cm} couples of fig. (6.17), bottom part).

From this comparison one can observe that the order of magnitude of the extracted elastic cross-section at low energies (where the Rutherford cross-section is dominant) is consistent with Rutherford cross-section).

In fig. (6.21) the angular range at which the cross-section was measured is shown.

In fig. (6.22) the excitation function relative to the three groups of quadrant are shown. The cross section for the peak at 13.5 MeV seems to decrease for lower angles. Anyway, a conclusion on the behavior of the cross-section cannot be definitive since the peak is very close the energy

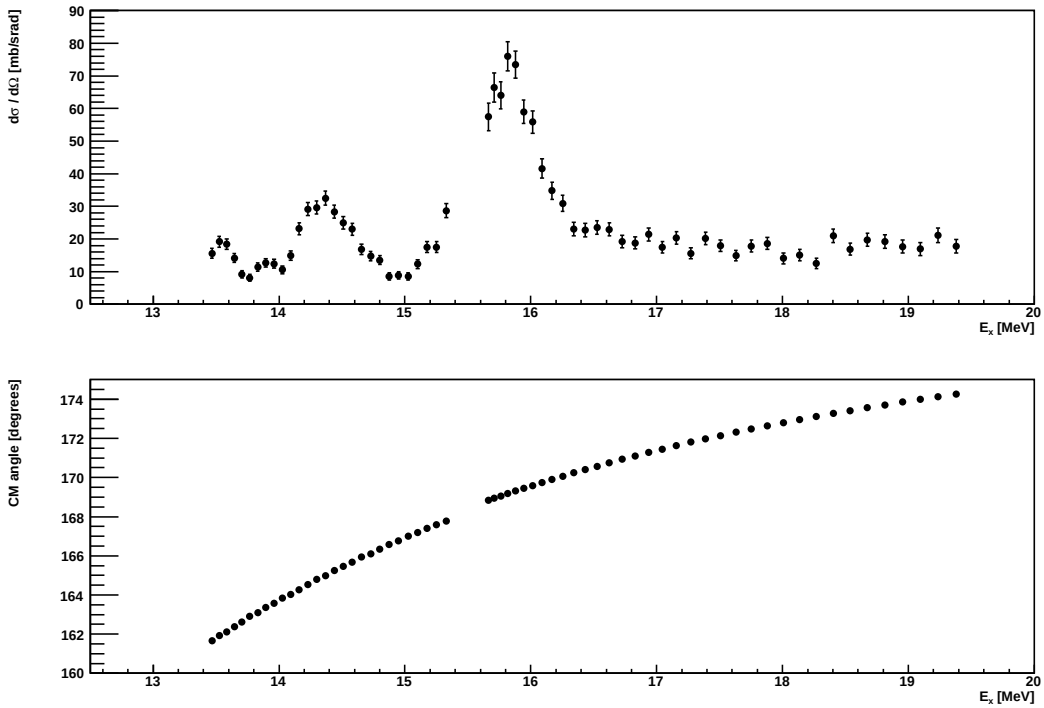

Figure 6.19: *On the top the cross section as a function of the centre of mass energy for the telescope 1. The hole around 15 MeV is due to the dead layer between the two stage of the telescope. On the bottom the centre of mass scattering angle of ^{8}Li as a function of the centre of mass energy. .*

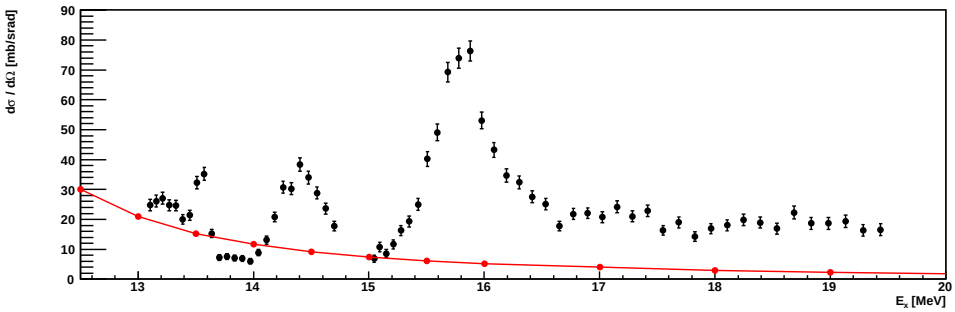

Figure 6.20: *Excitation function extracted from the telescope 3 (black dots).Rutherford cross section calculated for the correct scattering angle showed in the bottom of fig. (6.17 (red dots).*

range in which a contamination from triton particles is present.

Let us compare now these results to ^{12}B studies present in the literature (tab. (6.5)). Fig. (6.23) shows the ^{12}B excitation energy spectrum

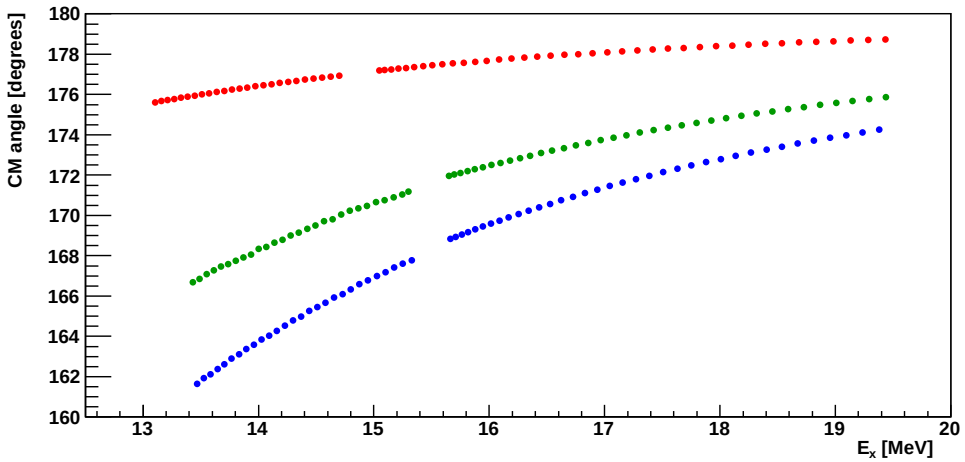

Figure 6.21: *θ_{cm} as function of the excitation energy. The plot shows the ^{8}Li scattering angle in the cm of mass system for each excitation energy at which the cross section was measured. The colors respect the color code of figure (6.15).*

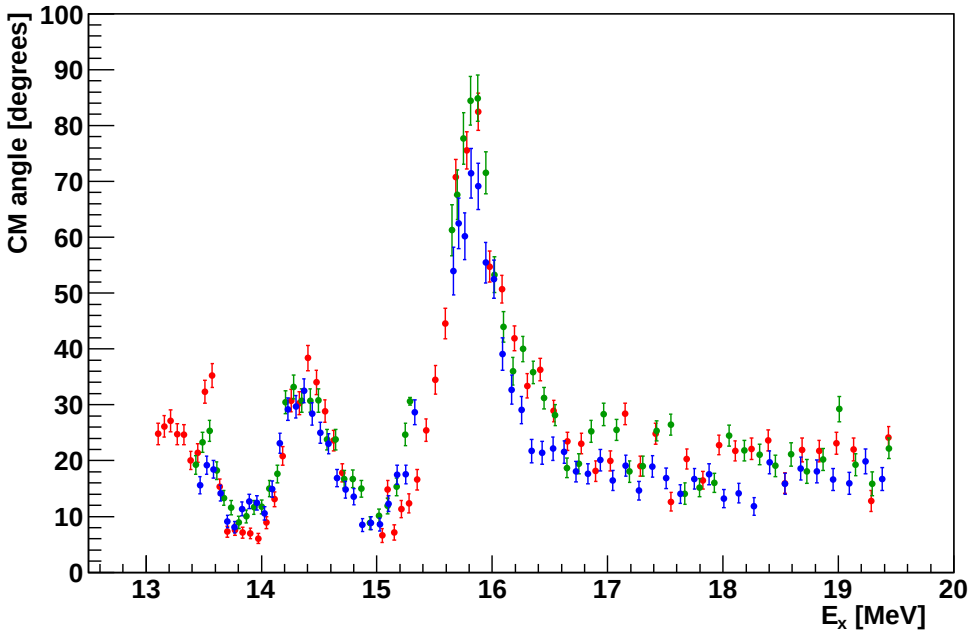

Figure 6.22: *Excitation functions for the three groups of quadrant corresponding to the three different angular range measured, see fig. (6.21). The colors respect the color code of figure (6.15).*

from the reaction ^{7}Li+^{9}Be $\rightarrow$ 2α +^{8}Li [76]. The first evidence one can observe is the correspondence of two resonances at excitation energies of 13.5 and 15.8 MeV with resonances at 13.4 and 15.7 Mev in ref. [76]. No feedback for our peak at 14.4 MeV. Anyway, as said before, any definitive assignment on R-matrix calculation is required. This last takes into account interference effects between the nuclear and the Coulomb part of the interaction as well interference phenomena between resonances.

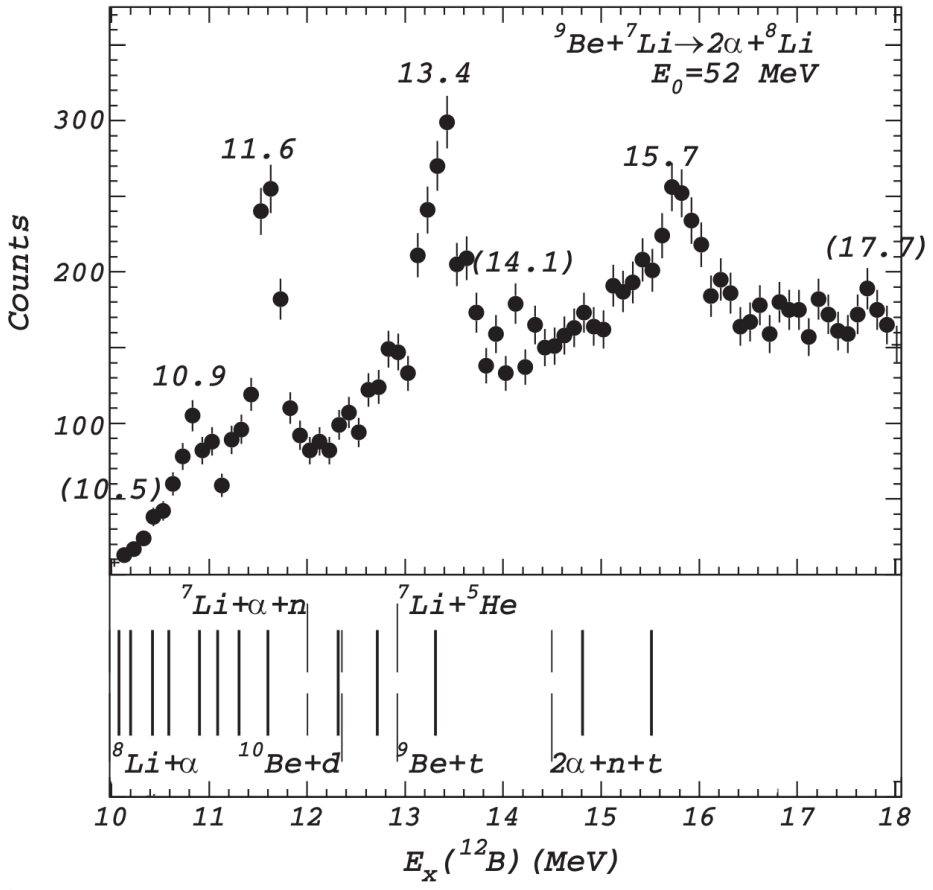

Figure 6.23: *The ^{12}B excitation energy spectrum from the reaction ^{7}Li+^{9}Be $\rightarrow$ 2α +^{8}Li on the top [76]. Scheme of adopted ^{12}B level scheme [27].*

Energy [MeV]	error [keV]	width [keV]	J^{π};T	reaction
13.330	30	50±20		A
13.4	100	broad		B
14.82	100	<200	2+; T=2	C
15.5				A

Table 6.5: *List of known states in the energy range of interest from ref. [27, 77]. reaction mark are: A:* $^{9}Be(^{7}Li,\alpha)$ *B:* $^{10}Be(t,p)$ *C:* $^{14}C(p,^{3}He)$

6.3.1 Systematic Errors

Systematic errors can raise from different sources: mis-knowledge of stopping power, beam profile, beam alignment, pressure and temperature values and MCP efficiency.

A stopping power mis-knowledge, as said before (see par. (2.3)), introduces systematic errors that have the effect to deform the excitation function (see fig. (2.6) and ref. [41]). Anyway the measurement of the stopping power of ^{4}He for ^{7}Li and the agreement with the semi-phenomenological data obtained from the SRIM code (see cap. (5)) make us confident on the used stopping power data.

In the present work, the ^{8}Li beam cross-section was assumed as point-like. The effect of a finite beam cross-section is that the path of the ^{8}Li and that one of the recoiling α-particles is different and this causes an error on the CM energy recovering. Anyway depending on the specific case, the CM energy can be underestimated or overestimated, thus the finite beam cross-section may affects the energy resolution rather than generate a systematic error.

A beam mis-alignment instead can generate a systematic error not only in the angular distribution but also in the reconstructed CM energy. The actual profile of the beam was measured by using the DSSSD 3 placed at zero degree. The MCP and the Kapton window, although they introduce a not negligible angular straggling, were kept on the beam line to reproduce accurately the measurement condition. The 2D and

3D histo as well as the projection on the x-axis and y-axis of the beam profile are shown in fig. (6.24). The beam is centered with respect to the detector. Moreover an indirect proof of the proper alignment is the fact that the excitation functions of the four quadrants of the detector 3 give consistent results.

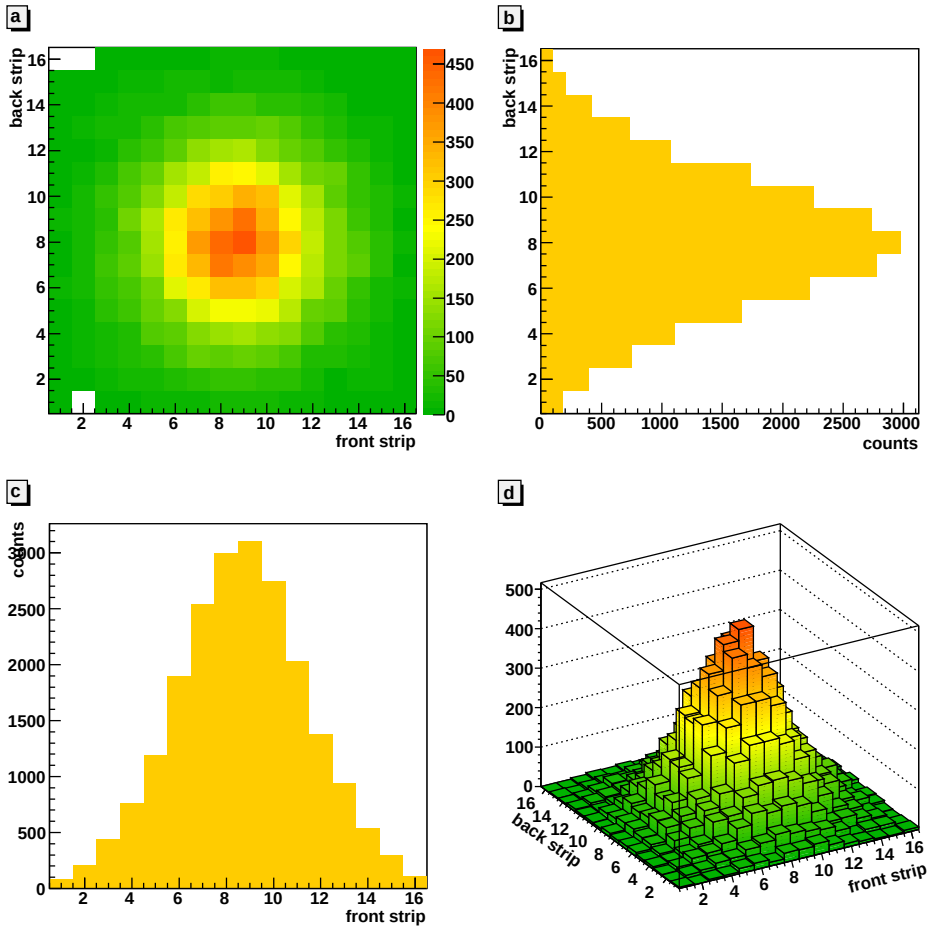

Figure 6.24: *ac 2D-histo and 3D-histo counts for each DSSSD pixel for a 8Li beam impinging on the DSSSD 3 (see fig. (6.15)) placed at the measurement position. b and c x-axis and y-axis profile of the beam size.*

Errors in pressure and temperature measurements can introduce systematic errors similar to that one generated by a mis-knowledge of the stopping power. Indeed an error on P or T results in an error on the density of the gas introducing a systematic error in the reconstruction of

CM energy. Moreover this affects also the number of particles in the target N_{ti} (see chap. 2.3) implying a systematic error in the cross-section. Since the pressure was slightly changing during the whole experiment, the value that has been used for cross-section calculation was the mean of the pressure values weighted with respect to the total number of beam particles in each run (counted by the MCP).

In order to estimate the effect of a systematic error in the pressure measurements on the excitation function we have repeated the overall procedure to calculate the excitation function for the value: 705.15 mbar corresponding to the maximum value measured during the experiment (this variation is comparable with the precision of the manometer that is 3‰). Fig. (6.25) reports the excitation function calculated by using

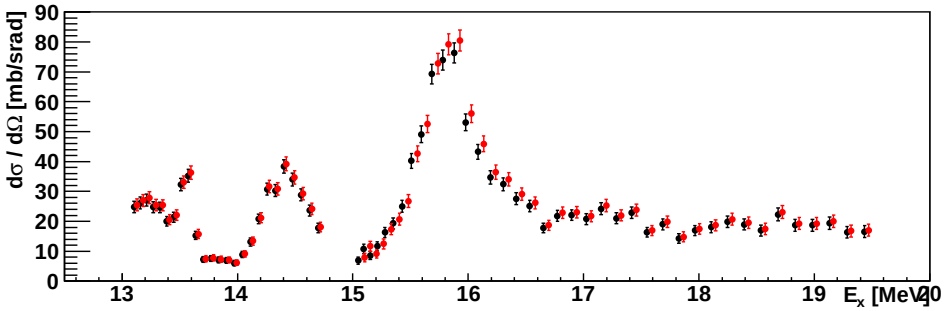

Figure 6.25: *Excitation function extracted by using two different pressure values. The measured value of the pressure P=702.63 mbar (black); the value P=705.15 corresponding to the larger pressure measured (red).*

two pressure value: the standard P=702.63 mbar (black) and the value P=705.15. Let us notice that the shift in the CM energies ($\sim$ 20 keV) is due to different energy losses due to the different density, while the differences in the value of the cross-section are due to the different values of N_{ti}.

For what concerns the temperature measurements the effects on the calculation are the same as those one obtained for the pressure: a change in the density of the gas and then in the energy losses and in the N_{ti}.

The precision of the thermocouple is 1 K. The density variation due to a variation due to a isothermal change of pressure ΔP=3 mbar, correspond also to the isobaric variation of 1.2 K (keeping P=702.63 fixed). We concluded that the difference between the energies of the resonance in our data and in data from literature can hardly be explained by assuming a systematic errors in the pressure or temperature measurements.

The number of particles of the beam was measured by MCP that has an efficiency of 99% at operating condition thus it does not represent a possible source of systematic errors.

The evaluation of the systematic error on the CM energy it is difficult. In fact, the systematic error on the CM energy reconstruction can originate from a mis-knowledge of the stopping power or for a systematic error in the knowledge of the geometry of the detector apparatus. The geometrical errors are very small and the effects are negligible, instead the effect of the stopping power mis-knowledge is to deforme the excitation function as shown in cap. (5). The effect of the stopping power mis-knowledge are known only if the mis-knowledge itself is known. Evaluating this systematic error without knowing the stopping power mis-knowledge is challenging.

The resolution is an essential element in order to perform a reliable R-matrix calculation and then to evaluate resonance parameters. Although an upper limit on the resolution can be given by looking at the peak at 13.4 MeV that in our data is large approximately 100 keV, a precise procedure aimed to the determination of the resolution is mandatory.
Besides the detector resolution, in order to properly determine the resolution, it is important to include in the calculations the beam size. Since the cross-section of the beam is not point-like, α-particles, detected at the same energy, can arrive on the detector through slightly different paths, corresponding to different energy losses and different CM scattering energy. An other effect, which produce the same consequences as

the beam spot, is the energy straggling for the beam particles and the recoiling particles. In order to evaluate the energy resolution, by taking into account all these effects, we plan to perform a complete Monte Carlo simulation.

Appendix A

Level Schemes

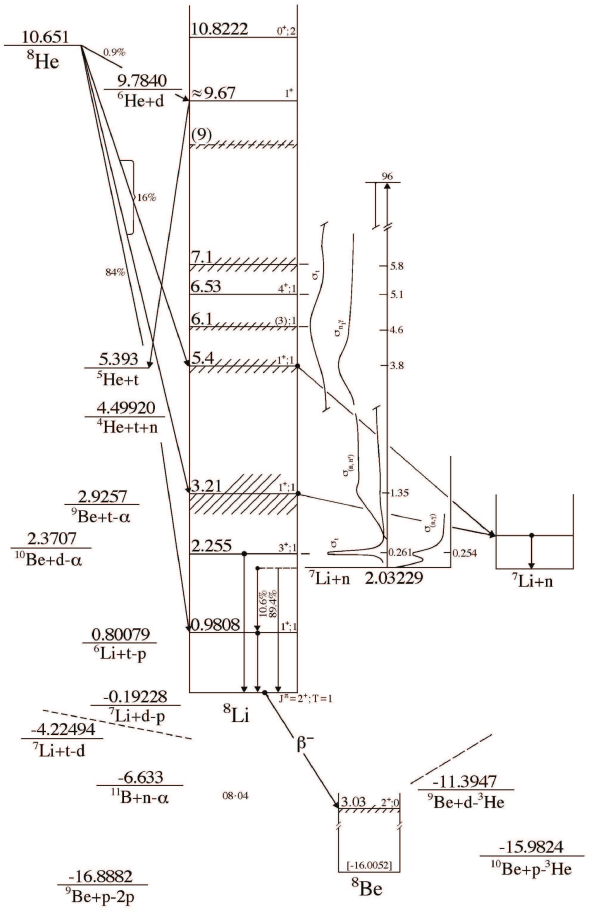

Figure A.1: ^{8}Li *level scheme from [72].*

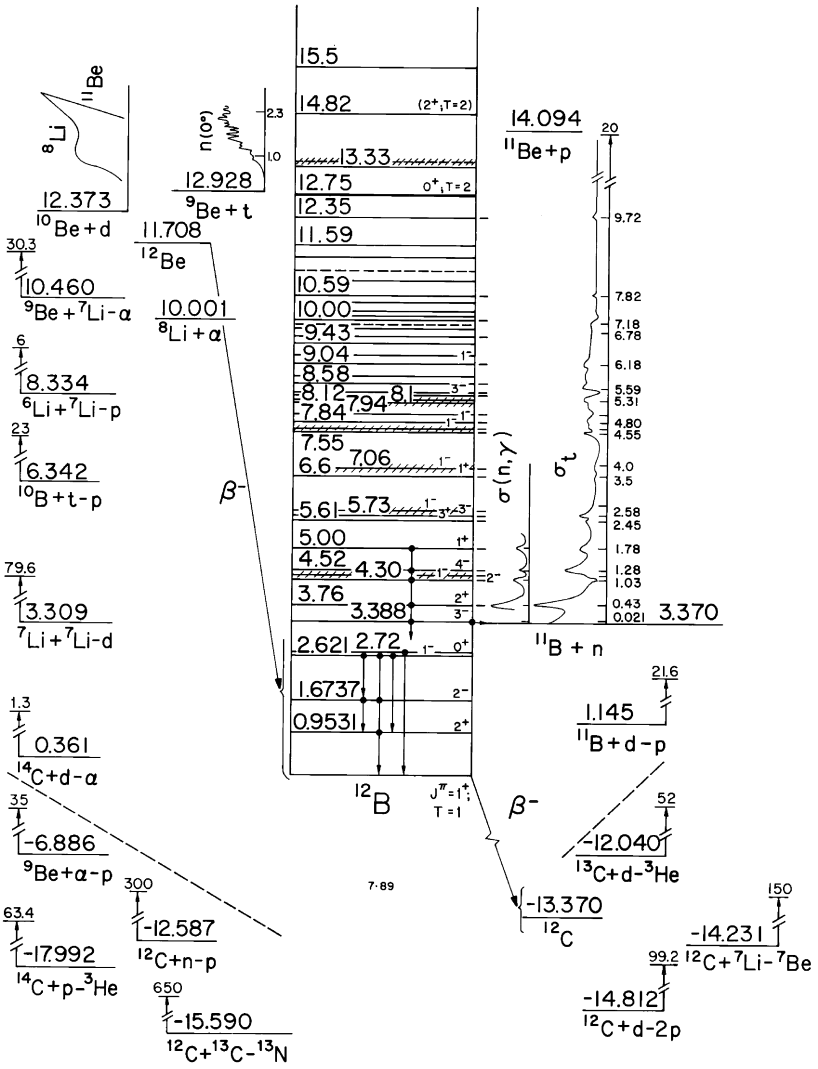

Figure A.2: ^{12}B *level scheme from [72].*

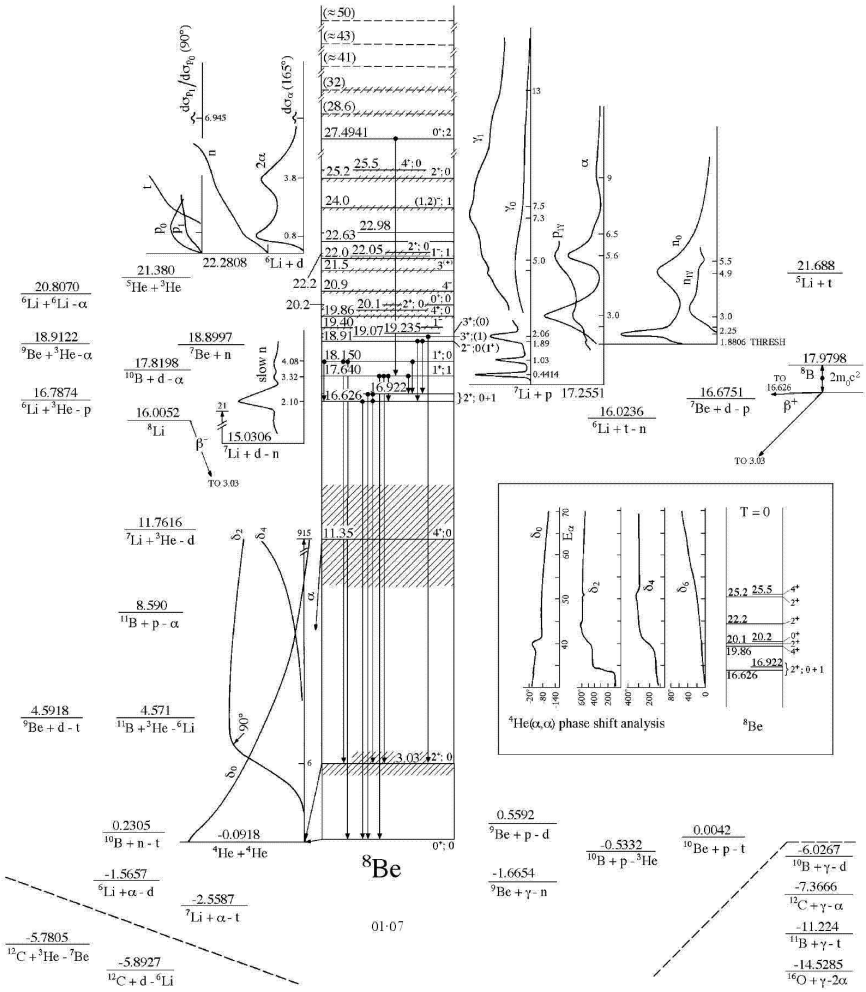

Figure A.3: ^{8}*Be level scheme from [72].*

Conclusions and Future Perspectives

In the past years theoretical efforts were devoted to the studies of the cluster structures of neutron-rich nuclei.

In this thesis a study of possible ^{8}Li-α cluster structures was carried out. For this purpose an experiment to study the ^{8}Li-α elastic scattering was performed for the first time. The experimental technique is the thick target inverse kinematics scattering method coupled with a time of flight measurement. This last allowed to discriminate the elastic events from inelastic and other background events.

During the experiment measurements of ^{4}He stopping power for the ^{7}Li were also performed in order to cross-check the results coming from stopping power codes. A good agreement with data coming from the SRIM code was found. Then the results from the SRIM code were included in the calculation that allows to determine the CM energy and angle from the position and the detected energy of α-recoiling particles.

The excitation function was obtained in the range of ^{12}B excitation energy between 13 MeV and 19.5 MeV at three different angular ranges from 161° to 175° for the lowest energy and from 174° to 178° for the highest energies (the explored angular range depends on the energy). Although before any definitive assignment an R-matrix calculation is needed, which requires in any case a resolution estimation, we can preliminary observe an agreement, within 200 KeV, for the energies position of the resonances

present in our data and reported in the literature.

In order to complete the analysis of the elastic scattering for ^{8}Li on ^{4}He, taking into account the effects of the energy and angular straggling as well as the finite dimension of the beam cross-section, a Monte Carlo simulation is planned. From this it will be possible to extract the energy resolution of the spectra obtained in this thesis. The resolution is a necessary element in order to perform an R-matrix calculation that is the final step of the analysis.

From R-matrix calculation it will be possible to extract the parameters of the resonances as energies and widths. From the angular distributions it is possible to assign spin and parity to the state. It is important to underline that from the values of the partial decay widths of the resonances it is possible to have indication on the characteristic of the resonances. In particular narrow peaks (of hundreds keV) and large reduced α-widths are the signatures of a cluster structure.

In the future, a new measurement can be performed in order to explore ^{12}B excitation energies between 10 MeV and 13 MeV, where a cluster band of positive parity was predicted by Descouvemont in the framework of GCM [10].

From the experimental point of view the use of a detector capable to track the recoiling α-particles can be a possible extension of the technique. The advantages of using the tracking are different. First it is possible to make an event by event analysis. Moreover the determination of the scattering point and angle become independent on the stopping power data. The CM energy reconstruction becomes less sensible, although not independent, on the stopping power calculation depending only on the ^{4}He stopping power for ^{8}Li and no more on the ^{4}He stopping power for α-particles.

In the future to continue the study of B isotopes a measurement of the

system ^{9}Li-^{4}He is planned.

Bibliography

[1] W. von Oertzen, M. Freer, and Y. Kanada-En'yo. Nuclear clusters and nuclear molecules. *Phys. Rep.*, 423:43,113, 2006.

[2] H. Horiuchi and Y. Kanada-En'yo. Structure of light exotic nuclei studied with amd model. *Nucl. Phys. A*, 616:349c–405c, 1997.

[3] Yoshiko Kanada-En'yo, Hisashi Horiuchi, and Akira Ono. Structure of li and be isotopes studied with antisymmetrized molecular dynamics. *Phys. Rev. C*, 52(2):628–646, Aug 1995.

[4] Y. Kanada-En'yo and H. Horiuchi. Neutron-rich b isotopes studied with antysimmetrized molecular dynamics. *Phys Rev. C*, 52:647, 1995.

[5] Y. Kanada-En'yo and H. Horiuchi. *Prog. Theor. Phys.*, 142:205, 2001.

[6] Y. Kanada-En'yo and H. Horiuchi. *Phys Rev. C*, 68:014319, 2003.

[7] P. Descouvemont and I. Baraffe. *Nucl. Phys. A*, 514:66–86, 1990.

[8] D. Baye and P. Descouvemont. *Phys. Soc. Japan (Suppl.)*, 58:103, 1989.

[9] D. Baye, P.H.Heenen, and Lienert Heinemann. *Nucl. Phys. A*, 291:230, 1977.

[10] P. Descouvemont and D. Baye. *Nucl. Phys. A*, 596:285–298, 1995.

[11] E. Almqvist, D. A. Bromley, and J. A. Kuehener. *Phys. Rev. Lett.*, 4:515, 1960.

[12] K. Ikeda, T. Marumori, R. Tamagaki, and H. Tanaka. Formation of the Viewpoint, Alpha-Like Four-Body Correlations and Molecular Aspects in Nuclei. *Suppl. Prog. Theor. Phys.*, 52:1, 1972.

[13] K. Ikeda, H. Horiuchi H., and S. Saito. Introduction to Comprensive Nuclear Structure Study Based on Cluster Correlations and Molecular Viewpoint. *Suppl. Prog. Theor. Phys.*, 68:1, 1980.

[14] M. Freer. The clustered nucleus. *Rep. Prog. Phys.*, 70:2149–2210, 2007.

[15] L.R. Hafstad and E. Teller. The Alpha-Particle Model of the Nucleus. *Phys. Rev.*, 54:681, 1938.

[16] W. von Oertzen. *Z. Phys. A*, 354:37, 2006.

[17] W. von Oertzen. *Nuovo Cimento A*, 110:895, 1997.

[18] N. Itagaki and S. Okabe. . *Phys. Rev. C*, 61:044306, 2000.

[19] Y. Akaishi, S.A. Chin, H. Horiuchi, and k. Ikeda. *Cluster Model and Other Topics*. Tools and Techniques for Computer Typesetting. World Scientific, Singapore, 1986.

[20] J.A Wheeler. Molecular Viewpoints in nuclear Structure. *Phisycal Review*, 52:1083, 1937.

[21] Y.C. Tang, M. LeMere, and D.R. Thompsom. Resonating-group method for nuclear many-body problems. *Physics Reports*, 47:167–223, 1978.

[22] P. Descouvemont. *Nucl. Phys. A*, 699:463, 2002.

[23] H. Ono, T. Horiuchi, Maruyana, and A. Ohnishi. . *Prog. Theor. Phys.*, 87:1185, 1992.

[24] H. Ono and T. Horiuchi. . *Phys. Rev. C*, 51:299, 1995.

[25] M. Dufour and P. Descouvemont. *Nucl. Phys. A*, 726:53, 2003.

[26] M. Dufour and P. Descouvemount. *Nucl. Phys. A*, 672:153, 2000.

[27] F. Ajzenber-Selove. *Nucl. Phys. A*, 506:1, 1990.

[28] Jun Jhon Sakurai. *Meccanica Quantistica Moderna*, pages 412–415. Zanchelli, 1996.

[29] M Norrby. 28 si + α as an example of novel methods for elastic scattering experiments. *Journal of Physics: Conference Series*, 111(1):012036, 2008.

[30] Jiarui Liu, Zongshuang Zheng, and Wei-Kan Chu. Cross section for non-rutherford backscattering of α on be. *Nuclear Inst. and Methods in Physics Research, B*, 108:247–250, 1996.

[31] K.M. Kallman, V.Z. Goldberg, T. Lonnroth, P. Manngard, A.E. Pakhomov, and V.V. Pankratov. Thick-target backscattering technique to measure α-particle elastic scattering cross sections. *Nuclear Inst. and Methods in Physics Research, A*, 338:413–418, 1994.

[32] K.-M. Kallman, M. Brenner, V.Z. Goldberg, T. Lonnroth, P. Manngard, A.E. Pakhomov, and V.V. Pankratov.

[33] Carmen Angulo. Study of excited states in proton-rich nuclei by resonant elastic scattering. *Nuclear Physics A*, 746:222–228, 2004.

[34] C. Angulo, G. Tabacaru, M. Couder, M. Gaelens, P. Leleux, A. Ninane, F. Vanderbist, T. Davinson, P. J. Woods, J. S. Schweitzer,

N. L. Achouri, J. C. Angélique, E. Berthoumieux, F. de Oliveira Santos, P. Himpe, and P. Descouvemont. Identification of a new low-lying state in the proton drip line nucleus ^{19}na. *Phys. Rev. C*, 67(1):014308, Jan 2003.

[35] M.G. Pellegriti, N.L. Achouri, C. Angulo, J.-C. AngÃ©lique, E. Berthoumieux, E. Casarejos, M. Couder, T. Davinson, C. Ghag, A.St. Murphy, N.A. Orr, I. Ray, I.G. Stefan, and P. Descouvemont. Evidence for core excitation in single-particle states of 19na. *Physics Letters B*, 659(5):864 – 869, 2008.

[36] K. P. Atremov et al. . *Sov. J. Nucl. Phys.*, 1990.

[37] Skorodumov. *Resonance Reactions Induced by Light Radioactive Beams*. PhD thesis, University of Notre Dame, 2007.

[38] G. V. Rogachev. PhD thesis, Russian Centre "Kurchatov Institute", 1999.

[39] V. Z. Goldberg, G. V. Rogachev, W. H. Trzaska, J. J. Kolata, A. Andreyev, C. Angulo, M. J. G. Borge, S. Cherubini, G. Chubarian, G. Crowley, P. Van Duppen, M. Gorska, M. Gulino, M. Huyse, P. Jesinger, K.-M. Källman, M. Lattuada, T. Lönnroth, M. Mutterer, R. Raabe, S. Romano, M. V. Rozhkov, B. B. Skorodumov, C. Spitaleri, O. Tengblad, and A. Tumino. Investigation of the α -cluster structure of ^{22}ne and ^{22}mg. *Phys. Rev. C*, 69(2):024602, Feb 2004.

[40] J. D. Goss, S. L. Blatt, D. R. Parsignault, C. D. Porterfield, and F. L. Riffle. Elastic scattering of α particles by ^{9}be and highly excited states of ^{13}c. *Phys. Rev. C*, 7(5):1837–1845, May 1973.

[41] M. Zadro et al. *Nuclear Inst. and Methods in Physics Research, B*, 297:836–840, 2007.

[42] V. Scuderi, M. Zadro, et al. *Eur. Ohys. J. Special Topics*, 150:53–54, 2007.

[43] J. Ziegler, 2008.

[44] Eugene P. Wigner. Resonance reactions and anomalous scattering. *Phys. Rev.*, 70(1-2):15–33, Jul 1946.

[45] Eugene P. Wigner. Resonance reactions. *Phys. Rev.*, 70(9-10):606–618, Nov 1946.

[46] E. P. Wigner and L. Eisenbud. Higher angular momenta and long range interaction in resonance reactions. *Phys. Rev.*, 72(1):29–41, Jul 1947.

[47] A. M. Lane and R. G. Thomas. R-matrix theory of nuclear reactions. *Rev. Mod. Phys.*, 30(2):257–353, Apr 1958.

[48] P. Descouvemont and D. Baye. *Rep. Prog. Phys.*, 73:036301, 2010.

[49] D.J. Morrissey and B.M. Sherill. In flight Separation of Projectile Fragments. *Lect. Notes Phys.*, 651:113–135, 2004.

[50] G. Cuttone et al. Status and perspectives of the EXCYT facility at INFN-LNS. *Nucl. Inst. Meth. B*, 266:4108–4112, 2008.

[51] G. Ciavola et al. The progress of the EXCYT facility at INFN-LNS. *Proceedings of EPAC 2000, Vienna, Austria*, pages 2597–2599, 2000.

[52] D. Rifuggiato et al. In *Proc. of the XVII International Conference on Cyclotrons and their Applications*, page 118, 2004.

[53] G. Cuttone et al. EXCYT: The RIB project at INFN-LNS. *Nucl. Inst. Meth. B*, 261:1040–1043, 2007.

[54] G. Ciavola et al. *Nuclear Physics A*, 701:54c–57c, 2002.

[55] A status report of the EXCYT Project. Technical report, Laboratori Nazionali del Sud, August 2001.

[56] M. Re, M. Menna, F. Chines, G. Cuttone, E. Messina, and D.W. Stracener. In *Proceedings of the Particle Accelerator Conference 2005, Knoxville*, page 898, 2005.

[57] D. Rifuggiato et al. In *Proc. of the 10th International Spring Seminar on Nuclear Physics, Vietri sul Mare, Italy.* to be published on AIP, May 2010.

[58] A. Musumarra, P. Figuera, F. De Luca, A. Di Pietro, P. Finocchiaro, M. Fisichella, M. Lattuada, A. Pakou, M.G. Pellegriti, G. Randisi, G. Scalia, C. Sciré, S. Sciré, V. Scuderi, D. Torresi, and M. Zadro. Measuring total reaction cross-sections at energies near the coulomb barrier by the active target method. *Nuclear Instruments and Methods in Physics Research Section A: Accelerators, Spectrometers, Detectors and Associated Equipment*, 612(2):399 – 406, 2010.

[59] Joseph Ladislas Wiza. Microchannel plate detectors. *Nuclear Instruments and Methods*, 162:587–601, 1979.

[60] Y. Blumenfeld, F. Auger, J.E. Sauvestre, F. Maréchal, S. Ottini, N. Alamanos, A. Barbier, D. Beaumel, B. Bonnereau, D. Charlet, J.F. Clavelin, P. Courtat, P. Delbourgo-Salvador, R. Douet, M. Engrand, T. Ethvignot, A. Gillibert, E. Khan, V. Lapoux, A. Lagoyannis, L. Lavergne, S. Lebon, P. Lelong, A. Lesage, V. Le Ven, I. Lhenry, J.M. Martin, A. Musumarra, S. Pita, L. Petizon, E. Pollacco, J. Pouthas, A. Richard, D. Rougier, D. Santonocito, J.A. Scarpaci, J.L. Sida, C. Soulet, J.S. Stutzmann, T. Suomijarvi, M. Szmigiel, P. Volkov, and G. Voltolini. Must: A silicon strip detector array for radioactive beam experiments. *Nuclear Instruments*

and Methods in Physics Research Section A: Accelerators, Spectrometers, Detectors and Associated Equipment, 421:471–491, 1999.

[61] O. Tarasov and D. Bazin, 2008.

[62] James F. Ziegler. Srim-2003. *Nuclear Instruments and Methods in Physics Research Section B: Beam Interactions with Materials and Atoms*, 219-220:1027–1036, 2004.

[63] Helmut Paul.

[64] *ICRU report*, 49:253, 1993.

[65] Jyh-Yuo Hsu and Jenq-Horng Liang. In *Proc. of the 10th International Conference on Particle Induced X-ray Emission and its Analytical Applications PIXE 2004, Portoroz, Slovenia*, page 118, 2004.

[66] S.K. Allison and C.S Littlejohn. *Physical Review*, 104:959, 1956.

[67] S.K. Allison, D. Auton, and R.A. Morrison. *Physical Review*, 138:68, 1965.

[68] J. Laursen C. Hanke. *Nucl. Instr. and Meth.*, 151:253, 1978.

[69] J. Yorkston, A.C. Shotter, D.B. Syme, and G. Huxtable. Interstrip surface effects in oxide passivated ion-implanted silicon strip detectors. *Nuclear Inst. and Methods in Physics Research, A*, 262:353–358, 1987.

[70] U.C. Bergmann, H.O.U. Fynbo, and O. Tengblad. Use of si strip detectors for low-energy particles in compact geometry. *Nuclear Instruments and Methods in Physics Research Section A: Accelerators, Spectrometers, Detectors and Associated Equipment*, 515:657–664, 2003.

[71] Chris Wrede, Ahmed Hussein, Joel G. Rogers, and John D'Auria. A double sided silicon strip detector as a dragon end detector. *Nuclear Instruments and Methods in Physics Research Section B: Beam Interactions with Materials and Atoms*, 204:619–624, 2003.

[72] *http://www.tunl.duke.edu/nucldata/*, 2010.

[73] J. A. Brown, F. D. Becchetti, J. W. Jänecke, K. Ashktorab, D. A. Roberts, J. J. Kolata, R. J. Smith, K. Lamkin, and R. E. Warner. Coulomb excitation of ^{8}li. *Phys. Rev. Lett.*, 66(19):2452–2455, May 1991.

[74] R. J. Smith, J. J. Kolata, K. Lamkin, A. Morsad, F. D. Becchetti, J. A. Brown, W. Z. Liu, J. W. Jänecke, D. A. Roberts, and R. E. Warner. Elastic and inelastic scattering of ^{8}li from ^{12}c. *Phys. Rev. C*, 43(5):2346–2352, May 1991.

[75] A. Szczurek, K. Bodek, L. Jarczyk, J. Krug, J. Krug, W. Lubcke, H. Ruhl, M. Steinke, M. Stephan, D. Kamke, and A. Strzalkowski. Ghost anomaly and first excited state of 8be in the 9be(d, t[alpha])4he reaction at 7 mev. *Nuclear Physics A*, 531(1):77 – 92, 1991.

[76] N. Soić et al. *Europhys. Lett*, 63:524–530, 2003.

[77]